universität wien

MASTERARBEIT / MASTER'S THESIS

Titel der Masterarbeit / Title of the Master's Thesis

„Investigating the Influence of Modifications on R5-derived Peptides in Silica precipitation and Immune stimulation“

verfasst von / submitted by

Martina Höllwarth, BSc

angestrebter akademischer Grad / in partial fulfilment of the requirements for the degree of

Master of Science (MSc)

Wien, 2023 / Vienna 2023

Studienkennzahl lt. Studienblatt / degree programme code as it appears on the student record sheet:	A 066 863
Studienrichtung lt. Studienblatt / degree programme as it appears on the student record sheet:	Masterstudium Biologische Chemie
Betreut von / Supervisor:	Univ.-Prof. Dr. Christian Friedrich Wilhelm Becker

Acknowledgments

First and foremost, I want to extend my deepest gratitude to Univ.-Prof. Dr. Christian Friedrich Wilhelm Becker for his guidance and supervision throughout my master's thesis, as well as for sharing his expertise.

I would also like to express my appreciation to Fanny Kozak, BSc MSc, for providing the data and allowing the inclusion in the thesis. Special thanks for her detailed explanations and enthusiastic responses to my questions. I am also grateful to SyntabTherapeutics (Aachen) for conducting the cellular assay and for our smooth exchanges. Thanks, should also go to Mag. Dr. Stephan Puchegger for providing an introduction to scanning electron microscopy.

Many thanks to all members of the Becker group, each of whom contributed to my personal and professional development. I appreciate the guidance of Mag. Manuel Felkl in the initial weeks and his ongoing support. Additionally, I would like to recognize Laura Holzapfel, BSc for her contributions to automated peptide synthesis.

I am fortunate to have had colleagues like Somnath Mukherjee, BSc MSc PhD, Dominik Vogl, BSc MSc, Oliver Gajsek, BSc MSc in the office, who explained and discussed scientific questions and made the small breaks enjoyable. Special thanks to Hannah Back, BSc MSc, and Dr. Claudia Cobos Caceres, BSc for their kindness, openness and unwavering assistance whenever I sought their help. I am extremely grateful to Dr. Moritz Urschbach, BSc MSc for sharing the bench and providing valuable advice and also for proofreading. Thank you to all the other colleges and fellow master students.

Last but not least, I want to express my gratitude to my mother Irmgard Höllwarth, my sister Manuela Höllwarth, and my boyfriend Alfons Huber, for their unwavering belief in me and constant support.

Abstract

The biomimetic silica formation process, driven by silaffin-based peptides and characterized by mild conditions, has garnered interest for its potential applications in biomedicine and biotechnology. The method is inspired by the biomineralization process in diatoms, that is modulated amongst others by the highly modified silaffin protein. It has been shown that the silaffin derived R5 peptide, lacking all posttranslational modifications, induces silica precipitation in the presence of phosphate ions. In depth mechanistical studies revealed that the RRIL tetrapeptide within R5 plays a crucial role in promoting self-assembly in solution, a key step in the silica formation process. Additional investigations by our group led to the discovery of two branched peptides containing the RRIL motif, namely K*(rrill)-RRIL and k*(rrill)-RRIL. The RRIL motifs are linked by an isopeptide bond (*) and form different compact self-assemblies in phosphate buffer, giving rise to distinct morphologies upon silicic acid addition.

In this work the influence of modifications at the *N*-termini of the artificial silica-precipitating peptides K*(rrill)-RRIL and k*(rrill)-RRIL on silica morphology was further investigated. The modifications included coupling of the bacterial danger signal formyl-methionine-leucine-phenylalanine (fMLF) *via* a polyethylene glycol (PEG_3) chain to either available α-amino group, as well as other modifications to assess the individual contributions of each building block to silica particle morphology. The results demonstrated that elongation with fMLF-PEG_3 consistently resulted in spherical particles, irrespective of the position in the peptides. The steric bulk and hydrophobicity of the fMLF motif may interfere with the dense peptide self-assembly crucial for rod-shaped particles, resulting in less dense self-assembly and ultimately spherical particles. Additionally, the study revealed the potential impact of the charged *N*-terminus on self-assembly and the following formation of distinct morphologies. Moreover, an intriguing peptide capable of precipitating both spherical and rod-shaped particles was found and analyzed using nuclear magnetic resonance (NMR) methods, which suggested the involvement of two processes with different kinetics leading to the formation of two distinct morphologies.

The fMLF modification was primarily selected due to its innate immune system stimulating properties by activating the formyl peptide receptor (FPR). Paired with silica particles as delivery systems, it could enhance vaccine responses as an adjuvant. The investigation of peptide incorporation and release within the particles showed promising outcomes. Additionally, the immune stimulating potential of both modified peptides and their corresponding particles was evaluated using a dihydro rhodamine (DHR) assay, illustrating their ability to induce reactive oxygen species (ROS) production and indicating FPR activation.

Zusammenfassung

Die Synthese von biomimetischem Silica, gesteuert durch Silaffin-basierte Peptide, weckte aufgrund der milden Bedingungen das Interesse für mögliche Anwendungen in der Biomedizin und der Biotechnologie. Die Methode orientiert sich am Biomineralisationsprozess der Diatomeen, der unter anderem von stark modifizierten Silaffin Proteinen kontrolliert wird. Weitere Studien demonstrierten, dass R5, ein artifizielles Silaffin Derivat ohne posttranslationale Modifikationen, in Anwesenheit von Phosphat-Ionen die Bildung von Silica-Partikeln induziert. Detaillierte mechanistische Studien zeigten die bedeutende Rolle des Tetrapeptids RRIL innerhalb des R5 bei der Selbstassemblierung, einem Schlüsselschritt der Silica Präzipitation. Weitere Untersuchungen unserer Gruppe führten zur Beschreibung von zwei verzweigten Peptiden, und zwar K*(rrill)-RRIL und k*(rrill)-RRIL. Die RRIL-Motive sind durch eine Isopeptid-Bindung (*) miteinander verbunden und bilden in Lösung verschieden dichte Selbstassemblierungen, wodurch nach Zugabe von Kieselsäure Partikel unterschiedlicher Morphologie entstehen.

Diese Arbeit untersucht den Einfluss von Modifikationen an den *N*-Termini der artifiziellen Silica-präzipitierenden Peptide K*(rrill)-RRIL und k*(rrill)-RRIL auf die Silica-Morphologie. Die Modifikationen umfassten die Kopplung des bakteriellen Gefahren-Signals Formyl-Methionin-Leucin-Phenylalanin (fMLF) über eine Polyethylenglykol (PEG_3)-Kette an je eine verfügbare α-Aminogruppe, sowie weitere Modifikationen zur Bestimmung des individuellen Beitrags jedes Bausteins zur Silica-Partikel-Morphologie. Die Ergebnisse zeigten eine konsistente Bildung von kugelförmigen Partikeln bei der Verlängerung mit fMLF-PEG_3, unabhängig von der Position im Peptid. Dies könnte auf den sterischen Anspruch und die Hydrophobizität der fMLF-Modifikation zurückzuführen sein, die die dichte Selbstassemblierung, erforderlich für stäbchenförmige, reduziert und somit zu kugelförmigen Partikeln führt. Die Studie wies auch auf einen potenziellen Beitrag des geladenen *N*-Terminus zur Selbstassemblierung und die darauffolgende Bildung einer definierten Morphologie hin. Ein faszinierendes Peptid, das sowohl kugel- als auch stäbchenförmiger Partikel bildet, wurde beschrieben und mittels Kernspinresonanz (NMR)-Studien analysiert. Die Untersuchung der Präzipitation deutete auf die Beteiligung von zwei Prozessen unterschiedlicher Kinetik hin. Die Wahl der fMLF-Modifikation erfolgte aufgrund der immunstimulierenden Eigenschaften durch Aktivierung des Formyl Peptid-Rezeptors (FPR). In Kombination mit Silica-Partikeln könnte dies als Impfstoff-Adjuvans dienen. Die Auswertung der Peptidaufnahme und -freisetzung ergab vielversprechende Resultate. Zudem wurde das immunstimulierende Potenzial mittels eines Dihydro-Rhodamin (DHR)-Assays nachgewiesen, indem die Fähigkeit zur Induktion von reaktiven Sauerstoffspezies (ROS)-Produktion und FPR-Aktivierung demonstriert wurde.

Table of contents

1 Introduction

1.1 Silicon

Silicon is at 20% the second-most abundant element on Earth, following oxygen.[2, 3] In compound form it makes up a significant part of Earth's composition, accounting for more than 75%. Among that monomineralic quartz (SiO_2) comprises a large portion, alongside other silica forms like the disordered hydrated opal and amorphous silica, which includes gels, glass, sinters, powders and skeletal materials of numerous silica secreting organisms.[4] Silicon undergoes a substantial flux in combined states of minerals and in its dissolved state as silicic acid (H_4SiO_4). At neutral pH the acid remains uncharged and is soluble up to 2 mM. Beyond that threshold polycondensation leads to colloidal particles of hydrated silica ($SiO_2 \cdot xH_2O$).[5] Rivers transport the dissolved silica to the ocean, where marine organisms such as diatoms, radiolaria, silico-flagellates and siliceous sponges utilize it for their skeletal structure.[6] Upon their demise, the silica is redissolved and assimilated by plants to stiffen leaves and stalks and reinforce protective spikes and spicules.[3, 7] While silicon exerts beneficial effects on plants, it is non-essential for their growth. Humans acquire silicon through their diet, experiencing positive impact on health, particularly in bone metabolism and connective tissue synthesis.[8] Although, the role of silicon and its status as an essential nutrient is still under scientific investigation.[9]

1.2 Diatoms and biomineralization process

Diatoms are unicellular, eukaryotic protists, that engage in photosynthesis, that is responsible for 40% of marine primary production.[10] Thereby they produce organic carbon that is consumed by the marine food webs. Moreover, about one-fifth of global primary production is carried out by diatoms, reflecting their crucial ecological role.[11-13] Diatoms are ubiquitous, with an estimated 200 000 species thriving in various water habitats worldwide.[14] The term "diatom" originates from the Greek "diatomos", meaning "cut in half", referring to their distinctive two-part cell walls made of silica.[13, 15] The rigid frustule is composed of the larger top half (epitheca) and the smaller bottom half (hypotheca), which fully enclose the protoplast. The thecae consist of a valve with a species-specific, ornate structure and several girdle bands (see **Figure 1**).[16]

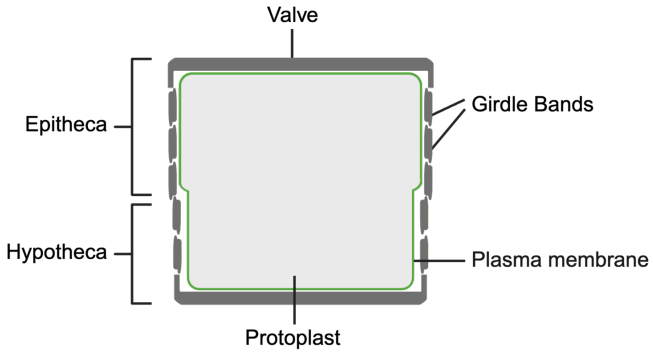

Figure 1 | The diatom structure shown in cross section. The protoplast is enclosed by the silicified cell wall, composed of two parts, the bigger epitheca and the smaller hypotheca, which are both composed of a valve and girdle bands. The diagram was created with BioRender.com.

Diatoms acquire silicon in form of silicic acid through proteins, referred to as silicic acid transporters (SIT). These transporters feature a highly conserved GXQ (X=QGR or M) sequence motif, hypothesized to play a role in silicic acid binding.[17] Diatoms have Si(IV) pools that exceed the solubility limit of 2 mM, which would result in polycondensation under abiotic conditions. It is postulated that diatoms possess specific compounds forming metastable complexes with soluble Si(IV) to prevent uncontrolled silica precipitation.[18]

Following cell division the synthesis of a new valve is initiated in a specialized intracellular compartment, the silica deposition vesicle (SDV).[19] The mechanism of transport from SIT to the SDV remains unclear, but the acidified vesicles allow polymerization of silica and expand to form a new valve. After the exocytosis of the SDV the daughter cells enclosed in a new frustule undergo separation. Upon expansion of the protoplast additional girdle bands are synthesized in SDVs–one for each girdle band–and subsequently released via exocytosis.[20]

Although the SDV was never isolated before, dissolution experiments evidenced that several organic components, including sugars and proteins, are part of the frustule.[21]

Various polysaccharides were isolated by different extraction methods.[22] Two major polysaccharide components, mannan and callose, could be identified. There is some indication that they influence the structure formation process, but are in no correlation with silica polymerization.[23] Another polysaccharide, chitin, first isolated from *Thalassiosira pseudonana*, was suggested to be involved in valve morphogenesis.[24] Since the pattern of the frustule is relayed over generations, the biomineralization process is suggested to be under genetic control. Consequently, the emphasis was placed on identifying proteins within the silica cell wall.

The first identified protein was α1-frustulin from *Cylindrotheca fusiformis*, which was later found to protect the silica cell wall against corrosion.[25] Another protein, extracted from *C. fusiformis* was pleuralin, which is strongly associated with the cell wall in the overlap region of the thecae, known as pleural bands, and protects the protoplast during cell devision.[26, 27] In *Thalassiosira pseudonana* proteins with 150 kDa could be detected upon Copper stress induction.[28] The functions of these proteins, referred to as p150, and their involvement in biomineralization remain unclarified.

However to date there are three components embedded in the cell wall that enable silica precipitation in artificial systems: the phosphoproteins silaffins, long-chain polyamines (LCPAs) and silacidins.[13]

The LCPAs are abundant components in the cell wall, consisting of repeating units of propyleneimine attached to ornithine, putrescine or other diamines, which are methylated. LCPAs are able to catalyze silica precipitation from a silicic acid solution in the presence of polyanions, such as phosphate.

That prompted the search for polyanionic components in the cell wall and resulted in the identification of the acidic protein silacidin. The precursor protein is proteolytically processed resulting in peptides rich in aspartic acid and phosphorylated serin. The combination of the negatively charged silacidin and LCPAs induces silica precipitation *in vivo*.[29]

Last but not least, the phosphoproteins silaffins are deeply embedded in the cell wall and due to their polycationic and polyanionic properties silaffins are able to induce silica precipitation without the need for additional components.[30, 31]

1.2.1 Silaffins

Silaffin proteins are located within the silica cell wall of diatoms. Their strong affinity for silica is also the origin for their nomenclature. They were first purified from *C. fusiformis* using anhydrous hydrogen fluoride (HF), dissolving the cell wall to extract the tightly bound proteins.[32] However, HF does not only dissolve silica it also cleaves O-glycosidic- and phosphate ester bonds, removing posttranslational modifications. Hence, the extraction conditions were adjusted to an aqueous solution of ammonium fluoride at pH 5 to preserve these modifications. In total nine silaffin variants, encoded by four silaffin genes, were isolated from *C. fusiformis* and *T. pseudonana*.[33] While all identified silaffins share similar posttranslational modifications, only those from *C. fusiformis* demonstrated the ability to catalyze silica formation from silicic acid solutions.[34] Silaffin-1A (4 kDA), silaffin-1B (8 kDa) and silaffin-2 (17 kDa) were detected by treating the cell wall of *C. fusiformis* with HF.[32] Based on preliminary sequence information, the *sil1* gene was successfully cloned into a cDNA library, encoding the 265 amino acid-long precursor protein sil1p.[35] It comprises an *N*-terminal signal sequence domain (amino acids 1-19) allowing translocation to the

endoplasmic reticulum, an acidic domain (amino acids 20-107) with an as yet unknown function and a basic domain (amino acids 108-257) characterized by highly repetitive units (R1–R7) and very conserved amino acid composition, enriched in lysine and serine (see **Figure 2**). The repeats are highly similar, generating three different peptides upon proteolytic cleavage, Sil-1A$_1$ derived from the units R3–R7, Sil-1A$_2$ derived from R2 and Sil-1B derived from R1. There is no indication that silaffin-2 is also encoded by the *sil1* gene.[32] Upon maturation, the RRIL- or RRNL sequences undergo cleavage, serving as a spacer between the repeats.[29]

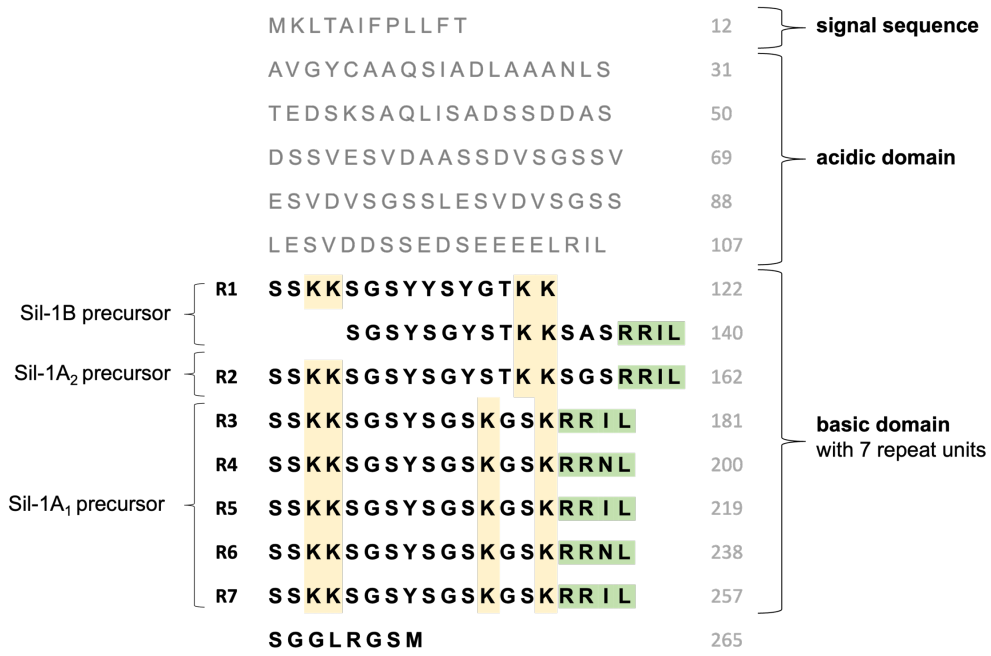

Figure 2 | Primary structure of the precursor protein sil1p. It is composed of a signal sequence (amino acids 1–19), an acidic domain (amino acids 20–107) and a basic domain (amino acids 108–257), enriched in lysine (yellow) with highly repetitive units R1–R7, which give rise to the peptides Sil-1A$_1$, Sil-1A$_2$ and Sil-1B. Upon maturation the RRIL and RRNL (green) are proteolytically cleaved.

The native silaffins exhibit many posttranslational modifications. In natSil-1A$_1$, each serine residue is phosphorylated and lysine is alkylated. In addition to the known methylation, the amino group of lysine is also modified with *N*-methylated oligo-propyleneimine chains, representing an undescribed type of protein modification. Furthermore, hydroxylation occurs at trimethylated lysine residues, followed by phosphorylation at the δ-C-position (see **Figure 3**).[21, 30]

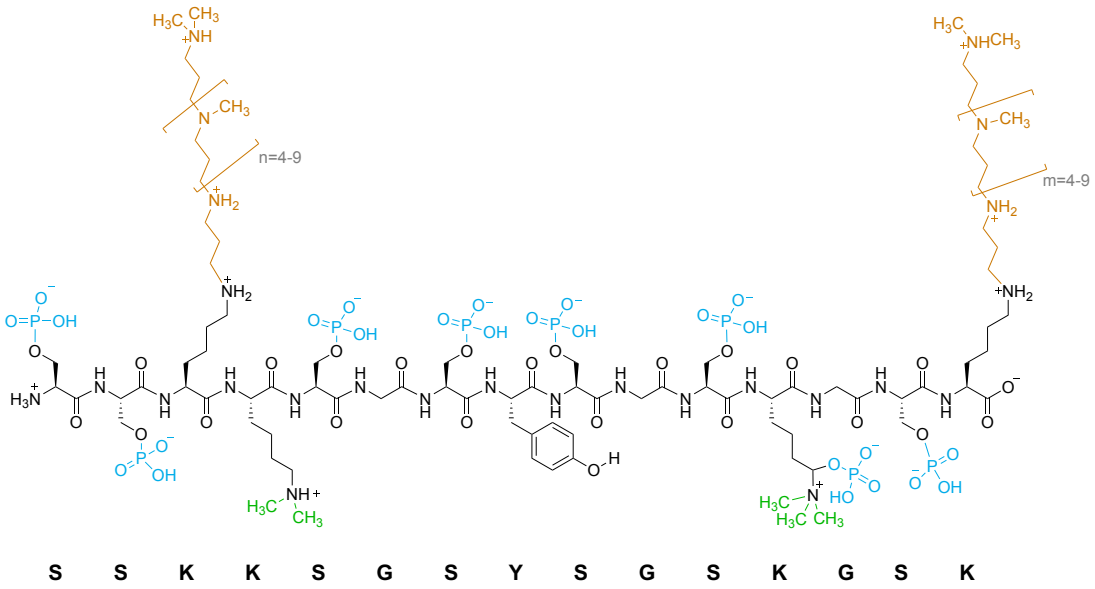

Figure 3 | Primary structure of natSil-1A$_1$ at pH=5. The peptide is modified with phosphorylations (blue), methylations (green) and *N*-methylated oligo-propyleneimine chains (ochre).

The posttranslational modifications render the peptide zwitterionic, incorporating both negative and positive charges. Silica formation requires the presence of polyvalent anions, provided by the natSil-1A$_1$ peptide through its phosphate groups. These groups engage in electrostatic interactions with the positively charged groups in the peptide, leading to self-assembly and cluster formation into a template. The process also induces microscopic phase separation, which results in microdroplets enriched in polyamine and polyanions. The amine groups are essential for polycondensation of silicic acid, facilitating the formation of siloxane bonds.[36] Consequently, dephosphorylated natSil-1A$_1$, lacking negative charges, has no silica-precipitating ability.[31] But upon addition of polyvalent anions (phosphate ions, pyrophosphate or sulfate) the silica precipitation ability is restored. Several studies showed that the peptides R1, R2 and R5 derived from sil1p are able to precipitate silica from a silicic acid solution.[21, 37]

1.2.2 The synthetic R5 peptide and variants

The R5 peptide, characterized by the sequence (H-SSKKSGSYSGSKGSK-RRIL-OH) is a synthetic variant derived from the natSil-1A$_1$ peptide. It lacks all posttranslational modifications and retains the RRIL tetrapeptide, which is typically cleaved during maturation. Upon incubation in a phosphate buffer the peptide is able to precipitate silica from a silicic acid solution (see **Figure 4**).[38] The contribution of each amino acids residue to the biomineralization process was assessed in several studies.[20, 39-41]

Although removed during maturation in vivo, truncation and mutation experiments revealed that RRIL sequence plays a crucial role in artificial silica precipitation. The positively charged guanidinium group of arginine and the hydrophobic residues leucine and isoleucine, located in close proximity, are presumed to facilitate the self-assembly. Mutation experiments, where the arginine was replaced by hydrophobic or a negatively charged amino acids, demonstrated the loss of silica precipitation capability.[39]

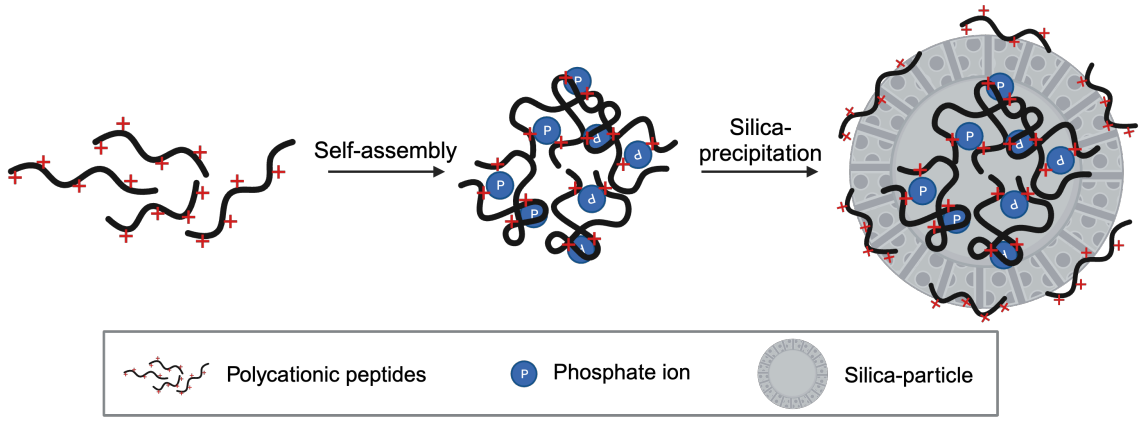

Figure 4 | Proposed mechanism of silica precipitation. The polycationic peptides self-assemble upon addition of phosphate ions. They already form a template in solution, which predetermines the silica morphology. Some peptides only lightly adhere to the surface. The diagram was created with BioRender.com.

Furthermore, the positioning of the RRIL peptide, whether at the C- or the N-terminus does not alter the ability of the resulting peptide to induce silica precipitation. Interestingly, the tetrapeptide RRIL alone lacks the capacity to precipitate silica, but the addition of lysine resulting in KRRIL can generate silica particles, albeit with reduced efficiency.[40]

This led to the concept of introducing a second RRIL tetrapeptide connected by a central lysine group. Various versions, including a linear peptide and a peptide with the second RRIL motif coupled via an isopeptide bond with lysine, were tested, as well as D-amino acid variants. All of these versions exhibited high silica precipitation efficiency, forming spherical particles similar to those produced by the original R5 peptide.[42]

During these experiments, a noteworthy discovery emerged—rod-shaped particles were observed when using the peptide K*(rrill)-RRIL, introducing a second D-Leu to the second RRIL peptide motif. Furthermore, subsequent studies revealed that changing the central L-Lys to D-Lys altered the resulting silica particles back to a spherical morphology. These findings highlight how even minor alterations can lead to significant changes in the outcome of silica particles.[1, 42]

1.2.3 Applications of biomimetic silica

Silica materials are conventionally applied in adsorption, catalysis, as a stationary phase in liquid chromatography and sensing.[43] Their traditional synthesis involves harsh temperature and pH conditions.[44] However biomimetic synthesis using silica-precipitating peptides derived from skeletal material of diatoms offer a milder alternative. This opened up new application areas, particularly in biotechnology and biomedicine, where silica particles are now being explored as delivery systems for drugs and vaccines.[45] This utilization aims to enhance therapeutic stability, facilitate cell membrane passage, and prevent rapid clearance in vivo. Silica matrices offer distinct advantages over alternative delivery systems such as liposomes, micelles or polymers.[46, 47] First and foremost, silica is considered safe and biocompatible as it degrades into non-toxic silicic acid, which can be excreted through the urinary system. The metabolized products of other delivery platforms, in contrast, are often toxic and accumulate in the body.[48] Additionally, the favorable properties of silica particles, such as high surface area, shape and morphology control, and robust chemical and thermal stability, position them as an excellent drug delivery system.[49]

The drugs can be immobilized by simple co-precipitation during silica formation, which entraps the biomolecule, or through covalent linkage to the silica-precipitating peptide.[30] The entrapment poses some problems since the encapsulation is heterogeneous and the release occurs randomly. The variant with covalent linkage to the peptide allows controlled release using stimulus-responsive linkers, such as pH or redox-sensitive linkers (see **Figure 5**).[38] Yet, due to biomolecule conjugation, the controllability of the silica precipitation is compromised and requires adjustment and reevaluation. Further research is needed to establish an effective drug delivery system, despite the remarkable advantages.

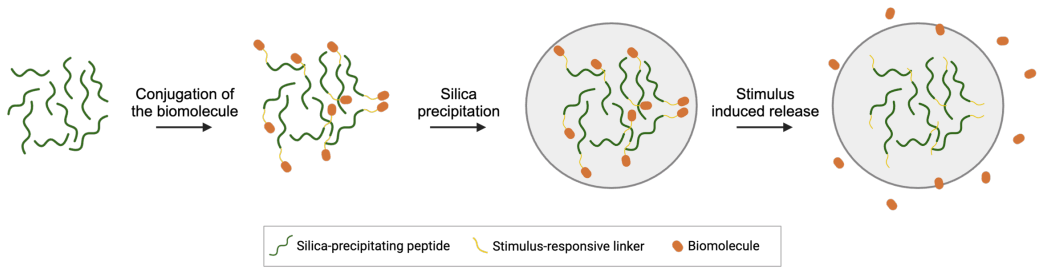

Figure 5 | Illustration of drug delivery using biomimetic silica particles. The silica-precipitating peptides are conjugated via a stimulus-responsive linker to the biomolecule and the complex is used for silica precipitation. Upon a stimulus the linker breaks and releases the biomolecule. The diagram was created with BioRender.com.

1.3 Vaccine adjuvants

Since Edward Jenner's pioneering vaccination experiment in 1796, which revealed that exposure to the milder cowpox could prevent a smallpox infection, vaccinations have played a crucial role in promoting human and animal health, saving millions of lives each year.[50] Vaccines function by stimulating an immune response that provides protection against infections or diseases before actual exposure. Generally, vaccines have to contain antigens to achieve this effect.[51] Traditional approaches involve using killed whole organism or live attenuated pathogens. While live vaccines elicit a robust immune response without real manifestation of the disease, side effects like inflammation and high production costs pose problems. Subunit vaccine, including purified and recombinant proteins, polysaccharide and peptides offer a more stable and safer alternative. However, in contrast to live vaccines they often exhibit limited immunogenicity and require adjuvants.[51]

Adjuvants, derived from the Latin word “adjuvare”, which means help or enhance, are compounds that specifically improve the immune response elicited by vaccines.[52]

Adjuvants can fulfill various roles, whereby their most crucial function is the enhancement and extension of an immune response. Moreover, adjuvants reduce the required amount of antigen per dosage, contributing to an increased vaccine supply. Their ability to elevate the immune response has promoted the development of single-shot vaccine options, minimizing the necessity for multiple doses. Furthermore, adjuvants address the challenge of pathogen variability by broadening the immune response profile. They also play a pivotal role in improving immune responses in weak immune systems, such as in newborns, elderly or immunocompromised individuals. Vaccine adjuvants have shown potential in inducing T cell differentiation, which can promote prolonged immunogenicity or stimulate T cells to kill invading pathogens [53, 54]

Adjuvants can be broadly categorized into three groups based on their application, sources and mechanism of action. These groups encompass immunomodulatory molecules, delivery systems or a combination of both.[54, 55]

In this context, it is important to mention that the efficacy of a vaccine induced immunity is dependent on the initial triggering of the innate immune system.[56, 57] The immunomodulatory molecules act on the innate immune system and adjust responses to the antigen. Thereby, they target pattern recognition receptors (PRR), such as Toll-like receptors (TLR), NOD-like receptors, etc., on immune cells that recognize pathogen-associated molecular patterns (PAMPs). These patterns include cell wall components, lipoproteins, proteins, lipopolysaccharides and nucleic acids of bacteria, virus or fungi.[58] Adjuvants in this category often consist of a combination of components to enhance effectiveness, such as cytokines, bacterial toxins or glycolipids, that alter antigen processing.[59] An approved example for an immunomodulatory molecule is monophosphoryl lipid A (MPL®), which is derived from the

lipopolysaccharide present in the outer cell membrane of gram-negative bacteria. MPL® consists of a polysaccharide ensuring solubility and the Lipid A, that can be hydrolyzed to MPL.[60] In contrast to full-length Lipid A that compound shows reduced endotoxicity and effectively induces an immune response and activates T helper type 1 (T_H1) cells.[55, 61]

The second category, delivery systems, provides efficient administration of vaccines. These systems enable depot delivery and controlled release to optimize conditions for a strong immune response. The most prominent and wildly utilized example is alum, an abbreviation for aluminum salts, like aluminum hydroxide or aluminum phosphate. The antigens adsorb the highly charged aluminum particles, which extends bioavailability and also enhances antigen presentation. Despite its extensive use, the exact mechanism of action remains unclear, but it is believed to function as a depot for continuous antigen release.[62] Additionally to the delivery function alum also exhibits immunostimulatory properties, which results in cytokine production and consequently T_H2 immune responses.[63] Therefore alum can also be accounted as a combination adjuvant. The combination of MPL® and alum, known as AS04, incorporates the advantages of both adjuvants, by increasing the immunogenicity and balancing the T_H1 and T_H2 immune cell response and also providing a delivery platform.[64]

Other licensed examples are oil-in-water emulsions MF59™ and AS03, that exhibit a dual function as a delivery system and eliciting an immune response including weak T_H1 and T_H2 response. Additionally, three more adjuvants licensed in Europe are AS01, CpG ODN 1018 and lipid nanoparticles.[65]

Despite considerate efforts to expand the repertoire of adjuvants, challenges persist, including concerns about toxicity, low batch-to-batch reproducibility, and adverse side-effects. An alternative could involve silica particles, already applied as drug delivery systems, providing some benefits including controlled characteristics such as size, morphology, and porosity and biocompatibility.[48]

1.4 Formyl peptide receptor

The Formyl peptide receptors (FPRs) are classified as G-protein coupled receptors, comprising seven transmembrane domains.[66] Additionally, they can be categorized as PRR that recognize PAMPs or damage-associated molecular pattern.[67, 68] As such, they are involved in host defense against infections and clearance of damaged host cells.

In humans, there are three variants of the receptor, including FPR1, FPR2, and FPR3.[69] FPR1 and FPR2 share a substantial sequence similarity, with 69% identity in amino acids and also demonstrating overlapping functions. Initially the receptors were only associated with myeloid cells, but they are expressed in various cell types, amongst others endothelial

cells, hepatocytes, astrocytes, microglial cells, and fibroblasts. In contrast, FPR3 is less widely distributed and predominantly expressed in monocytes and dendritic cells.[70]

The FPRs were first identified as high affinity binding sites for the *Escherichia coli* derived fMLF peptides.[71] During microbial infection, the *N*-formyl peptide is released from invading bacteria and primarily stimulates FPR1 responses. The chemoattractant properties of fMLF result in the recruitment of immune cells to the site of infection. Consequently, fMLF not only initiates chemotaxis but also facilitates innate immunity by inducing degranulation and superoxide production.[72]

However, FPR recognize a wide range of other agonists, encompassing peptides and non-peptides derived from pathogens and the host, as well as synthetic ones.[69, 73] Short *N*-formyl peptides from different bacteria exhibit higher affinity for FPR1, while FPR2 displays lower affinity for them but higher affinity for mitochondrial *N*-formyl peptides.[70] Moreover, FPR2 has a broader spectrum of agonists, including staphylococcal-derived phenol-soluble modulins, ligands produced by immunodeficiency virus (HIV) and host-derived eicosanoids, such as lipoxin A_4. Annexin, released as a danger signal from necrotic cells, is an example of a host-derived molecule recognized by all FPRs.[74] The agonists for FPR3 show limited overlap with those of the other two receptors in the family.[75]

Due to the high similarity the receptors FPR1 and FPR2 are thought to activate similar signal ways (see **Figure 6**). Upon binding of the agonist fMLF, the coupled G-protein is activated, meaning GDP is converted to GTP and the protein dissociates in a α-subunit and a $\beta\gamma$-subunit.[76] The latter activates the phospholipase Cβ (PLCβ) and phosphoinositide 3-kinase γ (PI3Kγ) pathway. PLCβ catalyzes the hydrolysis of phosphoinositol-4,5 bisphosphate (PIP_2) to generate diacylglycerol (DAG) and inositol trisphosphate (IP_3). The IP_3 diffuses to the endoplasmic reticulum membrane, where Ca^{2+} from intracellular stores is released. That triggers degranulation and together with DAG activates the protein kinase C (PKC), which is central for NADPH oxidase regulated superoxide production.[77]

PI3Kγ activates the protein kinase B (Akt), which is involved in chemotaxis, superoxide production and transcriptional regulation.[78] Moreover, PI3Kγ catalyzes the phosphorylation of membrane bound PIP_2 into phosphoinositol-3,4,5-triphosphat (PIP_3), which also activates PKC and therefore induces superoxide production.[79]

The Gα activates guanine exchange factors that induce the activation of Rho GTPases, including Rho, CDC42 and Rac, which alter the actin cytoskeleton, consequently leading to granule release and chemotaxis. Moreover, also the NADPH oxidase complex is formed to generate superoxide.[80] The activity of the Src-like tyrosine kinase is enhanced by the recruitment of PI3Kγ to the plasma membrane. That leads to association of Sos, Shc and

Grb2, which activates the Ras GTPase and the MAPK pathway, including MEKK and Raf, and further downstream p38 and ERK1/2 that regulate transcription, induce degranulation and chemotaxis.[81]

The first response at relatively low fMLF concentrations is chemotaxis, then 10-50 times higher concentrations are needed for degranulation and even higher ones for superoxide production.[69]

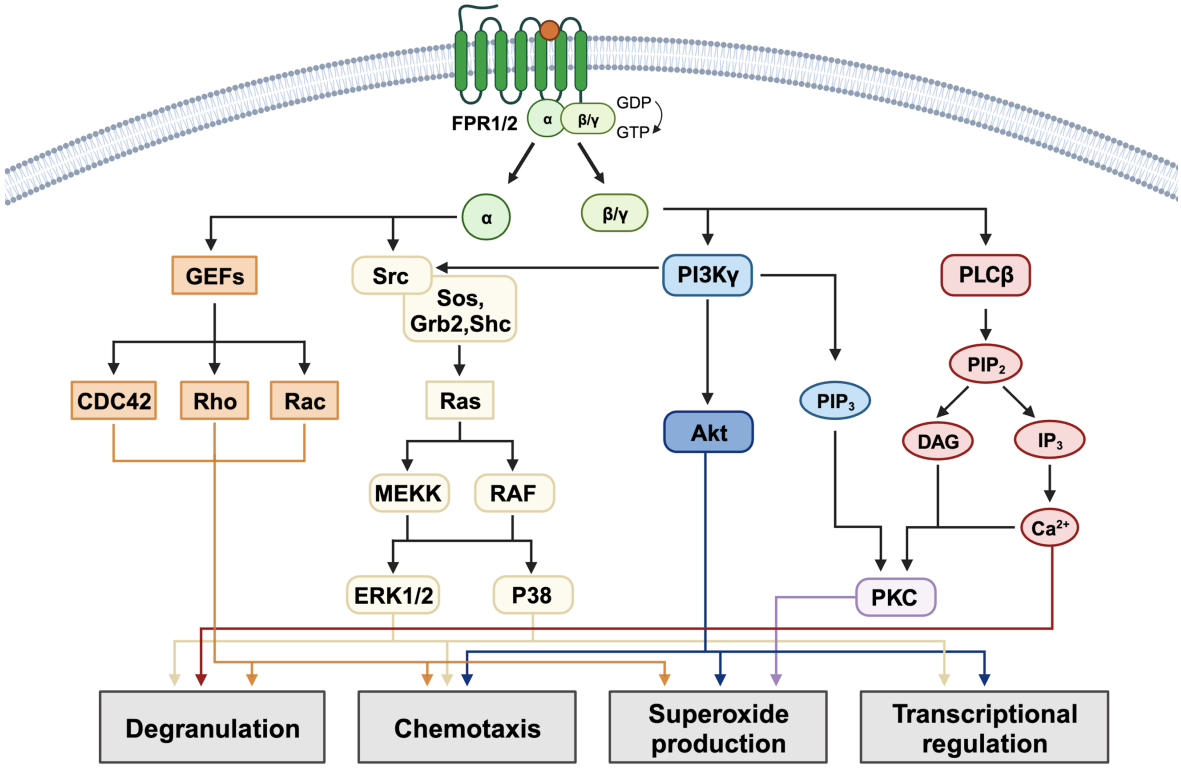

Figure 6 | FPR signal transduction. Upon binding of a ligand, the G-protein dissociates into a α-subunit and a βγ-subunit. The latter activates the PI3Kγ and the PLCβ. The PLCβ catalyzes the hydrolysis of PIP_2 to DAG and IP_3, which migrates to the ER and releases intracellular stored Ca^{2+}. That leads to degranulation and in combination with DAG the PKC is activated, which leads to superoxide production. The PI3Kγ activates Akt, which is involved in chemotaxis, superoxide and transcriptional regulation and also phosphorylates 4,5-bisphosphate to PIP_3, which also activates PKC. Moreover, PI3Kγ is involved recruited to the plasma membrane to activate Src-like kinase, which activates the MAPK pathway with signal transduction from Ras, to MEKK/RAF to ERK1/2 and P38, that leads to chemotaxis, superoxide production and transcriptional regulation. The activation of GEFs activates the Rho GTPases CDC42, Rho and Rac which alter actin cytoskeleton and therefore are involved in degranulation, chemotaxis and also form the NADPH complex for superoxide production. The diagram was created with BioRender.com.

1.5 Structural basis for fMLF binding

Although there is no crystal structure of the receptor available other experiments including site-directed mutagenesis and the construction of chimera receptors as well as

computational docking studies have been performed to study the interaction of the ligand and the receptor.[82, 83]

Point mutations showed, that some charged amino acids, including Arg84, Lys85, Arg163, Arg205, and Asp284 that are distributed in different transmembrane domains are important for the high fMLF affinity. In particular Lys85 and the Asp284 form “salt bridges” when no ligand is available. This interaction is disrupted when fMLF binds and is believed to activate the receptor.[69, 83, 84]

The structure of the *N*-formyl peptide allows strong binding to the receptor. The *N*-formyl group is recognized by Asp106, Arg201 and Arg205. The positively charged amino acids form hydrogen bonds with carbonyl oxygen of the formyl group and the methionine backbone. Moreover, Asp106 forms hydrogen bonds with the backbone amide nitrogen of fMet. The hydrophobic amino acids leucine and phenylalanine are also placed in an hydrophobic environment, which promotes the peptide binding.[85] In summary, the strong affinity of FPR1 for the fMLF peptide is facilitated by numerous hydrogen bonds and hydrophobic clusters.

2 Aims of the project

The thesis aims to explore the impact of modifications on the two stereoisomeric peptides K*(rrill)-RRIL and k*(rrill)-RRIL, derived from the silica-precipitating R5 peptide. The modifications encompass amongst others the *N*-formyl peptide fMLF coupled *via* a PEG_3 chain. The scaffold peptides K*(rrill)-RRIL and k*(rrill)-RRIL, previously described by Strobl *et al*. exhibit self-assembly in solution and form particles with two distinct morphologies.[1] The initial objective involved the synthesis of peptides based on these two scaffold peptides, incorporating modifications at either available α-amino group (see **Figure 7**).

The second goal is to examine the morphology of particles formed with the silica-precipitating peptides. After preparing particles from the peptides and clarifying their morphology, additional modifications are chosen based on these results, to comprehend and potentially predict the morphology of the resulting particles. Furthermore, peptides that generate silica particles with particularly intriguing morphologies are additional analyzed using NMR methods.

The introduction of the fMLF motif is primarily driven by its ability to stimulate the innate immune system *via* FPR activation. Specific peptides are selected to explore the potential application of the peptides and their corresponding particles as vaccine adjuvants. This encompasses studying the peptide incorporation efficiency and release, as well as assessing the activation of the FPR using a DHR assay.

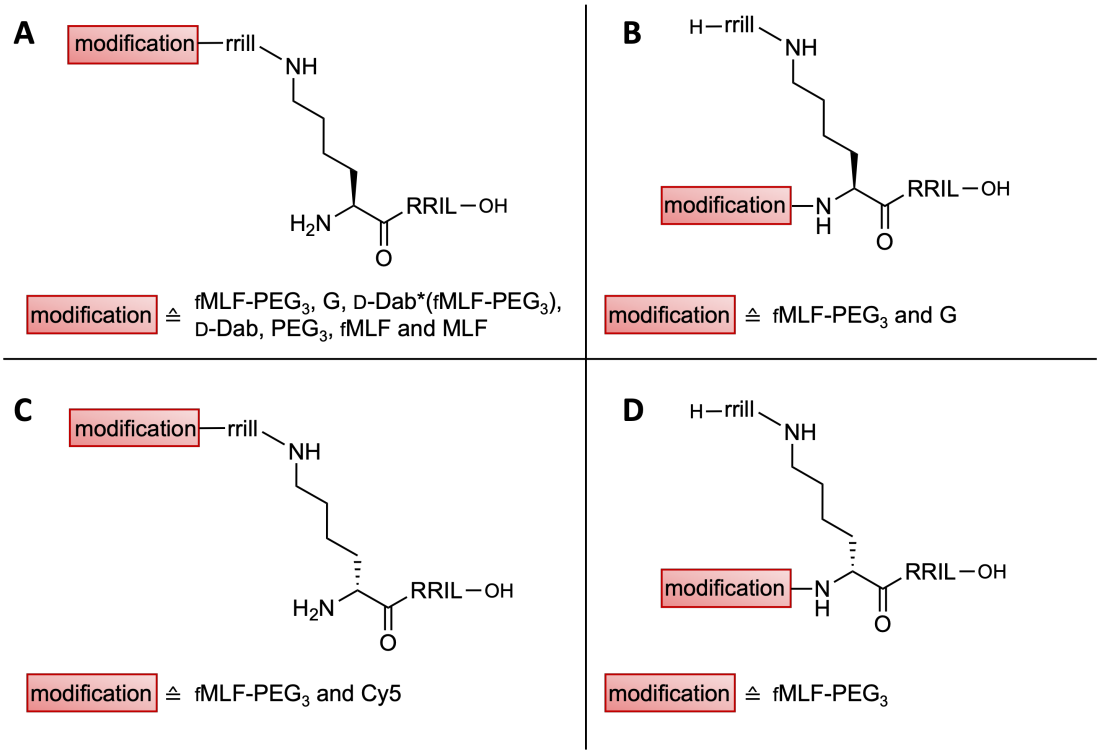

Figure 7 | Peptide constructs. (A, B) The L-Lys in the K*(rrill)-RRIL peptide (C,D) and the D-Lys in the K*(rrill)-RRIL peptide form an isopeptide bond with the *C*-terminus of D-Leu. In (A) and (C) the modification is coupled to the *N*-terminus of D-Argm whereas in (B) and (D) the modification is coupled to the *N*-terminus of lysine.

3 Materials and methods

3.1 Materials

3.1.1 Water

The water was deionized using a Professional G7895 Aqua Purificator by Miele GmbH (Salzburg, Austria) and underwent additional purification through a Milli-Q Reference A+ water purification system by Merck GmbH (Vienna, Austria).

3.1.2 Chemicals

Solvents were obtained from VWR International LLC (Vienna, Austria), Sigma-Aldrich by Merck GmbH (Vienna, Austria) and Carl Roth (Karlsruhe, Germany) in high performance liquid chromatography (HPLC)-grade or peptide synthesis grade.

Fmoc-Leu-Wang LL resin, Fmoc-Ile-OH, Fmoc-D-Ile-OH, Fmoc-Leu-OH, Fmoc-D-Leu-OH, Fmoc-Arg(Pbf)-OH and 2-(1*H*-7-Azabenzotriazol-1-yl)-1,1,3,3-tetramethyluronium hexafluorophosphate (HATU) were purchased from Novabiochem (Nottingham, United Kingdom).

Boc-Lys(Fmoc)-OH was obtained from Orpegen Peptide Chemicals GmbH (Heidelberg, Germany) and Boc-D-Lys(Fmoc)-OH from Bachem Holding (Bubendorf, Schweiz).
The other amino acids including, Fmoc-D-Arg(Pbf)-OH, Fmoc-D-Lys(Mtt)-OH, Fmoc-Lys(Mtt)-OH, Fmoc-Phe-OH, Fmoc-Met-OH, Fmoc-Gly-OH, Boc-D-Dab(Fmoc)-OH and Fmoc-NH-PEG_3-COOH were acquired from Iris Biotech (Marktredwitz, Germany).
The 4-Nitrophenyl formate (NPF) was purchased by Thermo Fisher Scientific GmbH (Vienna, Austria).

3.2 Methods

3.2.1 Automated peptide synthesis

The synthesis of the RRIL scaffold was executed by the Liberty Blue Microwave Peptide Synthesizer (CEM GmbH in Kamp-Lintfort, Germany) on a scale ranging from 0.05 mmol to 0.1 mmol. Initially, a preloaded Fmoc-Leu-Wang LL resin (substitution value: 0.31 $mmol \cdot g^{-1}$) was allowed to undergo swelling in *N,N*-Dimethylformamide (DMF) for 2 h at room temperature (RT) before introducing it to the synthesizer.
The 9-fluorenylmethoxycarbonyl (Fmoc)-protecting group removal was performed by using a solution of 20% piperidine in DMF for 40 s at 110 °C. Each individual amino acid was introduced at a concentration of 0.5 M and activated using a mixture comprised of 2 M diisopropylcarbodiimide (DIC), 0.25 M ethyl 2-cyano-2-(hydroxyimino) acetate (Oxyma), which was premixed with 0.1 M *N,N*-Diisopropylethylamine (DIPEA), all prepared in DMF solution. The equivalent ratio of amino acid to DIC to Oxyma relative to the scale was maintained at 5:12:5. The coupling of the amino acids was carried out for a brief duration of 80 s at 105 °C. After each coupling a washing step using DMF was performed.

3.2.2 Manual synthesis

The coupling of the modification motifs to the scaffold peptides were predominantly accomplished by manual synthesis. Therefore, the resin was transferred to a polypropylene syringe equipped with a polyethylene filter. As in automated synthesis, DMF was employed as the main solvent.
For deprotection, a solution containing 20% piperidine in DMF was applied for an initial duration of 3 min, followed by a subsequent 7-minute treatment after draining. Following deprotection, the resin was thoroughly washed using DMF.
The amino acids, utilized in a proportion of 5 equivalent, were dissolved in 4.76 equivalents 0.5 M HATU (*O*-(7-Azabenzotriazol-1-yl)-1,1,3,3-tetramethyluronium hexafluorophosphate) in DMF and 10 equivalents DIPEA. The dissolved amino acids were then added to the resin,

which had been drained of DMF, for 30 min incubation time. Subsequently, an additional washing step using DMF was carried out.
In the event of double coupling becoming necessary, the amino acids are activated and coupled in the same manner, without prior deprotection.
After the last coupling, the Fmoc-protecting group was removed and the resin washed with dichloromethane (DCM) to prepare for subsequent drying under vacuum and facilitate cleavage of the peptide from the resin.

3.2.3 Ninhydrin test

To confirm successful coupling the Ninhydrin test, described by Kaiser *et al.*[86] was performed. A few grains of resin were briefly washed with either methanol or DCM and then transferred to a glass vessel. To this, 2 drops of 80% (w/w) phenol in ethanol, 4 drops of 0.2 mM Kalium cyanide in pyridine, and 2 drops of 6% M ninhydrin in ethanol were added. The mixture was then heated in a block at 100 °C for 5 min.
The test is performed before Fmoc-deprotection to confirm successful coupling and the resin should show no color change. Uncoupled groups revealing free primary amine groups, would react strongly with ninhydrin and exhibit blue-colored beads. As a negative control 2-chlorotrityl chloride resin lacking amine groups or an empty glass vessel could be implemented as a uncolored reference. In contrast Fmoc-deprotected resin serves as a positive control.

3.2.4 Mtt-deprotection

The 4-Methyltrityl (Mtt)-protecting group of the amino acid lysine was selectively removed washing the resin with DCM followed by employing a solution composed of 1% trifluoroacetic acid (TFA), 1% triisopropyl silane (TIS), and 98% DCM. The deprotection solution was utilized several times for 5 min incubation time each, until the yellow tint had faded. The resin was finally washed with DMF to continue further coupling steps.

3.2.5 Methionine formylation

After Fmoc-deprotection of methionine, 6 equivalents 4-Nitrophenyl formate (NPF) (0.045 mmol, 45.1 mg) were dissolved in a minimum amount of DMF (approximately 500 µL), coupled for 3 h, and subsequently washed with DMF until the yellow undertone had faded.

3.2.6 Coupling of fluorescent dye Cy5

Following Fmoc-deprotection of D-Arg, the in-house synthesized Cyanine 5 (Cy5) was added at a ratio of 1.1 equivalents (0.02 mmol, 10.0 mg). It was dissolved in 1.05 equivalent 0.5 M HATU in DMF and 2.2 equivalent DIPEA, then introduced to the resin and incubated protected from light for 4 h. Afterwards, the resin was thoroughly washed using DMF and subsequently DCM in preparation for vacuum drying.

3.2.7 Cleavage from resin and ether precipitation

The dry resin was incubated in 20 $mL \cdot g^{-1}$ cleavage solution for 3 h at RT. In the absence of methionine, a mixture of 92.5% TFA, 5% TIS and 2.5% ddH_2O was applied, whereas if methionine was present 5% Dimethyl sulfide (DMS) were added to a mixture of 90% TFA, 2.5% TIS and 2.5% ddH_2O.

Following incubation, the cleavage solution was transferred to a threefold volume of 4 °C diethyl ether. The mixture was placed on ice for 5 min and then centrifuged at 4500 rpm for 10 min at 4 °C. After the supernatant was removed, the precipitation was repeated and the obtained pellet washed with diethyl ether. Then the pellet was dried in a nitrogen stream, dissolved in 20% solvent B (0.08% TFA in acetonitrile (ACN)) and 80% solvent A (0.1% TFA in ddH_2O) and lastly lyophilized.

3.2.8 Preparative RP-HPLC

Preparative reversed phase (RP)-HPLC purification occurred on a Waters system equipped with a Waters 2545 binary gradient module, a Waters 2489 UV/visible detector and a Waters Fraction Collector III. A Kromasil 300-10-C4 Prep Column (21.2 x 250 mm) was used as stationary phase with 0.1% TFA in ddH_2O as well as 0.08% TFA in ACN as eluents A and B. Lyophilized crude materials were dissolved in 9 mL 6 M Guanidine HCl (GuaHCl), filtered through a 0.2 µm PES syringe filter and administered to the system. The product was eluted using linear gradients from 5-15% solvent B to 50-65% solvent B in 40-50 min at a flow rate of 1 $mL \cdot min^{-1}$.

The collected fractions were then analyzed via direct injections into ESI-MS system and pooled according to the desired mass. Afterwards, the pooled product was lyophilized.

3.2.9 Analytical RP-HPLC

Analytical RP-HPLC was performed on a Dionex Ultimate 3000 HPLC system equipped with a DAD 300 detector. As a stationary phase the Waters XBridge® Protein BEH C4 column (4.6 × 150 mm) was used with solvent A and B as eluents.

The purified peptide was dissolved in a solution composed of 10% solvent B and 90% solvent A or 4 M GuaHCl and eluted at a gradient of 5-65% solvent B over a period of 30 min at a flow rate of 1 $mL \cdot min^{-1}$.

3.2.10 Mass spectrometry

Structures were characterizes by ESI (+) mass spectrometry by direct injection into a Waters Autopurification HPLC-MS system equipped with a Waters 3100 mass detector.

3.2.11 Production of silica-particles

A solution of 2 $mg \cdot mL^{-1}$ silica-precipitating peptides in 50 mM potassium phosphate buffer (pH 7) was prepared and then incubated for 3 h at RT. After that, silicic acid was prepared freshly by combining 40 µL tetramethyl orthosilicate (TMOS) with 960 µL 1 mM HCl, followed by brief vortexing and a 4 min incubation period. Then 135 µL aliquot of peptide solution was mixed with 15 µL of silicic acid and incubated for 30 min at RT. The resulting suspension was then centrifuged for 10 min at 14000 rpm at RT, followed by two washing steps with ddH_2O. The final product was dried at reduced pressure.

3.2.12 Preparation for SEM-analysis

The desiccated silica particles were suspended in 200 µL – 1 mL ddH_2O, vortexed and also pipetted up and down to dislodge any particles adhering to the tube wall. Then, 4 µl of the suspension was dabbed onto 13 mm Nunc Thermanox cell culture coverslips and dried on air. Following, sputter coating with 10 nm of gold using an EM QSG 100 instrument, scanning electron microscopy (SEM) was conducted at a 5 kV acceleration voltage utilizing a Supra 55 VP instrument equipped with an EDX detector.

3.2.13 Incorporation efficiency

During the silica-particle preparation process, two samples were gathered to assess the incorporation efficiency. Following the 3 h incubation time, 25 µL of the 2 $mg \cdot mL^{-1}$ solution of peptide in 50 mM potassium phosphate buffer pH 7, were mixed with 50 µL 6 M GuaHCl and eluted on a Kromasil 300-5-C4 short column (4.6 x 50 mm) in the Dionex Ultimate 3000 HPLC system equipped with a DAD 300 detector. After mixing the peptide solution with silicic acid and centrifugation, 25 µL were mixed with 50 µL 6 M GuaHCl and subjected to the analytical HPLC system.

3.2.14 Peptide release

The peptide release evaluation was executed in both an acidic environment (0.1 M citrate buffer, pH 4) and a physiological medium (Roswell Park Memorial Institute (RPMI) medium 1640, + L-Glutamine, pH 7.4). Thus, 300 µL of either buffer was added to a tube containing silica-particles prepared from a 135 µL peptide solution with 15 µL silicic acid (as described in **3.2.11**). After vortexing to assure no particles are adhering to the wall, the suspension was distributed equally in 90 µL portions, which were incubated at 37 °C at 400 rpm. After 1 h, 5 h and 24 h the tube was centrifuged for 10 min at 14000 rpm on a Table-top centrifuges by Eppendorf Austria GmbH. Subsequently, 65 µL of the supernatant was combined with 130 µL 6 M GuaHCl. The resulting mixture underwent another centrifugation step, ensuring no particles were subjected to the analytical HPLC system. The samples were eluted on a Kromasil 300-5-C4 short column (4.6 x 50 mm) on a Dionex Ultimate 3000 HPLC system equipped with a DAD 300 detector.

3.2.15 DHR assay (performed by SyntabTherapeutics)

For the assay human leukocytes were isolated from heparinized blood using dextran sedimentation and hypotonic lysis to remove erythrocytes. Subsequently, the cells were counted, centrifuged and resuspended in Hank's buffer with HEPES (HHBS) to obtain a cell concentration of 1.25 million cells·mL^{-1}. For the assay 15 mL of that solution were mixed with 67.5 µL 29 mM DHR, 93.8 µL 200 U·µL^{-1} catalase and 18.8 µL 21 mM cytochalasin B. The mixture was then divided in 200 µL proportions and pre-incubated at 37 °C for 10 min. The peptides were dissolved in phosphate buffer saline (PBS), and also the corresponding particles of the peptides were suspended in PBS. Then from both dilution series in cell suspension were prepared. The peptide concentration in the particles was estimated by the incorporation efficiency.

The cells were treated with the different effector concentrations and controls, followed by incubation at 37 °C for 15 min.

For the analysis with Fluorescence activated cell sorting (FACS), the cells were transferred to tubes containing 83.3 µL 4% formalin and 33 µL 50 µg·mL^{-1} Hoechst 33258 was added.

3.2.16 Data analysis

The analysis of MS and HPLC data was conducted using OriginPro® 2018 Graphs for peptide release and the cellular assay were generated using GraphPad Prism version 10.0.2 (171) for Mac OS X. Particle diameters and lengths were determined using the image processing package Fiji.[87] The scale indication was measured, and 20 randomly distributed diameters or lengths were subsequently measured. The ratio of the scale mark to the measured values was utilized to calculate the actual measurements.

4 Results and discussion

4.1 Overview of silica-precipitating peptides and synthesis strategy

The silica-precipitating peptides were synthesized based on two scaffold peptides: the K*(rrill)-RRIL peptide with an isopeptide bond between the ε-amino group of L-Lys and the *C*-terminus of D-Leu, capable of producing rod-shaped silica particles, and the k*(rrill)-RRIL also with an isopeptide bond but based on D-Lys, known for generating spherical silica particles, as previously outlined by Strobl *et al*.[1] While the precise mechanism of silica formation is not completely elucidated, the current understanding suggests that polycationic peptides participate in electrostatic interactions with phosphate ions in a buffer solution. These interactions facilitate the self-assembly of peptides in solution, serving as a template, which predetermines the silica morphology.[40]

To elucidate the impact of *N*-terminal modifications of K*(rrill)-RRIL and k*(rrill)-RRIL on the silica particle morphology, a small library of peptides was produced. It comprised various *N*-terminal modifications of the linear segment or the branch among them *N*-formyl peptide fMLF attachment. Further investigations involved the synthesis of additional variants of silica-precipitating peptides with different modification patterns aiming to enhance the understanding and potentially predict the morphology of the resulting particles. All variants are specified in **Table 1**.

Table 1 | Overview of all synthesized silica-precipitating peptides. The sequence is depicted as a simplified structural formula as well as the primary sequence, whereas the * indicates an isopeptide bond of the lysine ε-amine. The lowercase letters represent D-amino acids and the uppercase letters L-amino acids. The f in smaller font characterizes formylation.

Primary sequence	Peptide #	Structure	Molecular weight / g·mol^{-1}
K*(rrill)-RRIL	**1**	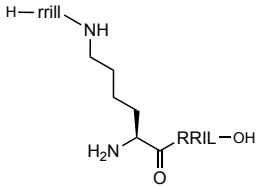	1336.8
k*(rrill)-RRIL	**2**	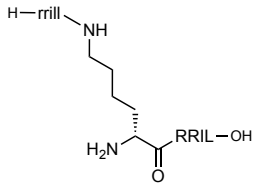	1336.8

fMLF-PEG$_3$-K*(rrill)-RRIL	**3**	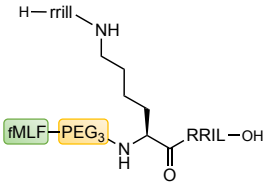	1959.5
K*(fMLF-PEG$_3$-rrill)-RRIL	**4**	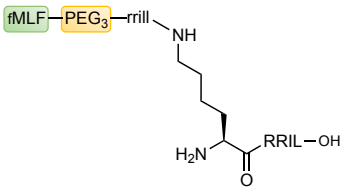	1959.5
fMLF-PEG$_3$-k*(rrill)-RRIL	**5**	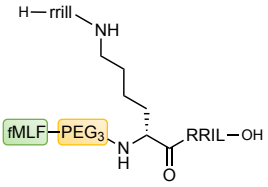	1959.5
k*(fMLF-PEG$_3$-rrill)-RRIL	**6**	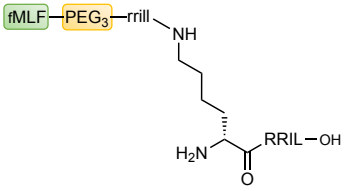	1959.5
GK*(rrill)-RRIL	**7**	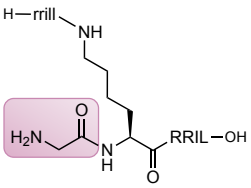	1393.8
K*(Grrill)-RRIL	**8**	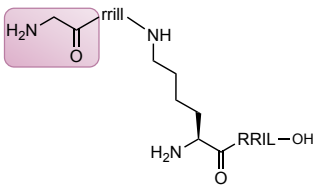	1393.8
K*(D-Dab*(fMLF-PEG$_3$)-rrill)-RRIL	**9**	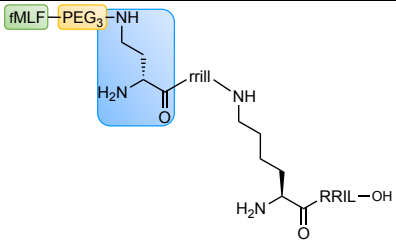	2059.7

K*(D-Dab-rrIlI)-RRIL	**10**	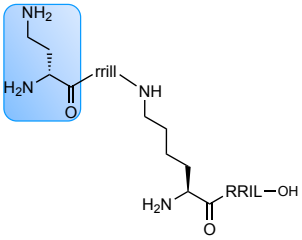	1436.9
K*(PEG$_3$-rrIlI)-RRIL	**11**	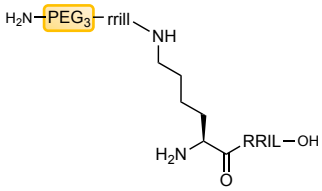	1540.0
K*(fMLF-rrIlI)-RRIL	**12**	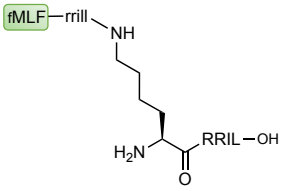	1756.3
K*(MLF-rrIlI)-RRIL	**13**	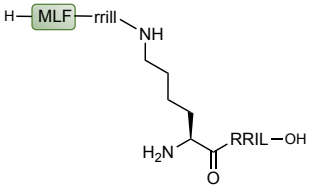	1728.3
k*(MLF-rrIlI)-RRIL	**14**	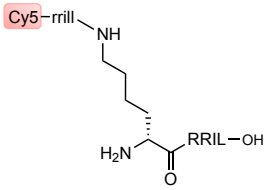	1788.4

All peptides were synthesized by SPPS using a synthesizer for the scaffold peptides and manual synthesis for further modifications, as described in **section 3.2.1** and **section 3.2.2**. Due to the different positions of the modifications, two distinct strategies based on rationally selected Lys protecting groups were established to synthesize the peptide variants.

The synthesis route to generate peptides elongated at the *N*-terminus of the lysine residue is illustrated in **Figure 8**. Initially, the five *C*-terminal amino acids were synthesized via automated synthesizer, ending in either Fmoc-L-Lys(Mtt)-OH or Fmoc-D-Lys(Mtt)-OH. Manual synthesis was employed for coupling the building blocks of the modification on the *N*-terminus of lysine. The orthogonality of the Mtt protecting group to the Fmoc-protecting

group, allows the selective deprotection under acidic conditions, following the completion of coupling steps for the modification on the lysine *N*-terminus. Ultimately, the resin was reintroduced to the synthesizer and the D-amino acids on the lysine side chain were coupled.

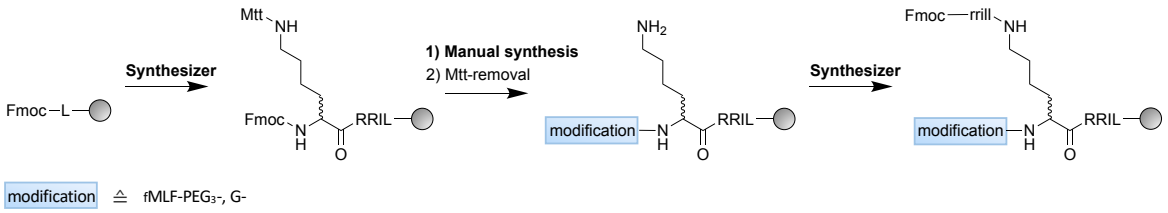

Figure 8 | Synthesis route 1 for the modification at the *N*-terminus of D-Lys or L-Lys. The first five amino acids were synthesized *via* automated synthesizer. Subsequently each building block featured in the modification was manually coupled, and the D-amino acids were coupled *via* automated synthesis following Mtt-deprotection.

The building blocks used in automated synthesis at a scale of 0.1 mmol, following synthesis route 1 are listed in **Table 2**. All amino acids are applied at a concentration of 0.5 M and as 5 equivalents relative to the synthesis scale. For arginine residues double coupling was employed.

Table 2 | Table of amino acids used to generate the scaffold peptide to introduce modifications at the *N*-terminus of D-Lys or L-Lys at a scale of 0.1 mmol. The first synthesis refers to the coupling of the *C*-terminal domain, ending with lysine, where the modification is coupled manually and subsequently the second synthesis is characterized by the reintroduction to the automated synthesizer.

Amino acid	Molecular weight / g·mol^{-1}	Volume / mL	Mass / g
First synthesis on automated synthesizer			
Fmoc-Ile-OH	353.41	2	0.36
Fmoc-Arg(Pbf)-OH	648.77	5	1.63
Fmoc-Lys(Mtt)-OH	624.77	2	0.62
Second synthesis on automated synthesizer			
Fmoc-D-Leu-OH	353.41	3	0.54
Fmoc-D-Ile-OH	353.41	2	0.36
Fmoc-D-Arg(Pbf)-OH	648.77	5	1.63

The chemicals listed in **Table 3** are involved in some modification. The PEG_3 linker is dissolved in 0.5 M HATU in DMF (3.81 equivalents) and DIPEA (8.0 equivalents). The NPF is dissolved in a minimal amount of DMF, approximately the same volume as used for amino acid dissolution. The Cy5 was produced in-house and only limited quantity was available, hence, it was applied in only 1.1 equivalents. Its dissolution involved 0.5 M HATU in DMF (1.05 equivalents) and DIPEA (2.2 equivalents).

Table 3 | Table of chemicals utilized for generating modified peptides. For PEG_3 and fMLF a scale of 0.045 mmol and for Cy5 a scale of 0.02 mmol was employed.

Chemical	Molecular weight / g·mol^{-1}	Equivalents	Mass / mg
Fmoc-NH-PEG_3-COOH	443.49	4.0	79.8
4-Nitrophenyl formate	167.12	6.0	45.1
Cy5-COOH	469.65	1.1	10.0

In **Table 4** the amino acids employed for manual synthesis are listed. The amino acids were utilized at 5 equivalents and dissolved in 0.5 M HATU in DMF (4.76 equivalents) and DIPEA (10 equivalents).

Table 4 | Table of amino acids used in manual synthesis. The amino acids (5 equivalent) were dissolved in 0.5 M HATU in DMF (4.76 equivalents) and DIPEA (10 equivalents).

Amino acid	Molecular weight / g·mol^{-1}	Mass / mg
Fmoc-Phe-OH	387.43	87.2
Fmoc-Leu-OH	353.41	97.5
Fmoc-Met-OH	371.45	83.6
Fmoc-Gly-OH	297.31	66.9
Boc-D-Dab(Fmoc)-OH	440.50	99.1

The second strategy employed for the generation of peptides modified at the *N*-terminus of D-Arg was performed in two steps, as outlined in **Figure 9**. First, the scaffold peptide was synthesized using a synthesizer, utilizing either Boc-L-Lys(Fmoc)-OH or Boc-D-Lys(Fmoc)-OH. The orthogonality of the Boc- and the Fmoc-protecting groups enables the formation of

an isopeptide bond. Subsequently, the building blocks of the modification were coupled manually.

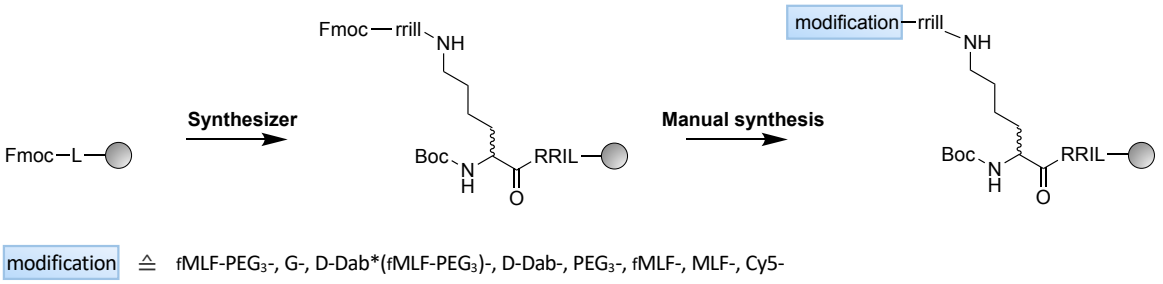

Figure 9 | Synthesis route 2 for the modification at the *N*-terminus of D-Arg. The scaffold peptide was synthesized using an automated synthesizer, with subsequent manual coupling of the building blocks featured in the modification.

In **Table 5** the amino acids employed in automated synthesis at a scale of 0.1 mmol, following synthesis route 2, are outlined. Each amino acid was used at a concentration of 0.5 M and at 5 equivalents relative to the synthesis scale. Arginine residues underwent double coupling. Additionally, the building blocks used for manual synthesis at a scale of 0.045 mmol are listed in **Table 3** and **Table 4**.

Table 5 | Table of amino acids used to synthesize scaffold peptides for introduction of a modification at the *N*-terminus of D-Arg at a scale of 0.1 mmol. All amino acids are coupled using automated synthesis.

Amino acid	Molecular weight / g·mol^{-1}	Volume / mL	Mass / g
Fmoc-Ile-OH	353.41	2	0.36
Fmoc-Arg(Pbf)-OH	648.77	5	1.63
Boc-Lys(Fmoc)-OH	468.54	2	0.47
Fmoc-D-Leu-OH	353.41	3	0.54
Fmoc-D-Ile-OH	353.41	2	0.36
Fmoc-D-Arg(Pbf)-OH	648.77	5	1.63

After synthesis, the peptides were cleaved from the resin and simultaneously global deprotection of the functional groups was conducted using a mixture of TFA, TIS and ddH_2O with optional DMS. Then the peptides were precipitated using 4 °C diethyl and lyophilized (refer to **3.2.7**). Subsequently, preparative RP-HPLC was employed for purification, as

described in **3.2.8**. After, lyophilization the peptides were assessed using an analytical RP-HPLC system and direct injections on an MS system (compare **3.2.9** and **3.2.10**). Finally, the purified peptides were utilized for silica precipitation and the morphology of the resulting particles was then examined using SEM, as described in **3.2.11** and **3.2.12**.

The upcoming sections provide a comprehensive description of the results for both peptides and the corresponding particles. The yields mentioned are based on theoretical yields relative to the synthesis scale and encompass peptide products with a purity exceeding 90% from both main and pure side pools. In the particle production, only peptides with a purity surpassing 95% were employed, supported by both MS and HPLC data confirming the purity of the peptides. Additionally, the SEM results feature four images, to provide a comprehensive overview of various sections of the analyzed grid.

4.1.1 Peptide 1

The peptide **1** was synthesized by synthesizer at a scale of 0.1 mmol (see **Figure 10**). However, only 0.015 mmol were subjected to purification since the remaining product was used for subsequent modifications. The yield amounted to 14.1 mg (70.5% of theoretical yield).

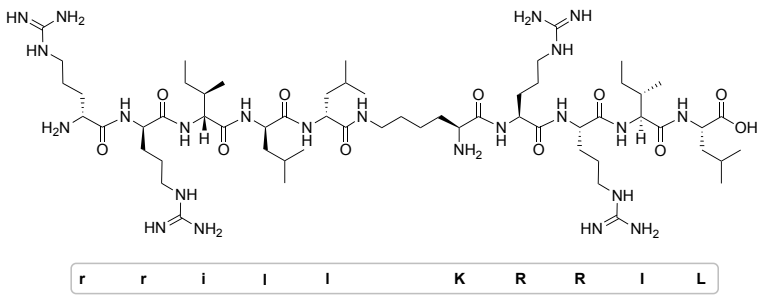

Figure 10 | Detailed structure of peptide 1. The L-Lys forms an isopeptide bond with D-Leu.

In **Figure 11** the HPLC data is depicted and shows one sharp single peak at 214 nm, indicating a pure product. The mass spectrum exhibits two peaks $[M+2H]^{2+}$ and $[M+3H]^{3+}$, which are in line with the calculated mass of 1336.8 Da and thereby confirming the correct product.

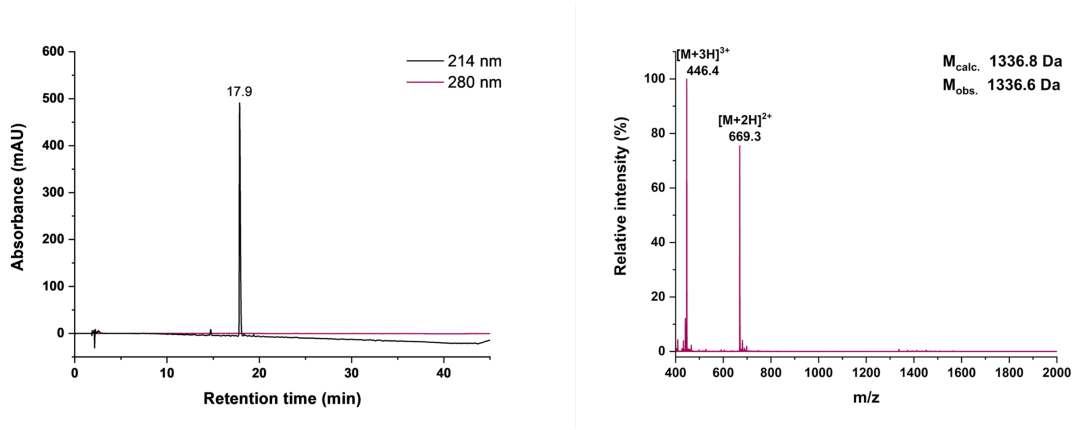

Figure 11 | Final analysis of peptide 1 with the sequence K*(rrill)-RRIL. HPLC chromatogram (left) and ESI-MS spectrum (right).

The peptide was then utilized for silica precipitation, resulting in the formation of rod-shaped particles, as already described by Strobl *et al.*[1] The particles exhibit lengths varying between 0.95–4.17 µm, with a relatively uniform diameter of 0.12 µm. The surface appears smooth and the particles tend to aggregate into clusters (see **Figure 12**).

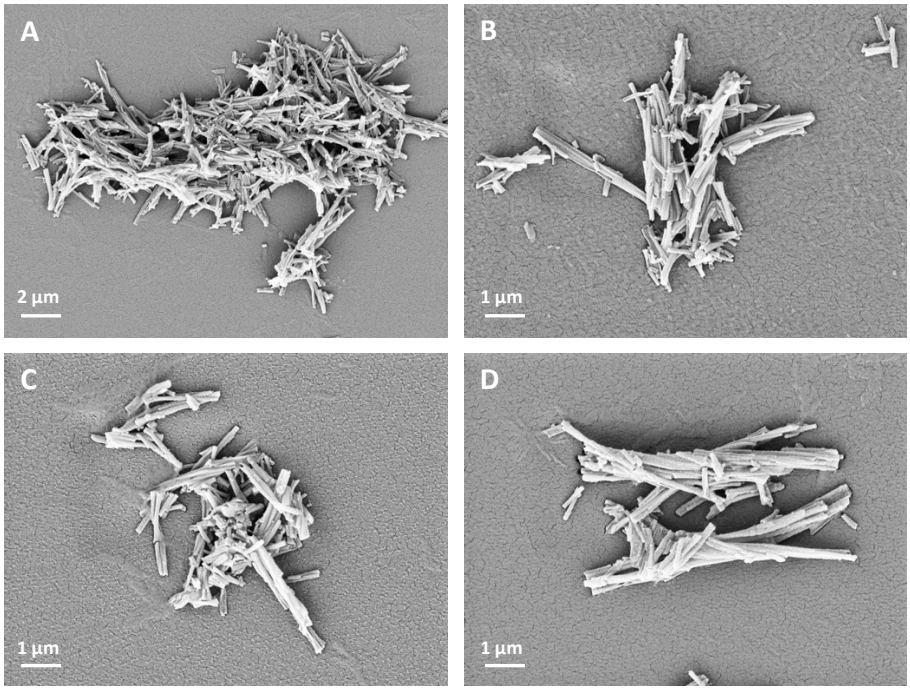

Figure 12 | SEM results of particles derived from peptide 1 with the sequence K*(rrill)-RRIL. The produced particles are rod-shaped.

4.1.2 Peptide 2

The peptide **2** (see **Figure 13**) was completely synthesized utilizing a synthesizer on a 0.1 mmol scale. Then 0.02 mmol thereof were cleaved off the resin and purified to yield 16.7 mg yield (62.5% yield).

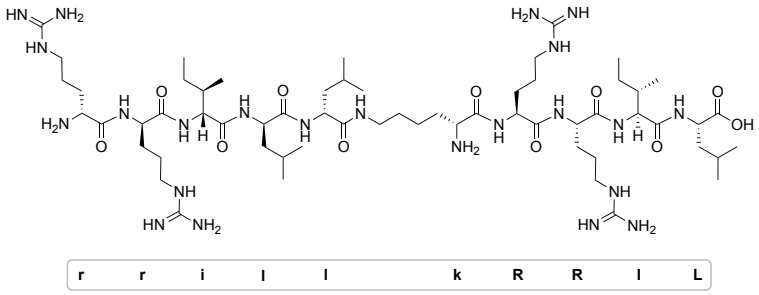

Figure 13 | Detailed structure of peptide 2. The D-Lys forms an isopeptide bond with D-Leucine.

The chromatogram in **Figure 14** shows one single peak at the 214 nm trace, revealing purity exceeding 95%. The mass spectrum aligns with the anticipated mass pattern, including $[M+2H]^{2+}$ and the $[M+3H]^{3+}$, consistent with the calculated mass of 1336.8 Da.

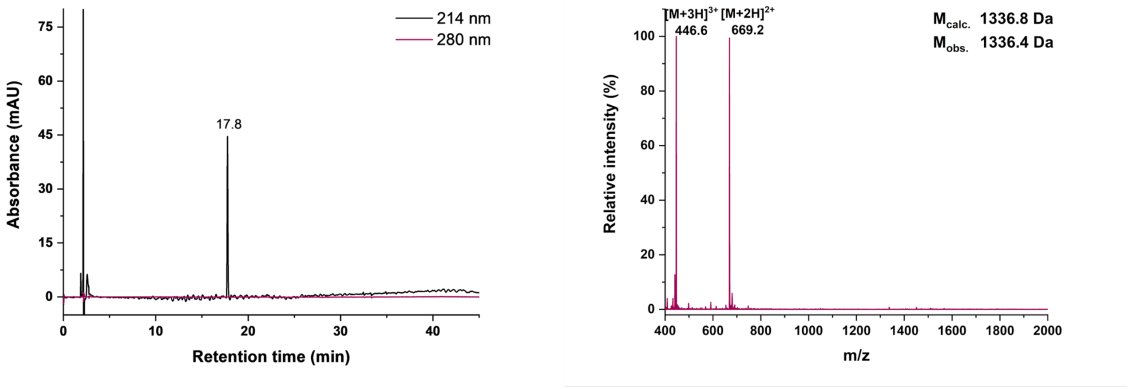

Figure 14 | Final analysis of peptide 2 with the sequence k*(rrill)-RRIL. HPLC chromatogram (left) and ESI-MS spectrum (right).

The purified peptide was used for the production of silica particles, which exhibit a spherical morphology (see **Figure 15)**, as reported by Strobl *et al*.[1] Upon closer inspection, it becomes evident that the particle diameter is unevenly distributed, ranging between 480–690 nm. The precise determination of the diameter proved to be challenging due to the cluster formation and fusion of some particles.

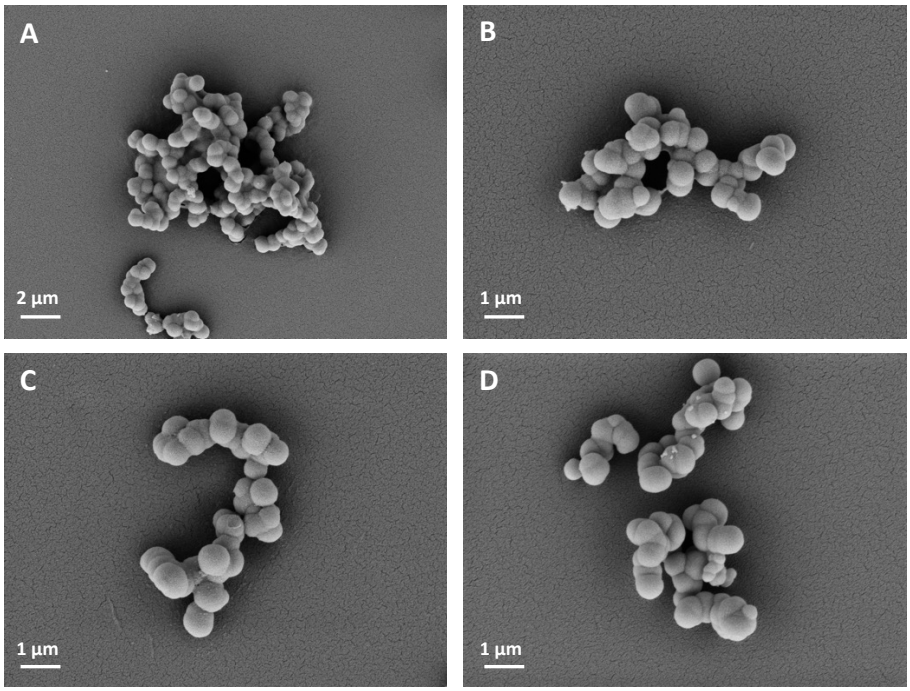

Figure 15 | SEM results of particles derived from peptide 2 with the sequence k*(rrill)-RRIL. The produced particles display spherical morphology.

4.1.3 Peptide 3

The peptide **3** is based on the peptide **1** scaffold, while additionally an fMLF motif was coupled via a PEG_3-linker to the *N*-terminus of L-Lys (see **Figure 16**). The peptide was synthesized following route 1 (see **Figure 8**) at a scale 0.045 mmol and was obtained in a yield of 55.0 mg (62.4% theoretical yield).

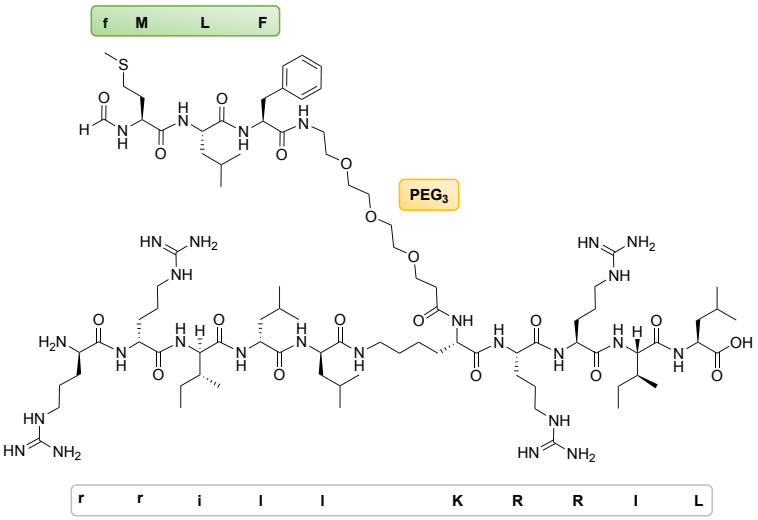

Figure 16 | Detailed structure of peptide 3. The L-Lys forms an isopeptide bond with D-Leu and provides a modification site at the *N*-terminus for PEG_3 (yellow), which serves as a linker for the fMLF-motif (green).

The chromatogram (see **Figure 17**) displays a solitary peak at the 214 nm trace indicating high purity. The mass spectrum encompassing $[M+2H]^{2+}$, $[M+3H]^{3+}$ and $[M+4H]^{4+}$ is consistent with the calculated mass of 1959.5 Da.

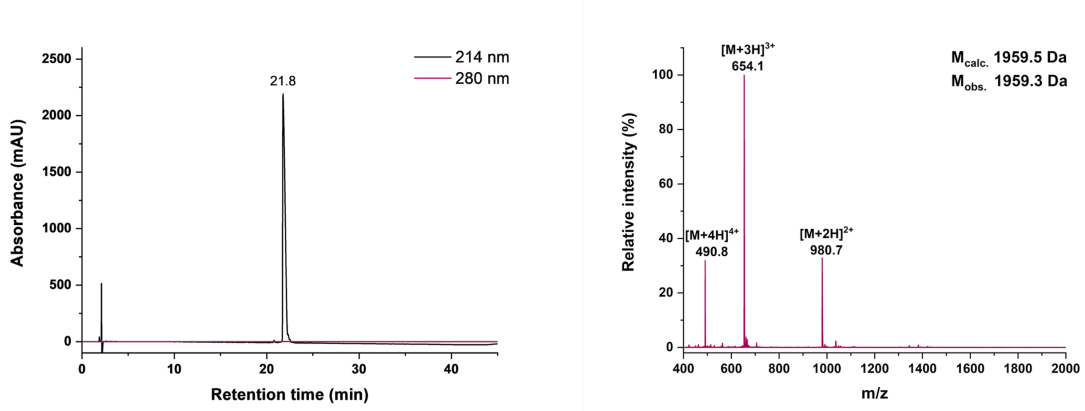

Figure 17 | Final analysis of peptide 3 with the sequence fMLF-PEG_3-K*(rrill)-RRIL. HPLC chromatogram (left) and ESI-MS spectrum (right).

The particles generated with peptide **3** form spheres with a smooth surface and a diameter of approximately 720–950 nm (see **Figure 18**). The particles assemble in clusters and some appear to be fused together, which biased the accurate diameter determination.

The morphology is distinctly different from the scaffold peptide **1**, which typically forms rod-shaped silica particles. The observed morphology disparity suggests that the fMLF-motif and/or the PEG_3-chain may have an influence on the morphological properties of the

particles. Moreover, the position of the modification could also contribute to the observed distinction.

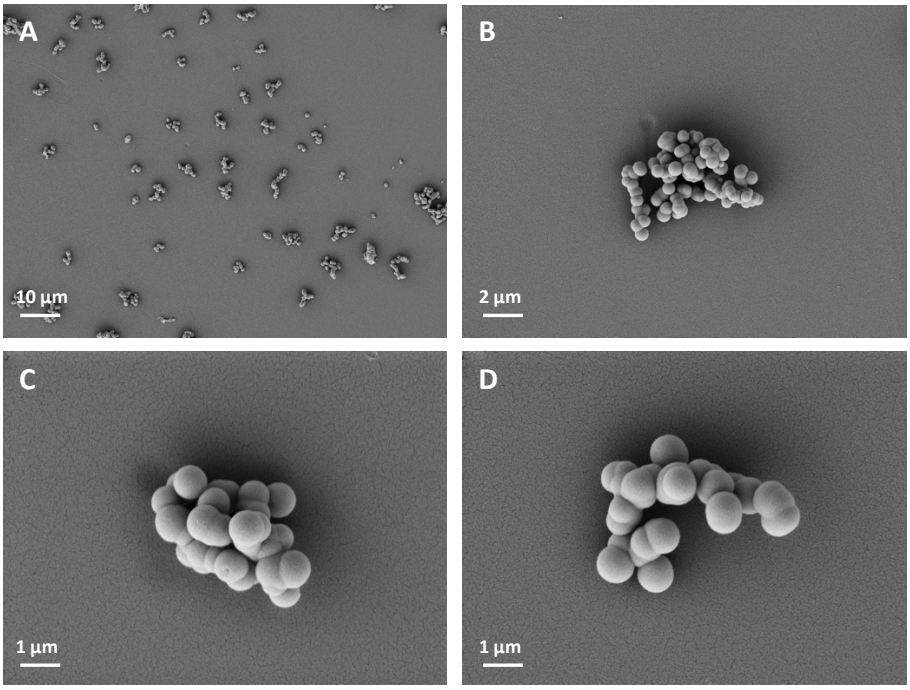

Figure 18 | SEM results of particles derived from peptide 3 with the sequence fMLF-PEG$_3$-K*(rrill)-RRIL. The produced particles display spherical morphology.

4.1.4 Peptide 4

Similarly to peptide **3**, peptide **4** is based on the scaffold peptide **1**, but the fMLF motif is coupled to the *N*-terminus of D-Arg (see **Figure 19**).

The peptide was synthesized at a scale of 0.045 mmol yielding 23.4 mg (26.6% theoretical yield), following the route outlined in **Figure 9**. The D-amino acids of the modification were single coupled, leading to deletions and comparatively modest yield of the desired product.

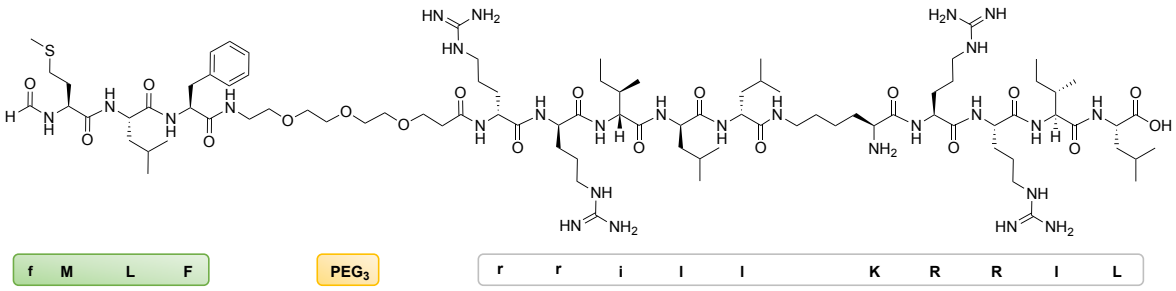

Figure 19 | Detailed structure of peptide 4. The L-Lys forms an isopeptide bond, and the fMLF-motif (green) is coupled *via* PEG$_3$ (yellow) to the *N*-terminus of D-Arg.

Analytical HPLC (see **Figure 20**) was employed to assess the purity of the product, revealing a single peak at the 214 nm trace. The mass spectrum confirmed the correct product with the observed mass pattern aligning with the calculated mass of 1959.5 Da.

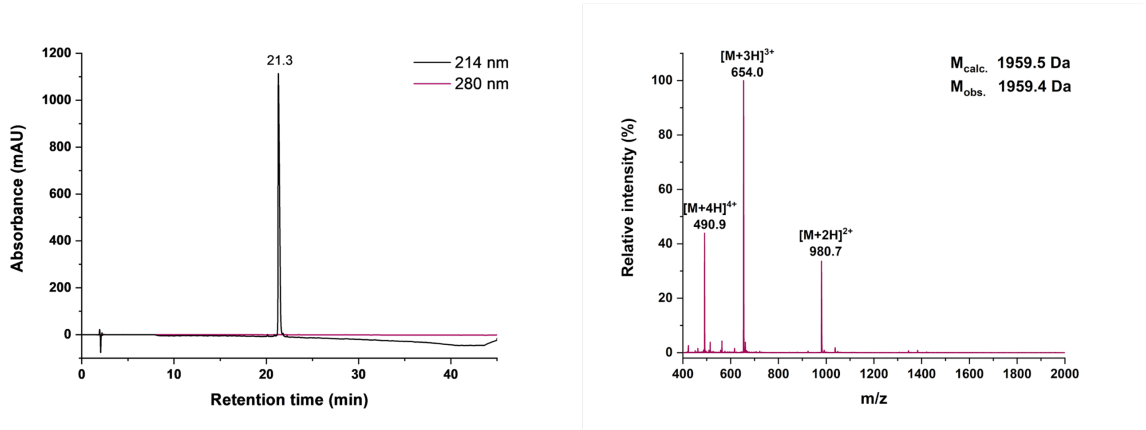

Figure 20 | Final analysis of peptide 4 with the sequence K*(fMLF-PEG$_3$-rrill)-RRIL. HPLC chromatogram (left) and ESI-MS spectrum (right).

The silica particles produced with peptide **4** exhibit a spherical shape with a diameter unevenly distributed between 520–840 nm (see **Figure 21**) and they readily aggregate to clusters. In comparison to the particles derived from peptide **3**, these appear smaller, more heterogenous and their surface seems fuzzier. But overall, both types of particles form

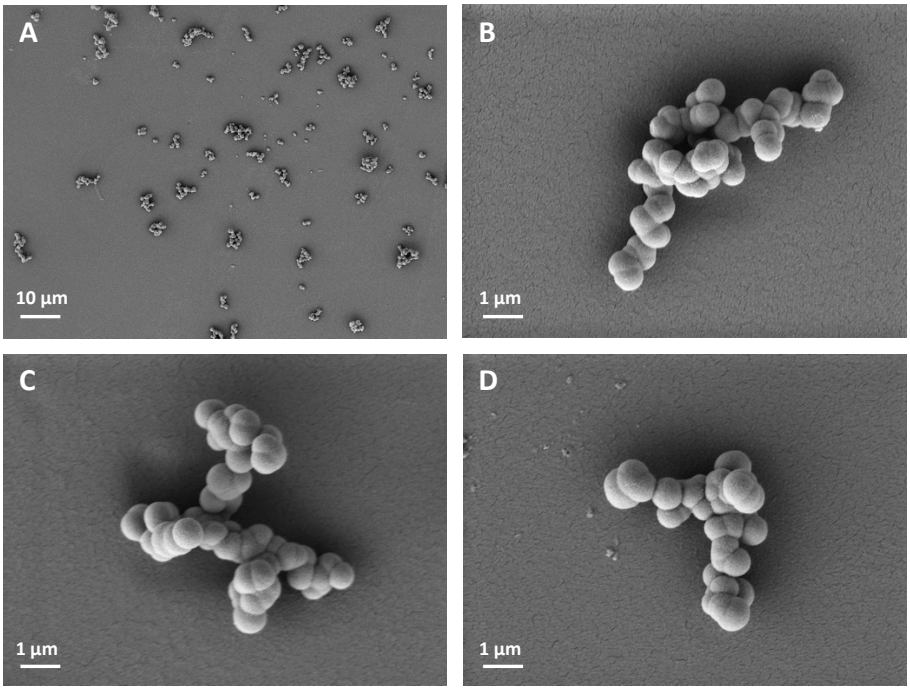

Figure 21 | SEM results of particles derived from peptide 4 with the sequence K*(fMLF-PEG$_3$-rrill)-RRIL. The produced particles display spherical morphology.

spheres, supporting the presumption that the modification affects the morphology of the particles, probably independent of the position in the peptide.

4.1.5 Peptide 5

The peptide **5** is the diastereomer to peptide **3** with a D-Lys that introduces an isopeptide bond. The scaffold is grounded in peptide **2**, but due to the incorporation of the fMLF motif on the *N*-terminus of D-Lys the synthesis follows the synthesis route depicted in **Figure 8**. The yield of the peptide **5** (see **Figure 22**) amounts to 11.5 mg (13.1% theoretical yield) at a synthesis scale of 0.045 mmol. The relatively small yield attributes to poorly separatable side products.

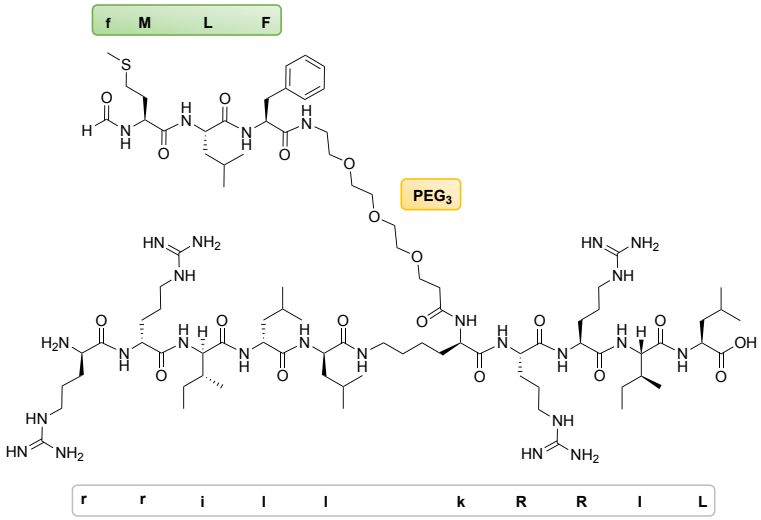

Figure 22 | Detailed structure of peptide 5. The D-Lys forms an isopeptide bond and provides a modification site at the *N*-terminus for PEG_3 (yellow), which serves as a linker for the fMLF-motif (green).

The chromatogram, depicted in **Figure 23**, reveals a singular peak accompanied by a broad plateau at the baseline at the 214 nm trace. However, the final product exhibits the correct mass pattern consistent with the calculated mass of 1959.5 Da.

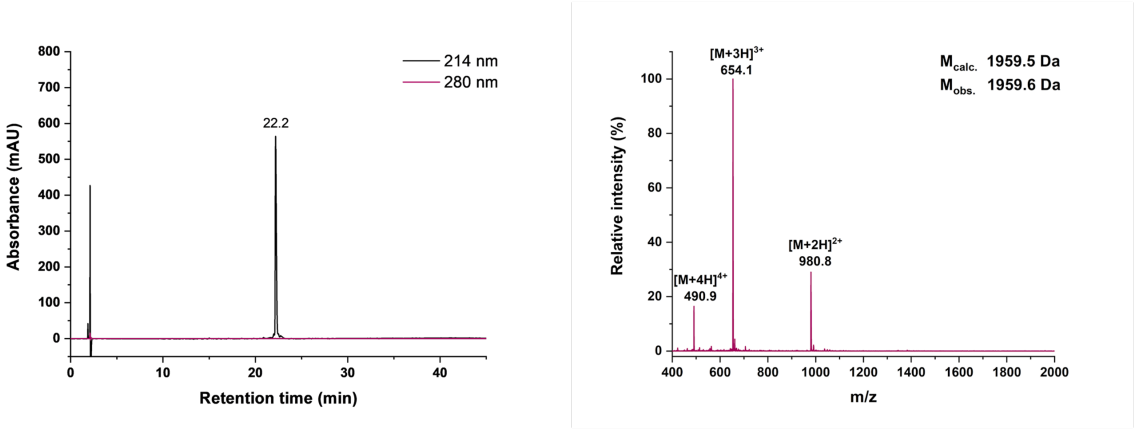

Figure 23 | Final analysis of peptide 5 with the sequence fMLF-PEG$_3$-k*(rrill)-RRIL. HPLC chromatogram (left) and ESI-MS spectrum (right).

The generated particles exhibit the anticipated spherical morphology with an irregularly diameter ranging from 660–830 nm (see **Figure 24**). Moreover, the particles occur in clusters, with some particles fused together. The observation of the spherical morphology aligns with the inherent spherical nature of the particles produced by the k*(rrill)-RRIL scaffold peptide. As described previously, the modification influences the particle shape, favoring the manifestation of spherical particles.

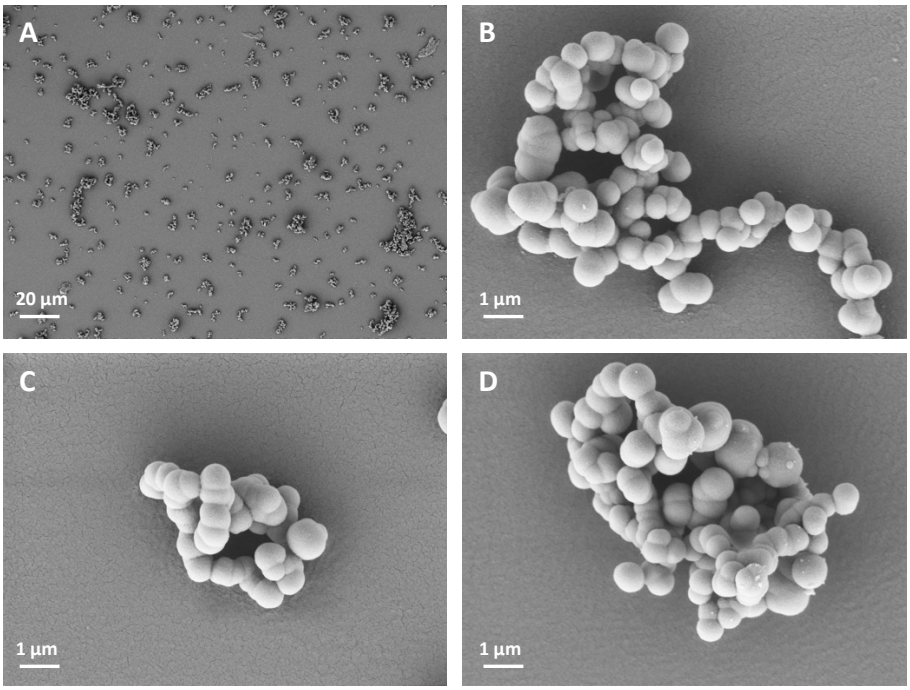

Figure 24 | SEM results of particles derived from peptide 5 with the sequence fMLF-PEG$_3$-k*(rrill)-RRIL. The produced particles display a spherical morphology.

4.1.6 Peptide 6

The peptide **6** (see **Figure 25**) represents the diastereomer counterpart to peptide **4**, featuring a D-Lys residue with the fMLF motif coupled at the same position. The synthesis of the scaffold peptide **2** was performed via synthesizer at a scale of 0.1 mmol, and then 0.035 mmol were withdrawn for manual synthesis (see **Figure 9**). The yield amounted to 44.6 mg, corresponding to a high theoretical yield of 65.0%.

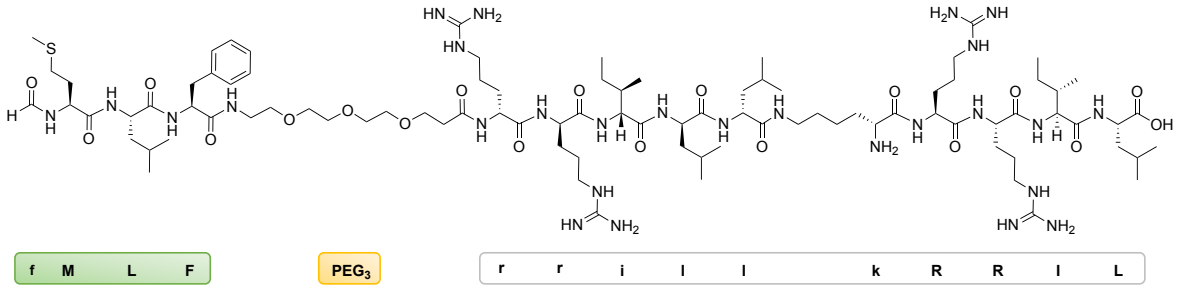

Figure 25 | Detailed structure of peptide 6. The D-Lys forms an isopeptide bond, and the fMLF-motif (green) is coupled *via* PEG_3 (yellow) to the *N*-terminus of D-Arg.

The assessment of the product purity was conducted via analytical HPLC (see **Figure 26**), revealing one single peak with minimal accompanying side peaks at the 214 nm trace. The small discrepancy also reflects in the mass spectrum with additional peaks in the lower m/z area. However, the mass pattern of $[M+2H]^{2+}$, $[M+3H]^{3+}$ and $[M+4H]^{4+}$ is consistent with the calculated mass of 1959.5 Da, thereby confirming the correct product.

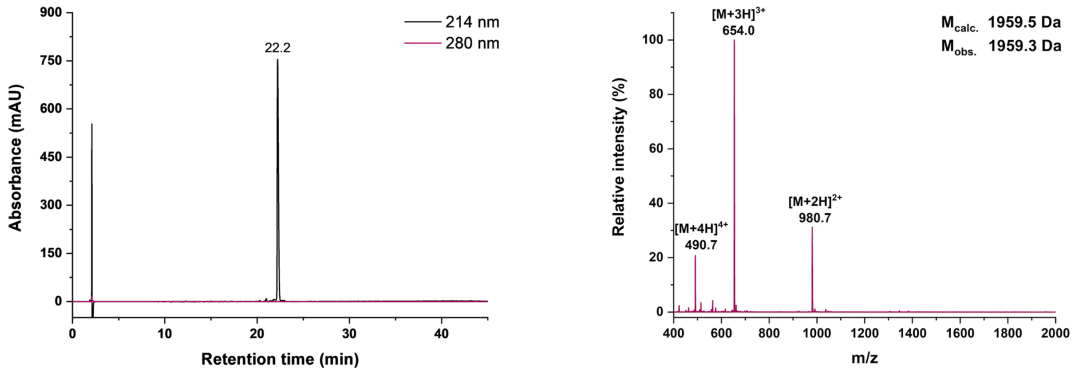

Figure 26 | Final analysis of peptide 6 with the sequence k*(fMLF-PEG_3-rrill)-RRIL. HPLC chromatogram (left) and ESI-MS spectrum (right).

The silica particles generated with peptide **6** were anticipated to exhibit spherical morphology, consistent with both their scaffold peptide **2** and the modification with the *N*-formyl peptide. As illustrated in **Figure 27**, that expectation was fulfilled and particles with a

diameter between 720–910 nm were observed. Similar to the previous description, the particles cluster together and some exhibit fusion.

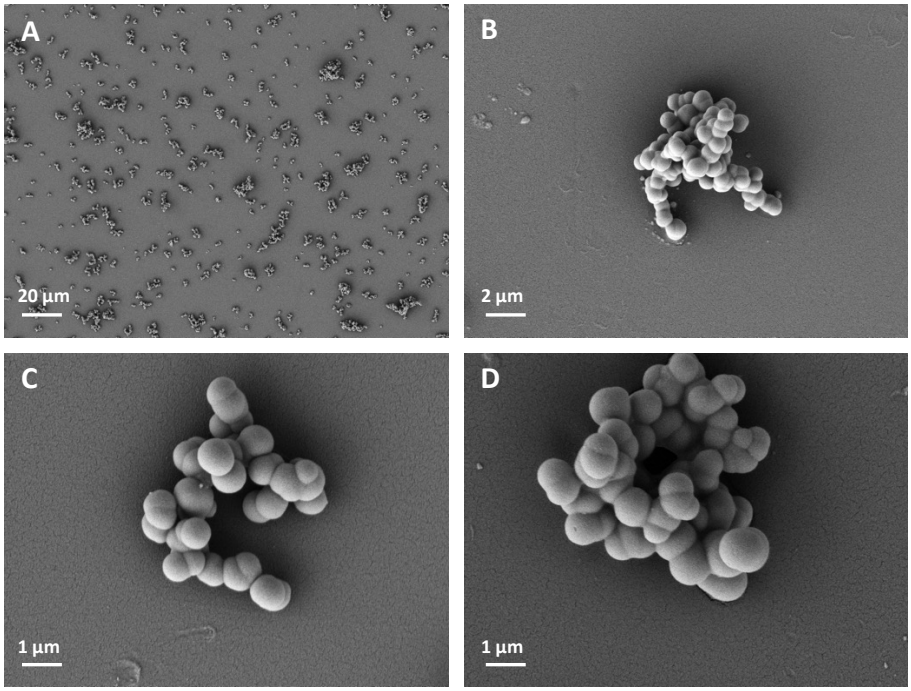

Figure 27 | SEM results of particles derived from peptide 6 with the sequence k*(fMLF-PEG$_3$-rrill)-RRIL. The produced particles display a spherical morphology.

4.1.7 **Peptide 7**

Upon observing spherical-shaped particles produced by all modified peptides, the impact of the chemical nature of modification on the morphology of the particles was investigated. Due to the inherent tendency of the k*(rrill)-RRIL scaffold peptide to form spherical particles, the focus was set on the K*(rrill)-RRIL scaffold peptide, exclusively, since that rod-shaped morphology is not formed commonly. Commencing with the modification of the smallest amino acid, a glycine residue was introduced at the *N*-terminus of the L-Lys to generate peptide **7** (see **Figure 28**). Moreover, the introduction of glycine reveals a free amino group, in contrast to *N*-formyl peptide modificatinos.

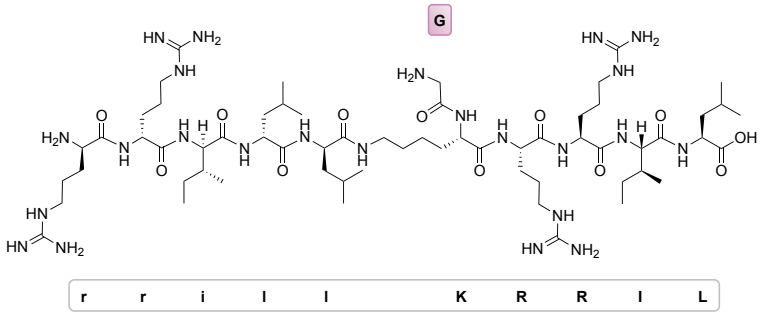

Figure 28 | Detailed structure of peptide 7. The L-Lys forms an isopeptide bond and the Gly-residue (magenta) is coupled to its *N*-terminus.

The synthesis route including automated synthesizer and manual coupling of glycine, outlined in **Figure 8**, was conducted at a scale of 0.04 mmol, yielding 26.7 mg (47.8% theoretical yield).

The purity evaluation via analytical HPLC revealed a single peak at the 214 nm trace and the confirmation of the correct product is reflected in the mass pattern of $[M+H]^+$, $[M+2H]^{2+}$ and $[M+3H]^{3+}$ is consistent with the calculated mass of 1393.8 Da (see **Figure 29**).

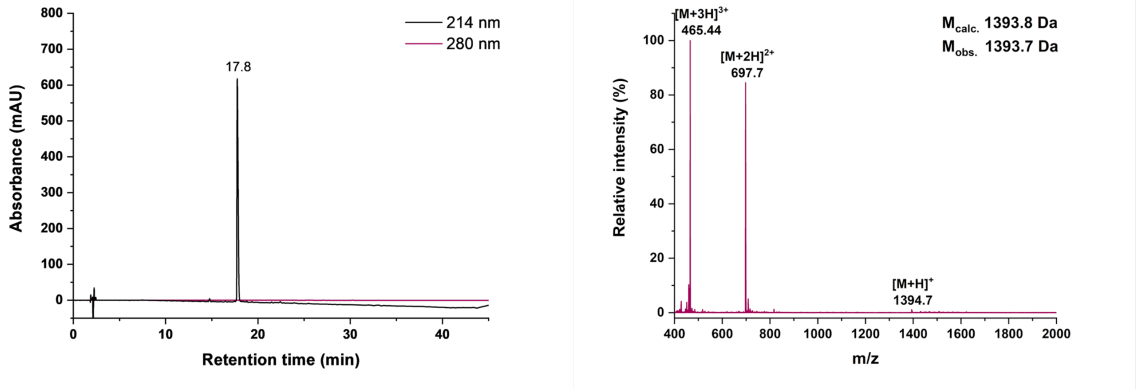

Figure 29 | Final analysis of peptide 7 with the sequence GK*(rrill)-RRIL. HPLC chromatogram (left) and ESI-MS spectrum (right).

The silica particles produced by the peptide **7** present an intriguing appearance, displaying both rod-shaped particles measuring approximately 1.91 µm in length and 0.15 µm in diameter and spherical particles with a non-uniform diameter around 470 nm (see **Figure 30**). Once again, both types of particles tend to cluster, with rod-shaped particles aligning with others of the same shape, and spherical particles grouping together. The different

morphologies were also found to be fused together (see **Figure 30A and D**). The observation suggests even small alterations have an impact on the silica morphology.

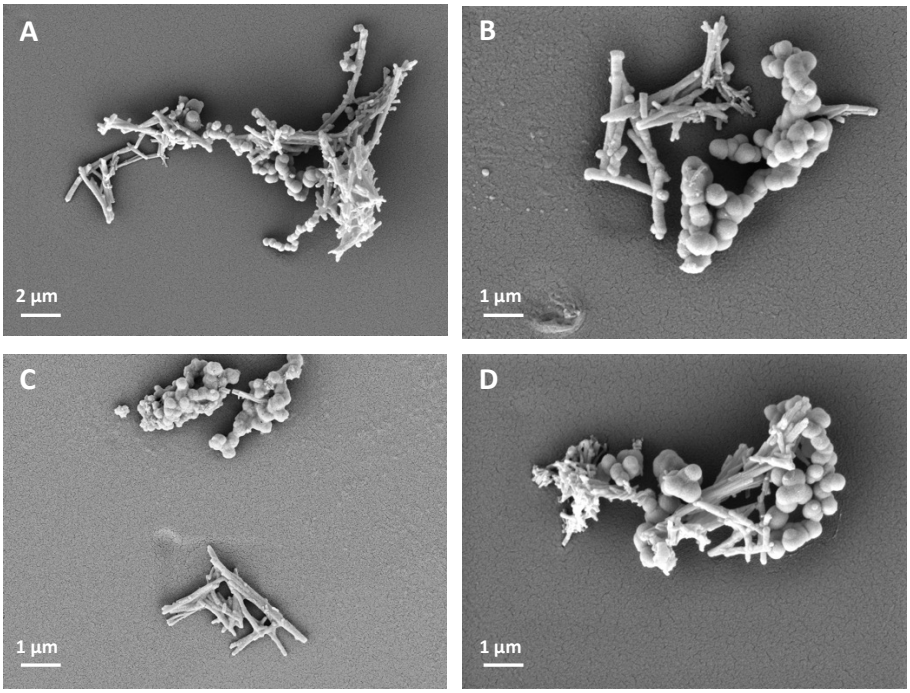

Figure 30 | SEM results of particles derived from peptide 7 with the sequence GK*(rrill)-RRIL. The produced particles display a mixture of spherical and rod-shaped morphology.

4.1.8 **Peptide 8**

The peptide **8**, a regioisomer of peptide **7,** was synthesized to investigate the changes in silica particle morphology resulting from slightly modified variants of K*(rrill)-RRIL. The synthesis of the peptide (see **Figure 31**), followed the route illustrated in **Figure 9** at a scale of 0.04 mmol. The yield obtained was 32.9 mg, corresponding to a theoretical yield of 59.0%.

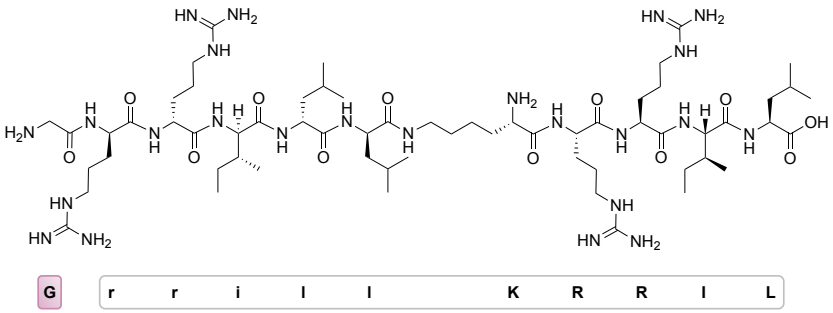

Figure 31 | Detailed structure of peptide 8. The L-Lys introduces forms an isopeptide, and the Gly-residue (magenta) is coupled to the *N*-terminus of D-Arg.

The peptide was subjected to analysis via analytical HPLC, revealing one single peak at the 214 nm trace, which indicates high purity. Moreover, the mass spectrum illustrates the pattern of $[M+H]^+$, $[M+2H]^{2+}$ and $[M+3H]^{3+}$, which is consistent with the calculated mass of 1393.8 Da (see **Figure 32**).

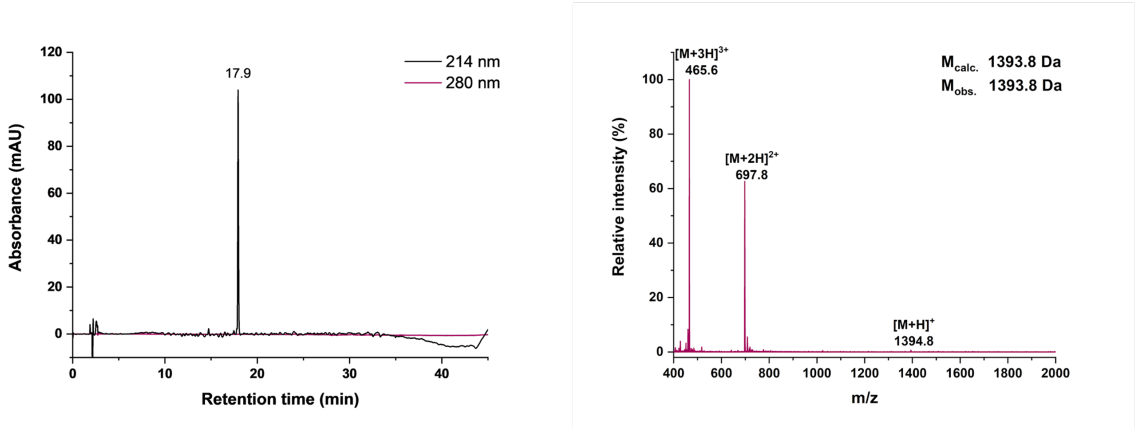

Figure 32 | Final analysis of peptide 8 with the sequence K*(Grrill)-RRIL. HPLC chromatogram (left) and ESI-MS spectrum (right).

The particles depicted in **Figure 33** were generated using peptide **8**, displaying a rod-shaped morphology with a rough surface. In contrast to its regioisomer, that was the only observed manifestation. This suggests that the presence of glycine on the *N*-terminus of D-Arg has no influential effect on peptide assembly, and thus, it serves as a template for rod-shaped particles. The rods measure approximately 6.26 µm in length and 0.22 µm in diameter, roughly three-times the length but not such a significant difference in diameter compared to rod-shaped particles produced with peptide **7**.

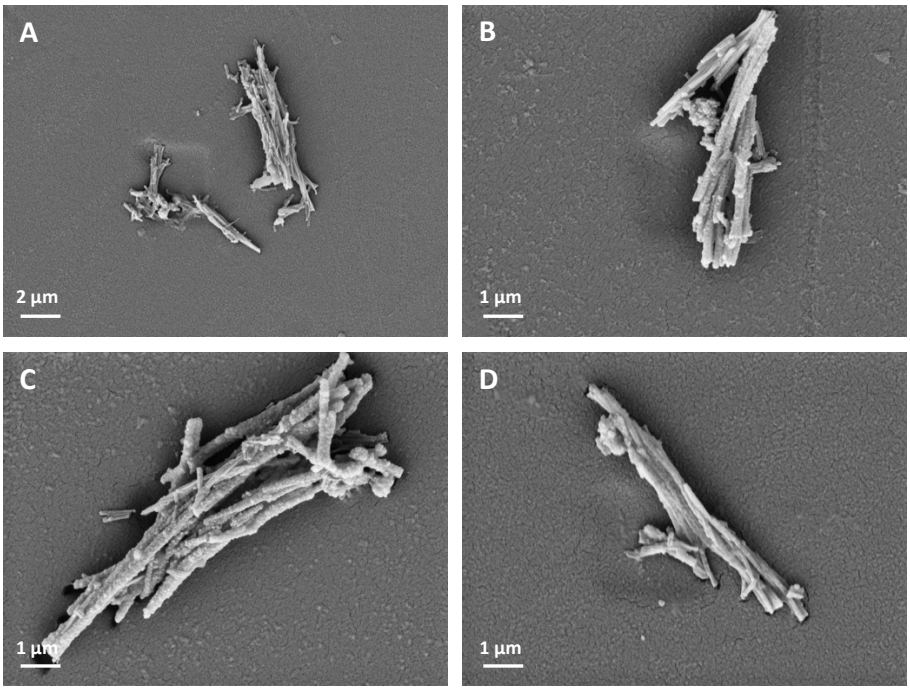

Figure 33 | SEM results of particles derived from peptide 8 with the sequence K*(Grrill)-RRIL. The produced particles display a rod-shaped morphology.

4.1.9 Peptide 9

Due to previous findings that the modification of glycine to D-Arg results in rod-shaped particles, an alternative structure introducing the *N*-formyl peptide fMLF, while retaining free amine groups at both *N*-termini was synthesized (see **Figure 34**) following the route outlined in **Figure 9**. The Boc-D-Dab(Fmoc)-OH was utilized to introduce the second isopeptide bond. The synthesis was executed at a scale of 0.04 mmol, yielding 25.9 mg, which corresponds to a theoretical yield of 31.5%.

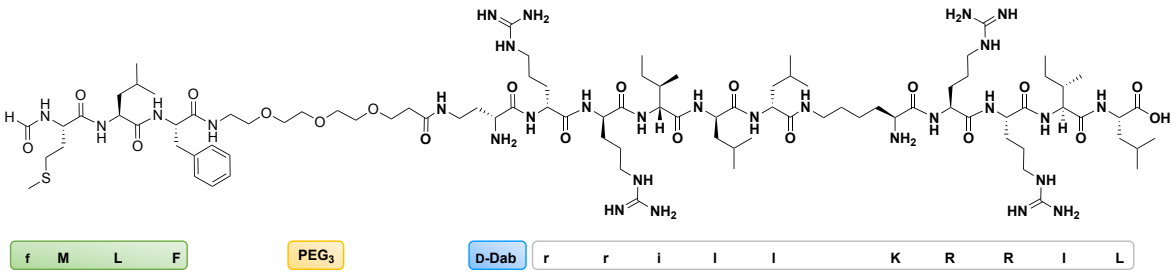

Figure 34 | Detailed structure of peptide 9. The L-Lys forms an isopeptide bond and the following amino acids are coupled to the ε-amino group, ending in D-Dab (blue), which introduces a second isopeptide bond to couple the fMLF-motif (green) *via* PEG_3 (yellow).

Analytical HPLC was employed to assess the purity of the product, revealing a single peak at the 214 nm trace, exceeding 95% purity (see **Figure 35**).

The mass spectrum confirmed the correct product, presenting the accurate mass pattern accompanied by minor peaks in the lower m/z area pointing to small impurities, yet still aligning with calculated mass 2059.7 Da.

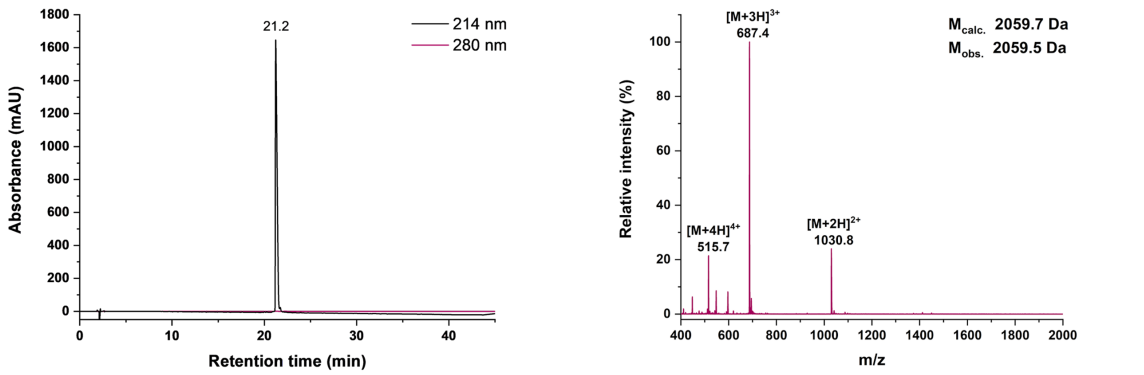

Figure 35 | Final analysis of peptide 9 with the sequence K*(D-Dab*(fMLF-PEG$_3$)-rrill)-RRIL. HPLC chromatogram (left) and ESI-MS spectrum (right).

The particles produced from peptide **9** are characterized by spherical particles with a diameter of ranging from 610–820 nm (see **Figure 36**). That occurrence may be attributed to the large modification, incorporating the hydrophobic fMLF-motif and the PEG$_3$ linker, which potentially disturb self-assembly and favoring spherical morphology, as observed earlier in peptides **3–6**. Another possibility is that the larger D-Dab, in comparison to glycine, also influences the dense self-assembly, resulting in a spherical morphology.

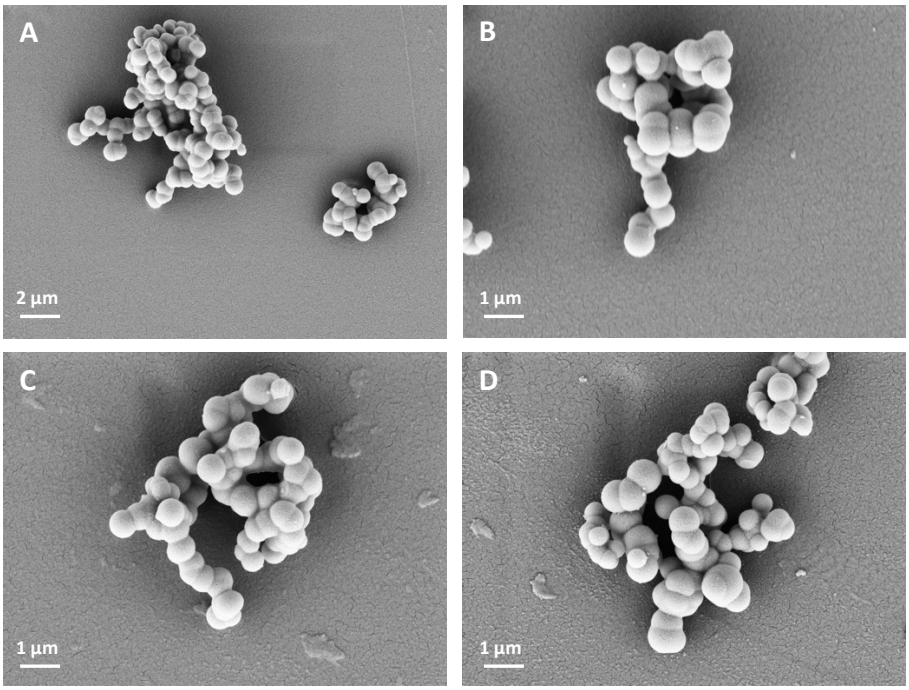

Figure 36 | SEM results of particles derived from peptide 9 with the sequence K*(D-Dab*(fMLF-PEG$_3$)-rrill)-RRIL. The produced particles display a spherical morphology.

4.1.10 Peptide 10

The particles derived from peptide **9** exhibit spherical morphology. To distinguish between the effect of fMLF and Dab alone the peptide **10** (see **Figure 37**) was synthesized as outlined in **Figure 9,** at a scale of 0.015 mmol, yielding 12.1 mg (56.2% theoretical yield).

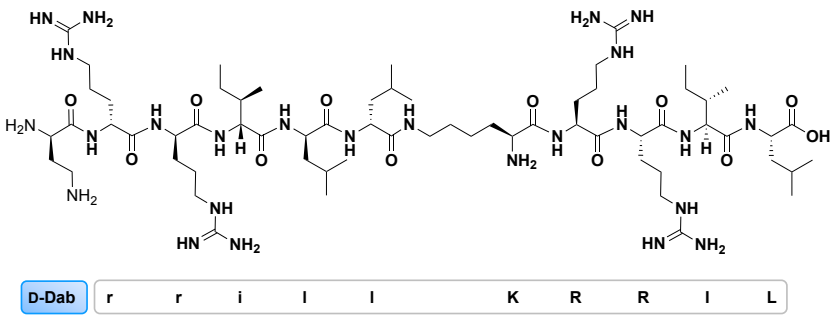

Figure 37 | Detailed structure of peptide 10. The L-Lys forms an isopeptide bond and the following amino acids are coupled to the ε-amino group, ending in D-Dab (blue).

Purity assessment via analytical HPLC exposes a very sharp single peak at the 214 nm trace, indicating very high purity (see **Figure 38**).

The mass spectrum confirmed the correct product, displaying the precise mass pattern accompanied by minor peaks in the lower m/z area pointing to small impurities or fragmentation of the peptide, yet still aligning with calculated mass 1436.9 Da.

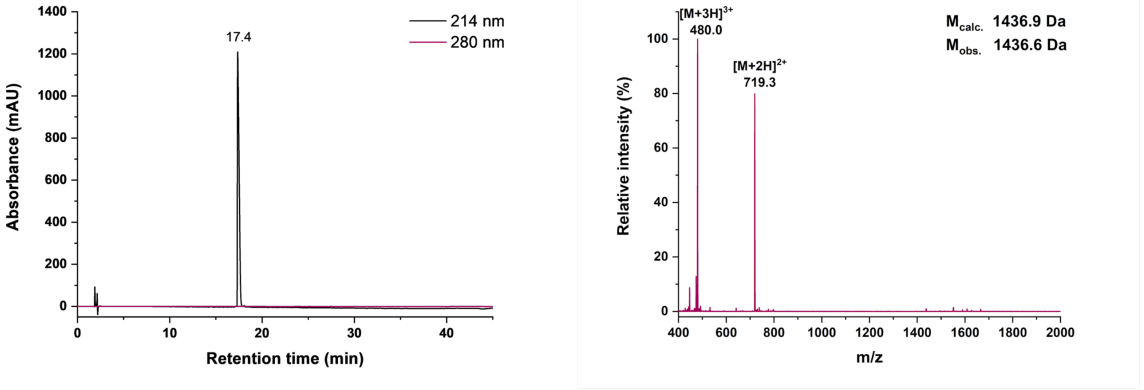

Figure 38 | Final analysis of peptide 10 with the sequence K*(D-Dab-rrill)-RRIL. HPLC chromatogram (left) and ESI-MS spectrum (right).

The particles derived from peptide **10** exhibit a rod-shaped morphology with highly variable lengths, reaching up to 11.42 µm. However, they maintain a consistent diameter of approximately 0.16 µm, similar to the other rod-shaped particles derived from peptides **1** and **8**. But in contrast to the stick-like particles originating from the scaffold peptide **1** they emanate from the center and radiate outward (see **Figure 39**). Additionally, they readily form aggregates, as illustrated in **Figure 39D** and appear twisted rather than lineal as in particles produced with peptide **1** and **8**.

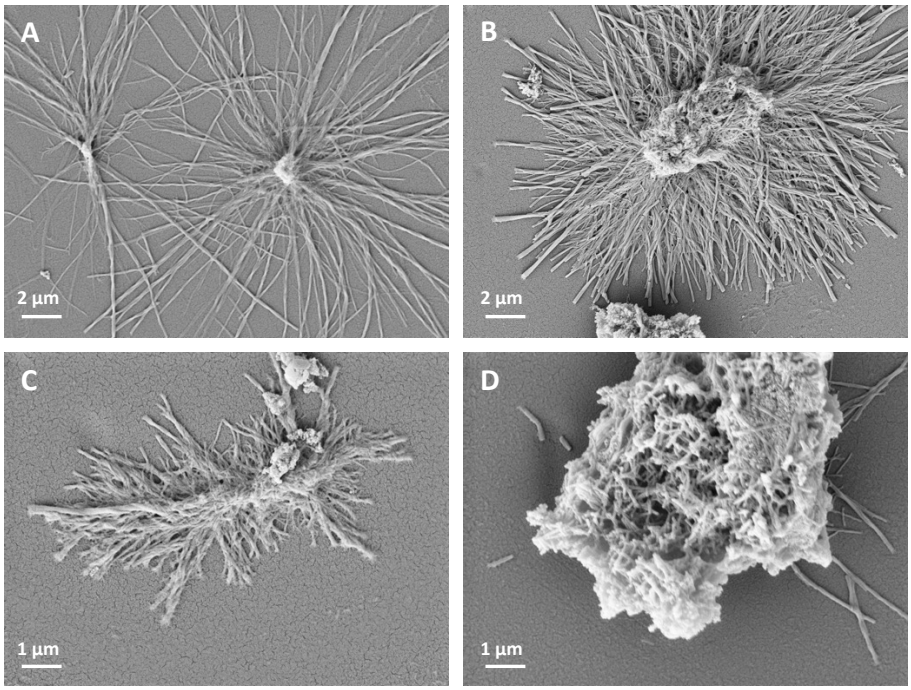

Figure 39 | SEM results of particles derived from peptide 10 with the sequence K*(D-Dab-rrill)-RRIL. The produced particles display long rod-shaped morphology radiating from the center.

4.1.11 Peptide 11

Upon observing that elongation at the *N*-terminus of D-Arg is tolerated, evidenced by the rod-shaped morphology in the resulting particles of peptide **8** and **10**, the subsequent investigation focused on the impact of the linker PEG_3 on the manifestation of the particles. Therefore, the peptide **11** (see **Figure 40**) was synthesized following the pathway illustrated in **Figure 9,** at a scale of 0.015 mmol, yielding 12.2 mg (52.8% theoretical yield).

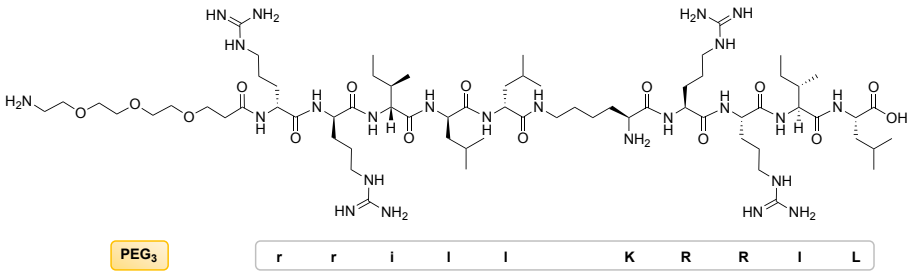

Figure 40 | Detailed structure of peptide 11. The L-Lys forms an isopeptide bond and the following amino acids are coupled to the ε-amino group ending with a PEG_3 (yellow) modification.

Analytical HPLC was utilized to evaluate the purity of the product, and the presence of a singular peak, accompanied by a minor side peak at the 214 nm trace affirmed a high purity level exceeding 95% (see **Figure 41**).

The mass spectrum further verified the correctness of the product, by the mass pattern $[M+2H]^{2+}$ and $[M+3H]^{3+}$, aligning with the calculated mass of 1540.0 Da.

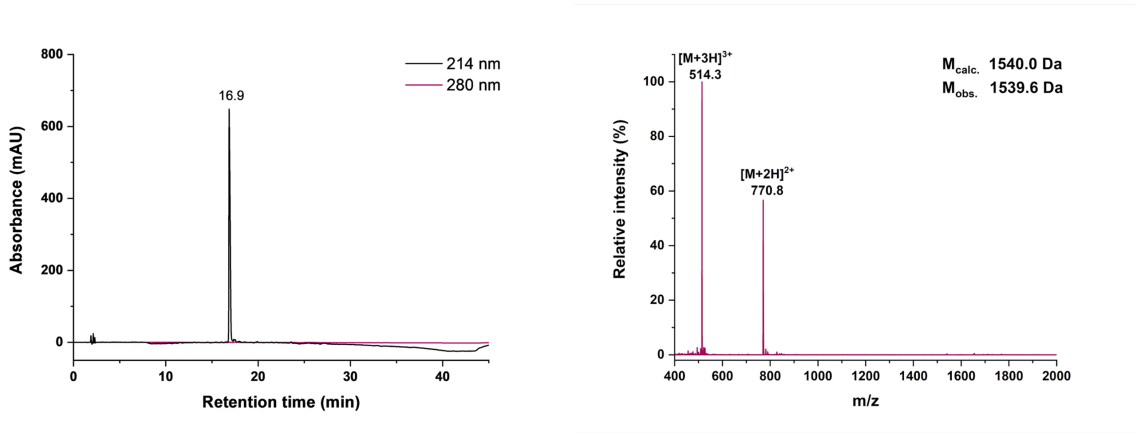

Figure 41 | Final analysis of peptide 11 with the sequence K*(PEG$_3$-rrIll)-RRIL. HPLC chromatogram (left) and ESI-MS spectrum (right).

The particles originating from peptide **11** exhibit spherical morphology with a not uniformly distributed diameter of 520–740 nm as illustrated in **Figure 42**. This might be attributed to the hydrophilicity and flexibility of the PEG_3 linker, which could potentially shield the positively charged arginine residues, the main contributors to the self-assembly.

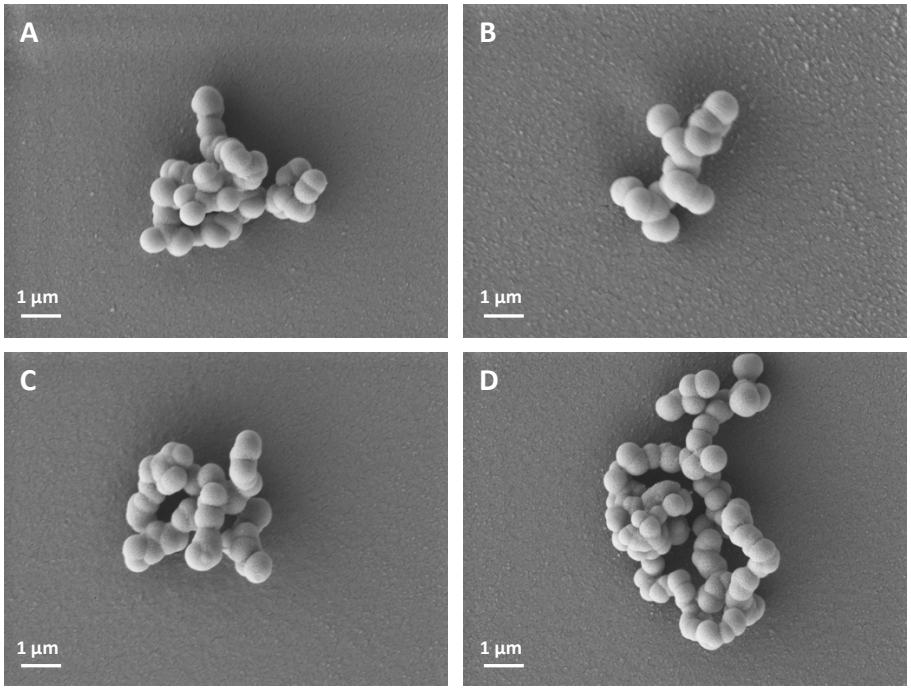

Figure 42 | SEM results of particles derived from peptide 11 with the sequence K*(PEG$_3$-rrIll)-RRIL. The produced particles display a spherical morphology.

4.1.12 Peptide 12

After the observation that the PEG_3 group encourages the formation of spherical particles, the impact of the *N*-formyl peptide motif fMLF was also investigated. The synthesis of peptide **12** (see **Figure 43**) was carried out following the pathway in **Figure 9** at a scale of 0.015 mmol, with a yield of 13.3 mg, adding up to a theoretical yield of 50.4%.

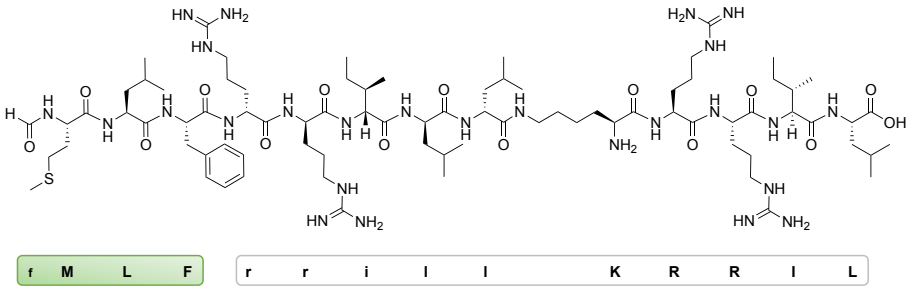

Figure 43 | Detailed structure of peptide 12. The L-Lys forms an isopeptide bond and the following amino acids are coupled to the ε-amino group ending with a fMLF (green) modification.

The final analysis encompassed both analytical HPLC and ESI-MS (see **Figure 44**). The chromatogram displays a distinct and sharp peak, indicative of a pure product. Additionally, the mass spectrum demonstrates a very clear mass pattern with $[M+2H]^{2+}$, $[M+3H]^{3+}$ and $[M+4H]^{4+}$, corresponding to the calculated mass of 1756.3 Da.

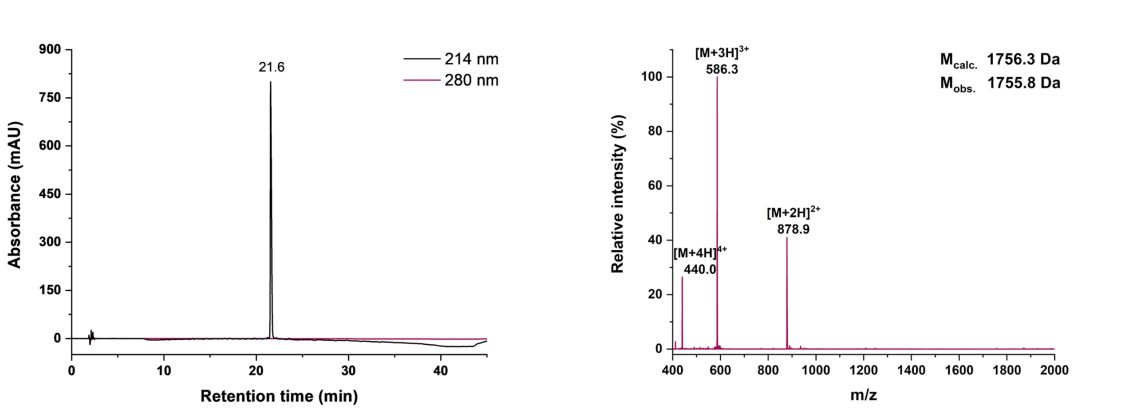

Figure 44 | Final analysis of peptide 12 with the sequence K*(fMLF-rrill)-RRIL. HPLC chromatogram (left) and ESI-MS spectrum (right).

The particles derived from peptide **12** exhibit a pronounced different morphology, lacking distinct manifestation (see **Figure 45**). They appear cloud-like with possibly very small spheres aggregated into clusters. Notably, **Figure 45D** reveals the presence of a stick-like morphology. The reasoning is very hard to point out, although it is noteworthy that the

modification with fMLF shifts the hydrophobicity of the entire peptide to more hydrophobic properties. Moreover, the charge of the *N*-terminus is lost, which could also possibly influence the self-assembly.

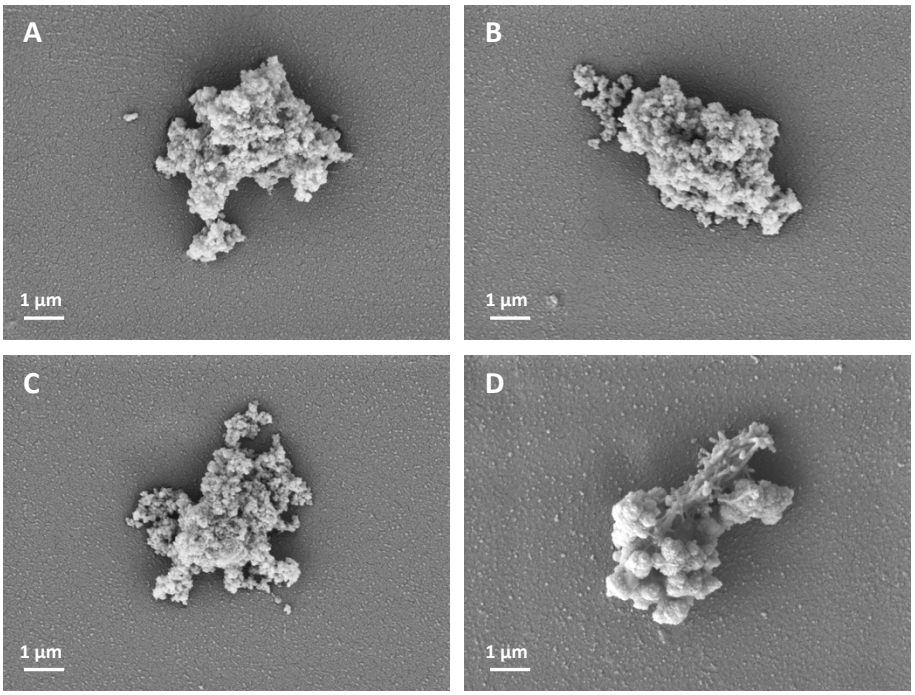

Figure 45 | SEM results of particles derived from peptide 12 with the sequence K*(fMLF-rrill)-RRIL. The produced particles do not display a distinct morphology. (A)–(C) shows cloud-like aggregates with seeminly very small spheres. In (D) additionally stick-like morphology is recognizable.

4.1.13 Peptide 13

The formation of particles derived from peptide **12** exhibited unexpected and indistinct characteristics, prompting the synthesis of peptide **13** (see **Figure 46**). The aim was to elucidate the impact of the formylation on the particle formation.

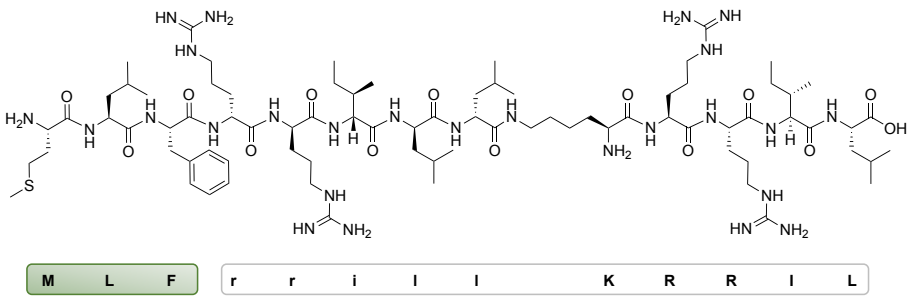

Figure 46 | Detailed structure of peptide 13. The L-Lys forms an isopeptide bond and the following amino acids are coupled to the ε-amino group ending with a MLF (dark green) modification.

The peptide was synthesized according to **Figure 9**, at a scale of 0.015 mmol. The yield added up to 16.1 mg and a theoretical yield of 62.3%.

The evaluation of the purity of the product was performed on analytical HPLC, which showed a sharp peak (see **Figure 47**) pointing to high purity.

The calculated mass of 1728.3 Da was perfectly reflected in the mass pattern $[M+2H]^{2+}$, $[M+3H]^{3+}$ and $[M+4H]^{4+}$.

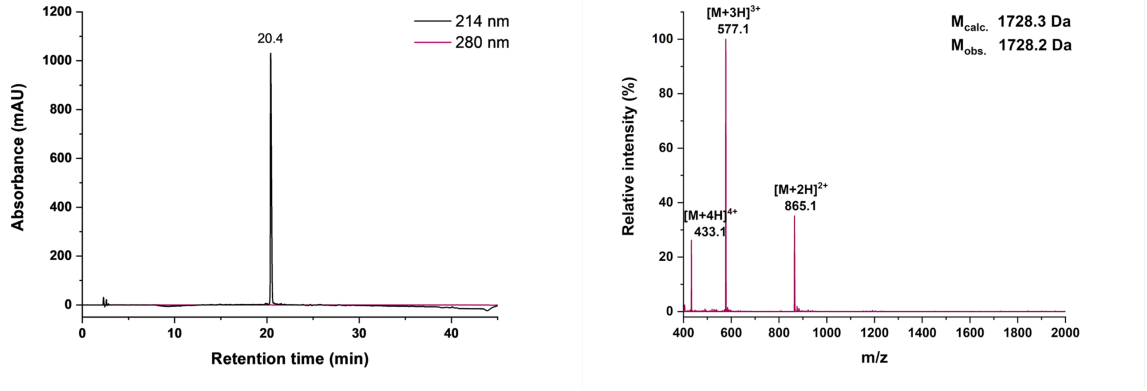

Figure 47 | Final analysis of peptide 13 with the sequence K*(MLF-rrill)-RRIL. HPLC chromatogram (left) and ESI-MS spectrum (right).

The particles derived from peptide **13** exhibit a spherical morphology with an uneven distributed diameter of 510–630 nm, as illustrated in **Figure 48**. As all the other particles they cluster together. The comparison between peptide **12** and **13** suggests, that even minor modifications, such as formylation, have a notable impact on the shape of the particles. Crucially, in this case, the *N*-terminus remained charged, indicating its crucial role in the self-assembly, that serves as a template for the silica particles.

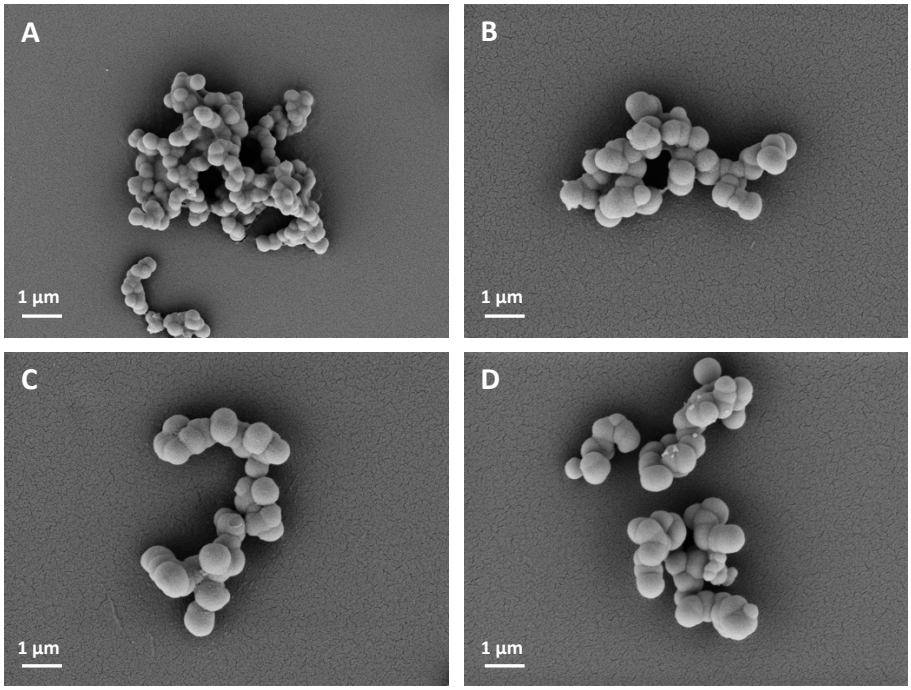

Figure 48 | SEM results of particles derived from peptide 13 with the sequence K*(MLF-rrill)-RRIL. The produced particles display an spherical morphology.

4.1.14 Peptide 14

The peptide **14** incorporated a Cy5 fluorescence tag to facilitate the tracking of particle uptake in following cellular experiments (not included in this thesis).

The Cy5 was synthesized in-house and the structure is depicted in **Figure 49**.[88] The scaffold peptide **2** was synthesized and the Cy5 was coupled manually, as outlined in **Figure 9**.

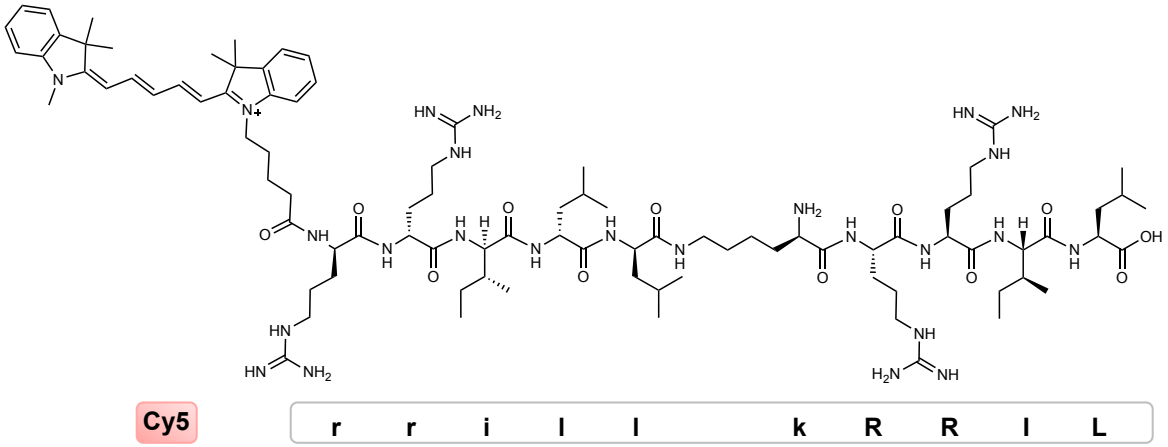

Figure 49 | Detailed structure of peptide 14. The D-Lys forms an isopeptide bond and the following amino acids are coupled to the ε-amino group ending with a Cy5 (red) modification.

The selection of the scaffold peptide **2** was based on its known manifestation of spherical particles, allowing its combination with fMLF modified peptides, which all exhibit spherical morphology.

The synthesis was conducted at a scale of 0.02 mmol, yielded 11.4 mg product (32.0% theoretical yield). Due to limited Cy5 availability, only 10 mg (1.1 equivalents) were used, likely reducing the overall yield.
Analytical HPLC was utilized to evaluate the purity of the product, and the presence of a singular peak, accompanied by a minor side peak affirmed a high purity (see **Figure 50**).
The mass spectrum further verified the product, by the mass pattern $[M+2H]^{2+}$, $[M+3H]^{3+}$ and $[M+4H]^{4+}$aligning with the calculated mass of 1788.4 Da.

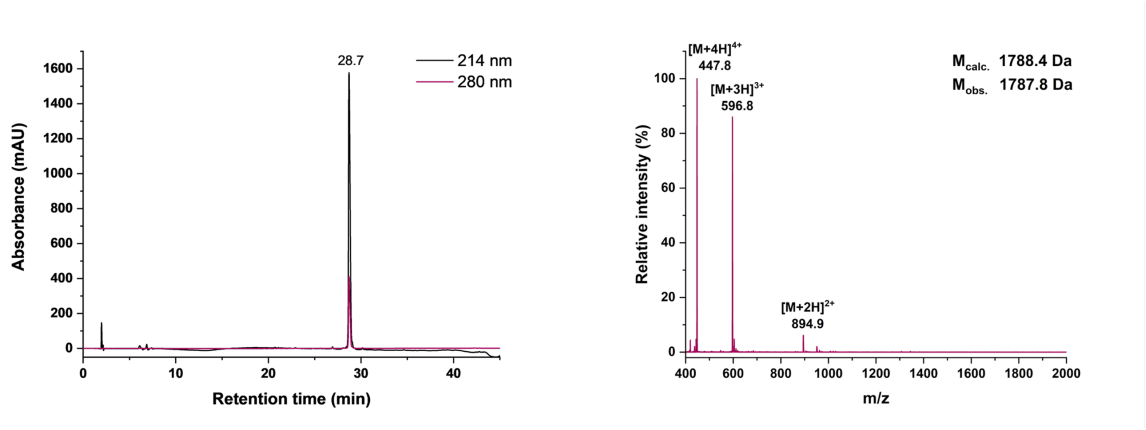

Figure 50 | Final analysis of peptide 14 with the sequence k*(Cy$_5$-rrill)-RRIL. HPLC chromatogram (left) and ESI-MS spectrum (right).

The particles derived from peptide **14** show spherical morphology, with little spheres on top, which are illustrated in **Figure 51 A** and **B**. The larger spheres have a diameter of 630–820 nm, while the smaller spheres measure 210–270 nm. For the particles depicted in **Figure 51C** and **D** 99% peptide **3** and 1% peptide **14** were used for silica precipitation, resulting in spherical particles with without smaller spheres on top and same diameters as determined for peptide **3** alone. That allows the tracking of the particles in cell compartments.

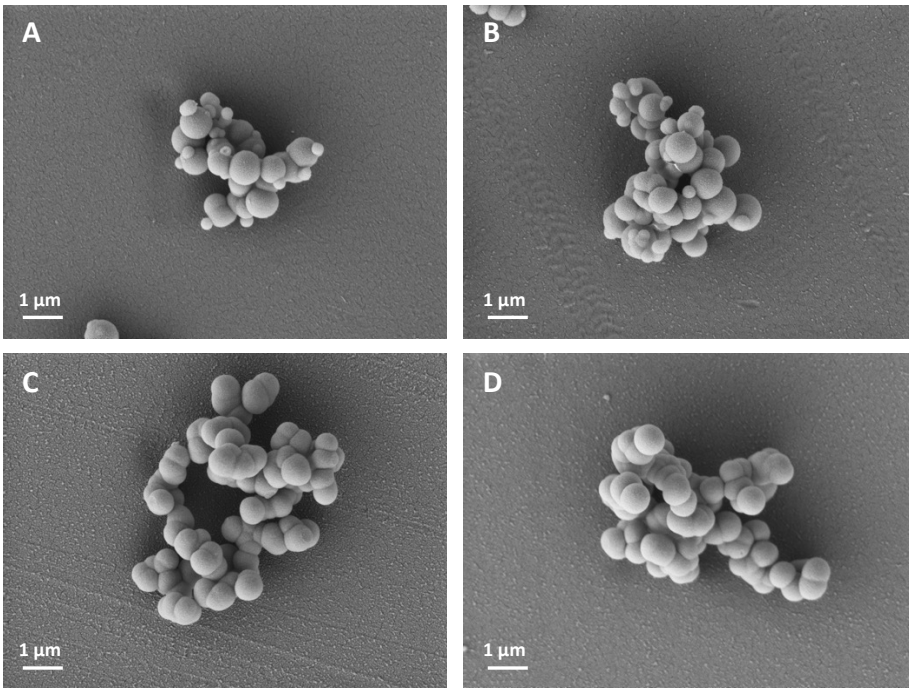

Figure 51 | SEM results of particles derived from peptide 14 with the sequence k*(Cy$_5$-rrill)-RRIL. (A)(B) Particles derived from peptide 14 show spherical morphology with little spheres on top. (C)(D) Particles derived from 99% peptide 3 and 1% peptide 14 only showed spherical morphology.

4.1.15 Discussion of results for silica-precipitating peptides 1-14

For all peptides the solid-phase peptide synthesis proceeded smoothly. However, after automated synthesis the resin had to be transferred to a syringe for manual coupling of modifications such as fMLF-PEG$_3$, Gly, D-Dab and more, which led to product loss. Additionally, since the same scaffold peptides were used for different following peptide modifications, the division of the resin was sometimes necessary after automated synthesis. As a result, the scale could only be estimated by weighing the dry resin portions and calculate the portion of the initial scale. It is important to consider this, while interpreting the stated yields.

For most of the peptides a good yield of over 50% of the theoretical yield could be obtained. However, peptides **4**, **5**, **7**, **9** and **14** exhibit yields below 50%. For peptide **4**, the omission of double couplings for the amino acids of fMLF likely resulted in deletions, observable in the MS-spectrum of side products. Subsequent synthesis involved double couplings for the fMLF motif. Peptides **5** and **7** were modified at the *N*-terminus of lysine, requiring re-introduction to the automated synthesizer, which possibly lead to smaller yields. Interestingly, peptide **3**, subjected to the same process, had a good yield of 62%. Peptide **9** with D-Dab includes a second isopeptide bond and is also the longest one. Its comparatively

small yield may be attributed to potential incomplete condensation reactions and the presence of byproducts.

The synthesis of peptide **14** was limited by availability of Cy5 (1.1 equivalents relative to the synthesis scale).

The peptide yields are listed in **Table 6**. All peptides were obtained at very high purity of >95%, with some additional pooled fractions also exceeding 90% purity.

Table 6 | Summary of yields of all synthesized peptides. The synthesis scale could only be estimated due to the transfer and splitting of the resin after automated synthesis. The yield includes all peptides that exceed a purity of 90% and refers to the theoretical yield from the synthesis scale.

Primary sequence	Peptide #	M_w / g·mol^{-1}	Synthesis scale / mmol	Yield / mg	Yield / %
K*(rrill)-RRIL	**1**	1336.8	0.015	14.1	**70.5**
k*(rrill)-RRIL	**2**	1336.8	0.020	16.7	**62.5**
fMLF-PEG_3-K*(rrill)-RRIL	**3**	1959.5	0.045	55.0	**62.4**
K*(fMLF-PEG_3-rrill)-RRIL	**4**	1959.5	0.045	23.4	**26.6**
fMLF-PEG_3-k*(rrill)-RRIL	**5**	1959.5	0.045	11.5	**13.1**
k*(fMLF-PEG_3-rrill)-RRIL	**6**	1959.5	0.035	44.6	**65.0**
GK*(rrill)-RRIL	**7**	1393.8	0.040	26.7	**47.8**
K*(Grrill)-RRIL	**8**	1393.8	0.040	32.9	**59.0**
K*(D-Dab*(fMLF-PEG_3)-rrill)-RRIL	**9**	2059.7	0.040	25.9	**31.5**
K*(D-Dab-rrill)-RRIL	**10**	1436.9	0.015	12.1	**56.2**
K*(PEG_3-rrill)-RRIL	**11**	1540.0	0.015	12.2	**52.8**
K*(fMLF-rrill)-RRIL	**12**	1756.3	0.015	13.3	**50.4**
K*(MLF-rrill)-RRIL	**13**	1728.3	0.015	16.1	**62.3**
k*(Cy5-rrill)-RRIL	**14**	1788.4	0.020	11.4	**32.0**

Following synthesis, the silica-precipitating properties of the peptides were analyzed. All of the modified peptides induced the formation of silica particles upon incubation in phosphate

buffer and addition of silicic acid. The resulting particles exhibited predominantly spherical morphology, some a rod-shaped one with the only exception of peptide **12**, characterized by the sequence K*(fMLF-rrill)-RRIL. The particles generated with peptide **12** formed were cotton-like with seemingly very small spheres but lacked a distinct morphology compared to the others.

As previously described the peptides were based on the scaffold peptide **1** with the sequence K*(rrill)-RRIL and peptide **2**, characterized by k*(rrill)-RRIL, which form rod-shaped and spherical particles. The rod-shaped particles generated by peptide **1** could be attributed to the compact self-assembly, due to electrostatic interactions between the positively charged arginine and the phosphate ions in solution and more hydrophobic interactions. The compact peptides form aggregates that serve as a template for the rod-shaped particles. In contrast, peptide **2** forms less dense self-assemblies and lacks hydrophobic interactions, which leads to manifestation of spherical particles.[1]

The peptides **3–5** incorporate the *N*-formyl peptide fMLF, linked *via* a PEG_3 chain to the *N*-terminus of either D-Arg or L-Lys or D-Lys. All these peptides induced silica precipitation and yielded spherical particles (see **Figure 52**). That could be attributed to the large modification involving the flexible, hydrophilic PEG_3 chain and also the hydrophobic fMLF. That modification could shield some of the positive charges from arginine, leading to less dense compaction of the peptide and therefore templating of spherical particles. Moreover, the modification causes the loss of charge on one *N*-terminus, potentially reducing interactions. Since peptide **2** generates spherical particles, and the large modification seems to further reduce the compact self-assembly, it was assumed that further modification would not lead to rod-shaped particles. Therefore subsequent modifications were based on peptide **1**, to determine which modifications would still enable the formation of rod-shaped particles.

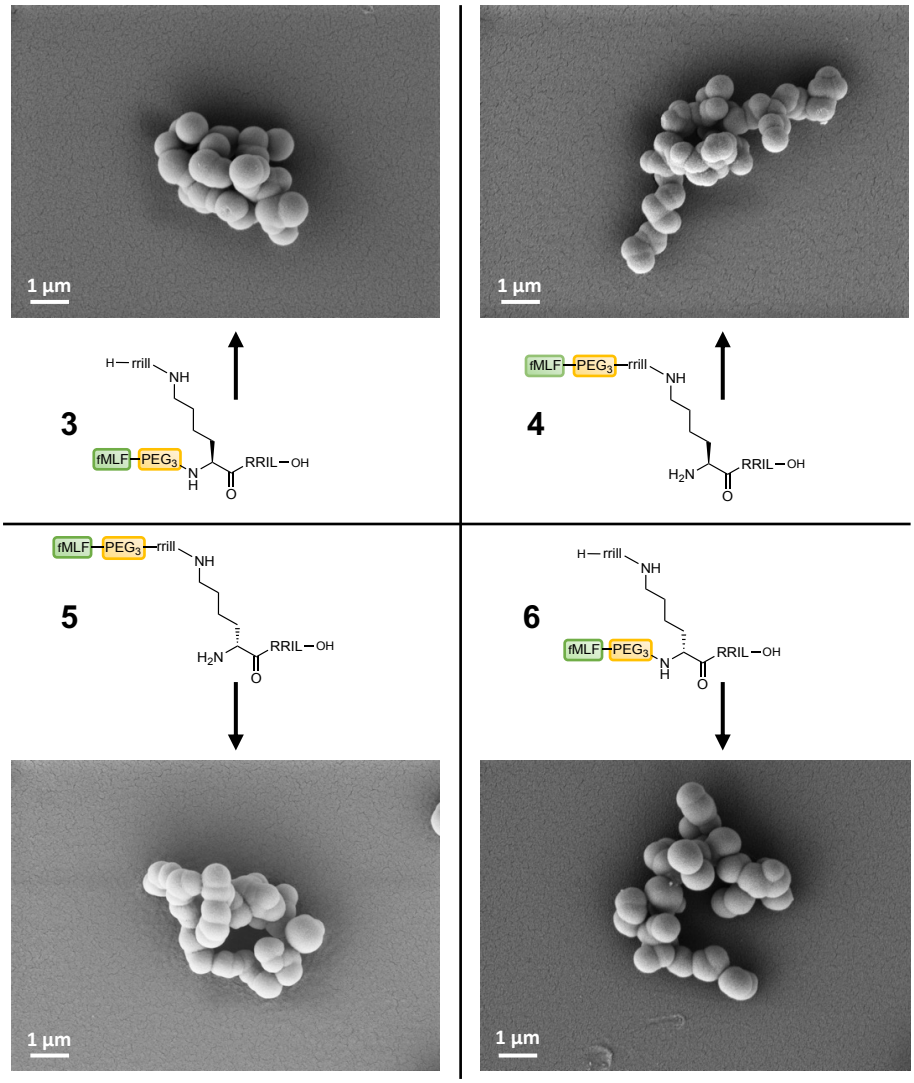

Figure 52 | Comparison of particles generated with fMLF-PEG$_3$ modified peptides 3–6. The structure of the peptides as well as the corresponding particles are depicted. All particles exhibit spherical morphology.

To distinguish the impact of a modification on the *N*-termini a glycine modification was added to each amino group. While the modification on the D-Arg, which maintains the linear peptide is less pronounced, the modification on the L-Lys, introducing a branch, proved to be intriguing (see **Figure 53**). Evidently, with peptide **7**, two states evolve, that represent a shift from one form of assembly to another, leading to the formation of two different particle morphologies. In contrast, peptide **8** exclusively promoted the manifestation of rod-shaped particles. That shows that the scaffold peptide **1** could be elongated and still produce rod-shaped particles. Furthermore, it emphasizes that the position of the modification plays a significant role.

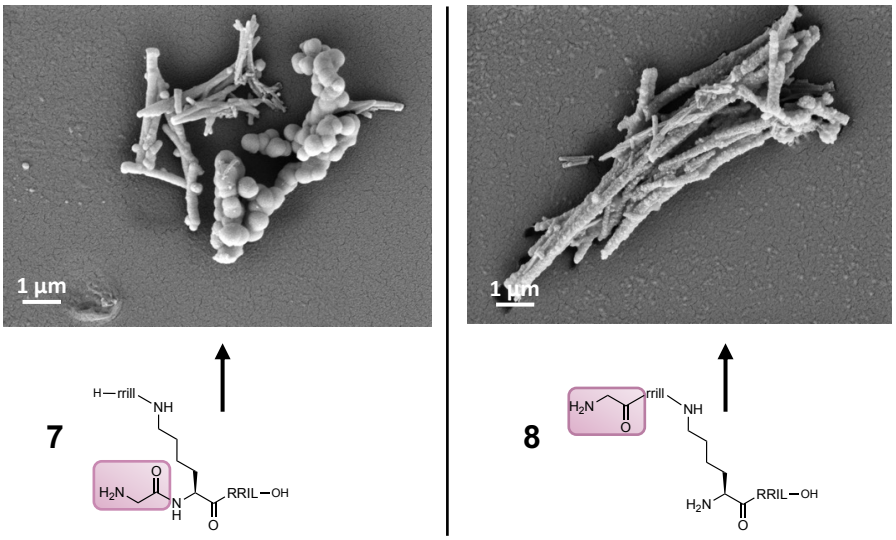

Figure 53 | Comparison of particles generated with peptides 7 and 8 modified with glycine at one *N*-terminus. The structure of the peptides as well as the corresponding particles are depicted. Peptide **7** generated both spherical and rod-shaped particles, while peptide **8** exclusively produced rod-shaped particles.

Since the peptide **8** precipitated rod-shaped particles, the introduction of a second isopeptide bond to incorporate the fMLF-PEG_3 modification while still retaining two charged *N*-termini was hypothesized to result in the production of rod-shaped particles. However, the particles produced with peptide **9** exhibited spherical particles similar to the particles generated by peptide **4** (see **Figure 54**). This finding supports the notion that the large modification with fMLF-PEG_3 prevents dense assemblies and results in the formation of spherical particles. To assess the specific impact of D-Dab on self-assembly peptide **10** was synthesized, which yielded the formation of rod-shaped particles that readily aggregated. The omission of the fMLF-PEG_3 group reduces the steric bulk and is likely responsible for the different morphology. In comparison to peptide **1**, the rods formed by peptide **10** are longer and extend outward from a dense aggregated cluster (see **Figure 54**). With D-Dab introducing an additional charge, stronger electrostatic interactions could occur, facilitating the dense compact self-assembly required for rod-shaped particles.

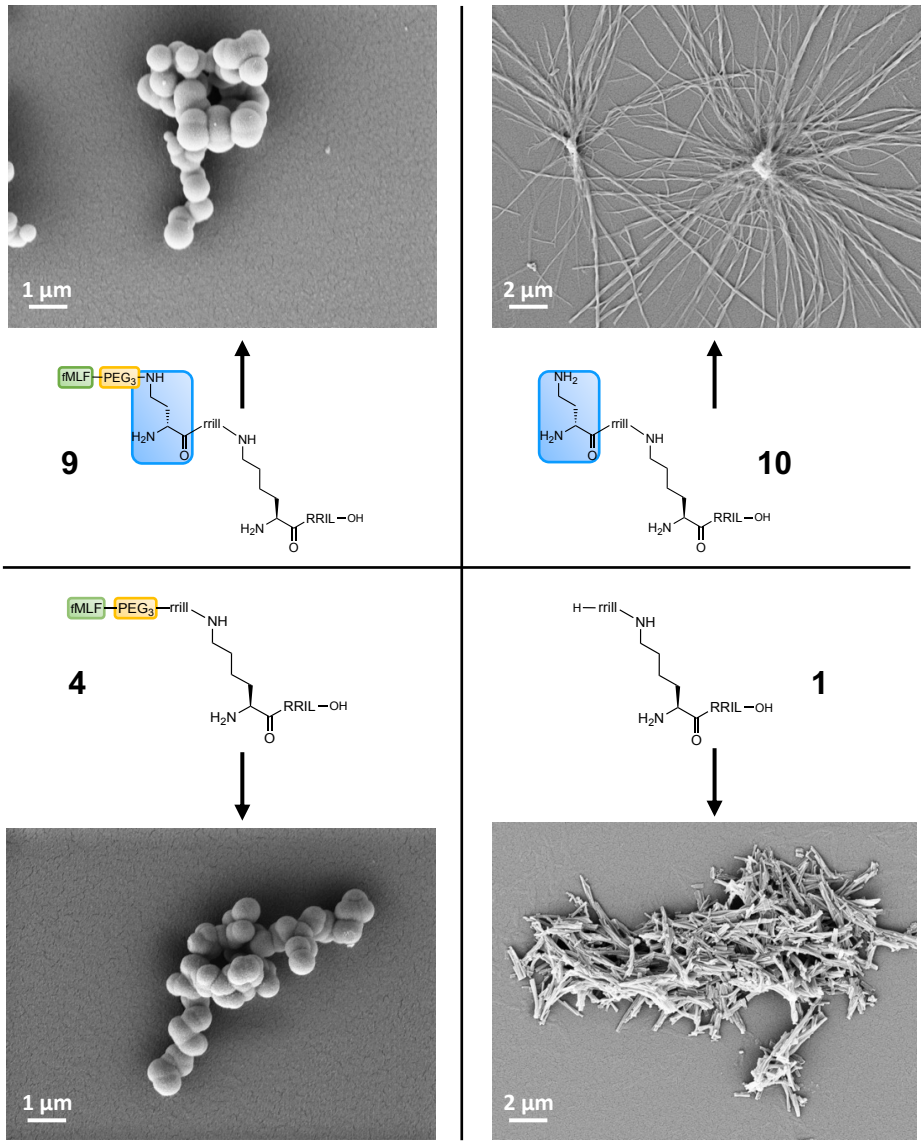

Figure 54 | Comparison of particles generated with peptides 9, 10, 4 and 1. The structure of the peptides as well as the corresponding particles are depicted. Peptide **9** forms spherical particles, similar to peptide **4**. Peptide **10** generates rod-shaped particles, but in comparison to peptide **1** they are longer and radiate outwards.

To evaluate the impact of the individual components of the fMLF-PEG_3 modification, namely the formyl group, the PEG linker and the hydrophobic MLF part, peptides **11–13** were synthesized**.** Peptide **11**, featuring the hydrophilic PEG_3 with a terminal amine, produced spherical particles. The flexibility of the linker could potentially disrupt the dense compaction in self-assembly required for rod-shaped assembly. The morphology of the particles produced with peptide **12**, modified with fMLF, was intriguing. The modification imparts higher hydrophobicity to the peptide while also reducing the charge due to formylation. In contrast, peptide **13**, lacking formylation, generated spherical particles again (see **Figure 55**). This is particularly interesting for several reasons: First, it suggests that the charge at the *N*-terminus plays a crucial role in assembly and templating. Although peptides **3–6** were

also formylated at one *N*-terminus, the flexible PEG_3 chain possibly impedes the effects of fMLF (e.g. shielding the positive charges required for self-assembly).

Furthermore, the comparison between peptide **13** and peptides **8** and **10** adds an interesting dimension to the analysis. Despite all three peptides being modified at D-Arg and maintaining a linear structure, peptides **8** and **10** act as templates for rod-shaped particles, whereas those produced with peptide **13** exhibit spherical morphology. This could be attributed to the larger modification imposed by MLF compared to Gly or D-Dab or also an increase in hydrophobicity. For peptide **1**, hydrophobic interactions play a crucial role in the formation of rod-shaped particles. However, it appears that this effect does not predominate the effect of the modification studied here. The MLF group potentially shields the positively charged groups from interaction with the phosphate ions in the buffer. Another factor to consider is that Phe might engage in cation-π interactions with positively charged groups, which could either lead to denser compaction or prevent the interaction with phosphate ions.

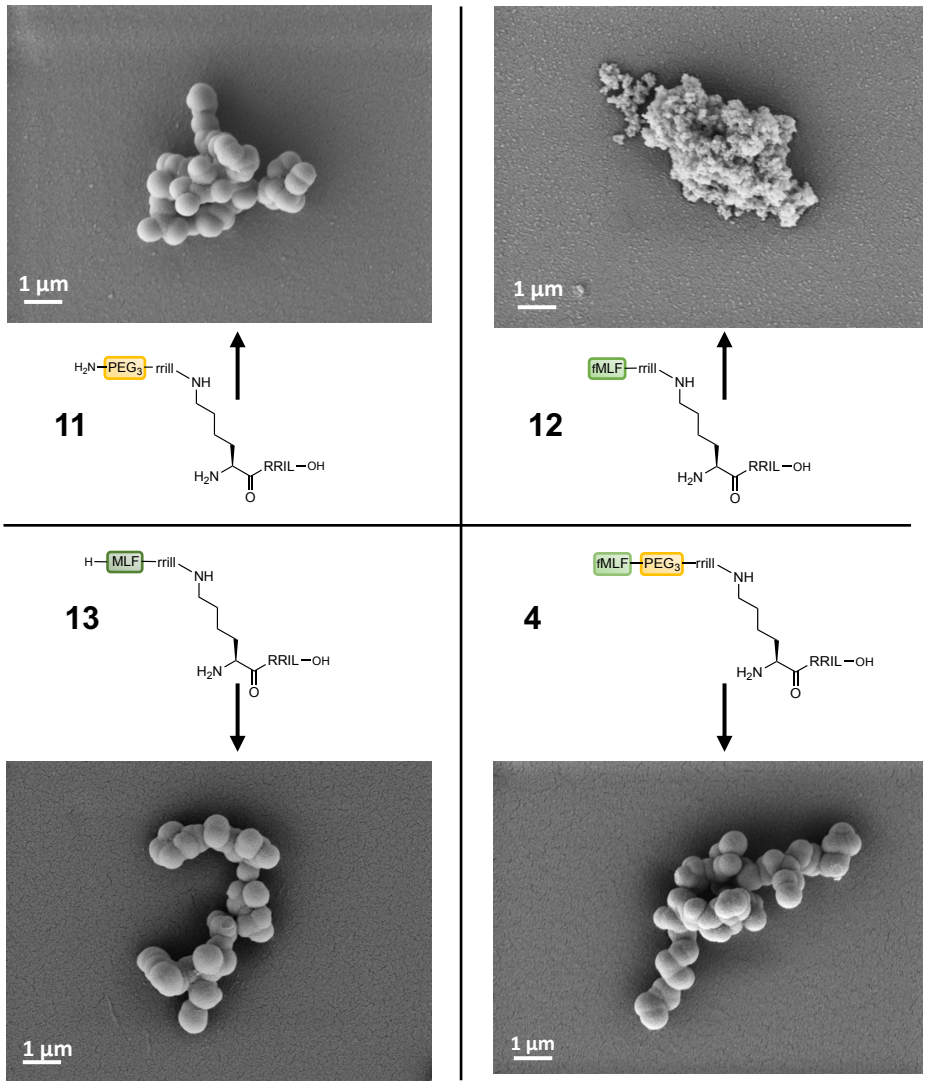

Figure 55 | Comparison of particles generated with peptides 11–13 and 4. The structure of the peptides as well as the corresponding particles are depicted. Peptide **11,** modified with PEG_3, and peptide **13**, modified with the tripeptide MLF, forms spherical particles, similar to peptide **4**. Peptide **12** generates cloud-like particles, which could maybe also be identified as very small spheres.

The particles generated by peptide **14**, featuring a linked Cy5 fluorophore, displayed an as yet unobserved morphology. Despite being spherical, they exhibited smaller spheres on top of the larger ones. This phenomenon might be attributed to intramolecular interactions of Cy5, involving π-stacking or cation-π interactions, which potentially prompt reduced growth. When peptide **14** is mixed with peptide **3** in a ratio of 1:99, the produced particles do no longer show smaller spherical particles (see **Figure 56**).

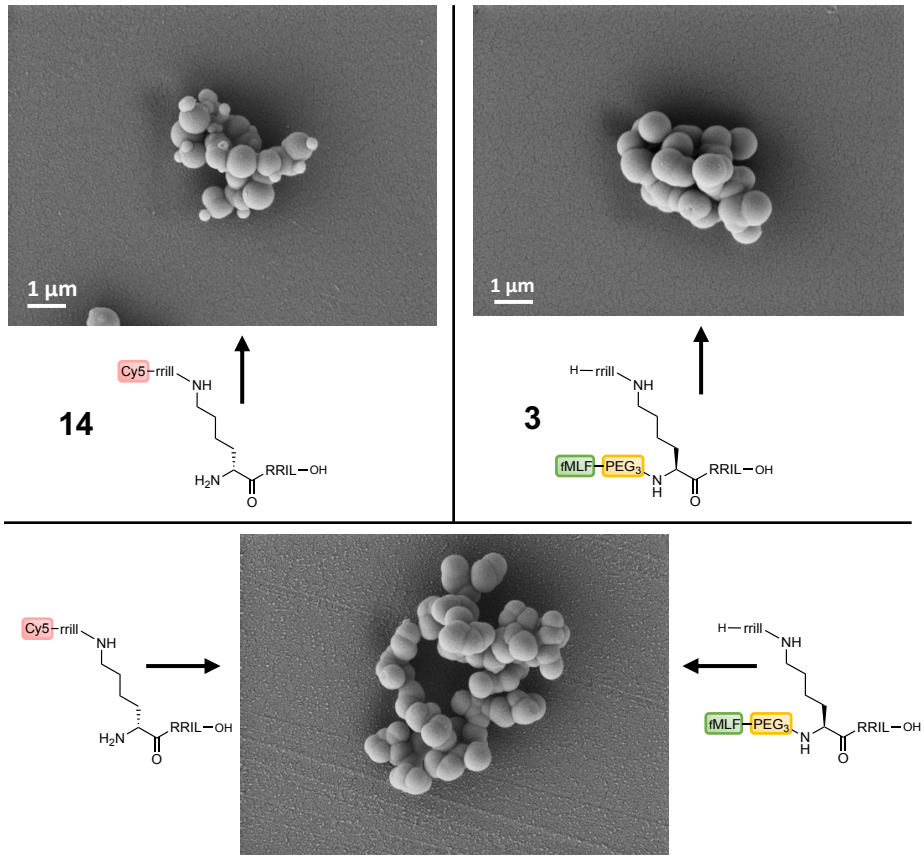

Figure 56 | Comparison of particles generated with peptides 14 and 3. The structure of the peptides as well as the corresponding particles are depicted. Peptide **14** produced spherical particles with smaller spherical particles on top. The bigger spherical particles are similar to the particles produced with peptide **3**. The mixture of 99% peptide **3** and 1% peptide **14** produced spherical particles without smaller ones visible.

In summary, all modified peptides self-assemble and precipitate silica particles. The formation of more densely packed self-assemblies serving as a template for rod-shaped particles is easily disturbed and leaves room only for small modifications. Otherwise, the peptides give rise to spherical particles. Moreover, the impact of the charged *N*-terminus seems to be an important part for self-assembly.

All conclusions drawn about the impact of the modifications on assembly and silica particle morphology require additional experimental support, which can be provided by a combination of NMR analysis and computational analysis, as previously demonstrated for peptide **1** and **2**.[1]

4.2 NMR analysis of peptide 7

The intriguing mix of two easily distinguishable particle morphologies formed by peptide **7** was further analyzed using NMR methods, with the aim of explaining the link between

chemical structures and peptide self-assembly, serving as a template for silica precipitation. These new findings were compared with published results on peptides **1** and **2** by Strobl *et al*.[1] The NMR studies were conducted and analyzed by Fanny Kozak, MSc BSc.

First, a comparison of total correlation spectroscopy (TOCSY) experiments with the peptide **7** dissolved in neat ddH_2O and in 50 mM phosphate buffer solution was performed (see **Figure 57A**). The amide backbone $^1H^N$ resonances were initially assigned in the aqueous solution for each amino acid, while incubation in phosphate buffered solution rendered several of the identified peaks inaccessible, due to broadening beyond the detection limit. Vanishing of the peaks indicates self-assembly and aggregation. Only the C-terminal I^9 and L^{10} were still detectable. That is in line with the TOCSY results obtained for peptides **1** and **2** (see **Figure 57B**).[1]

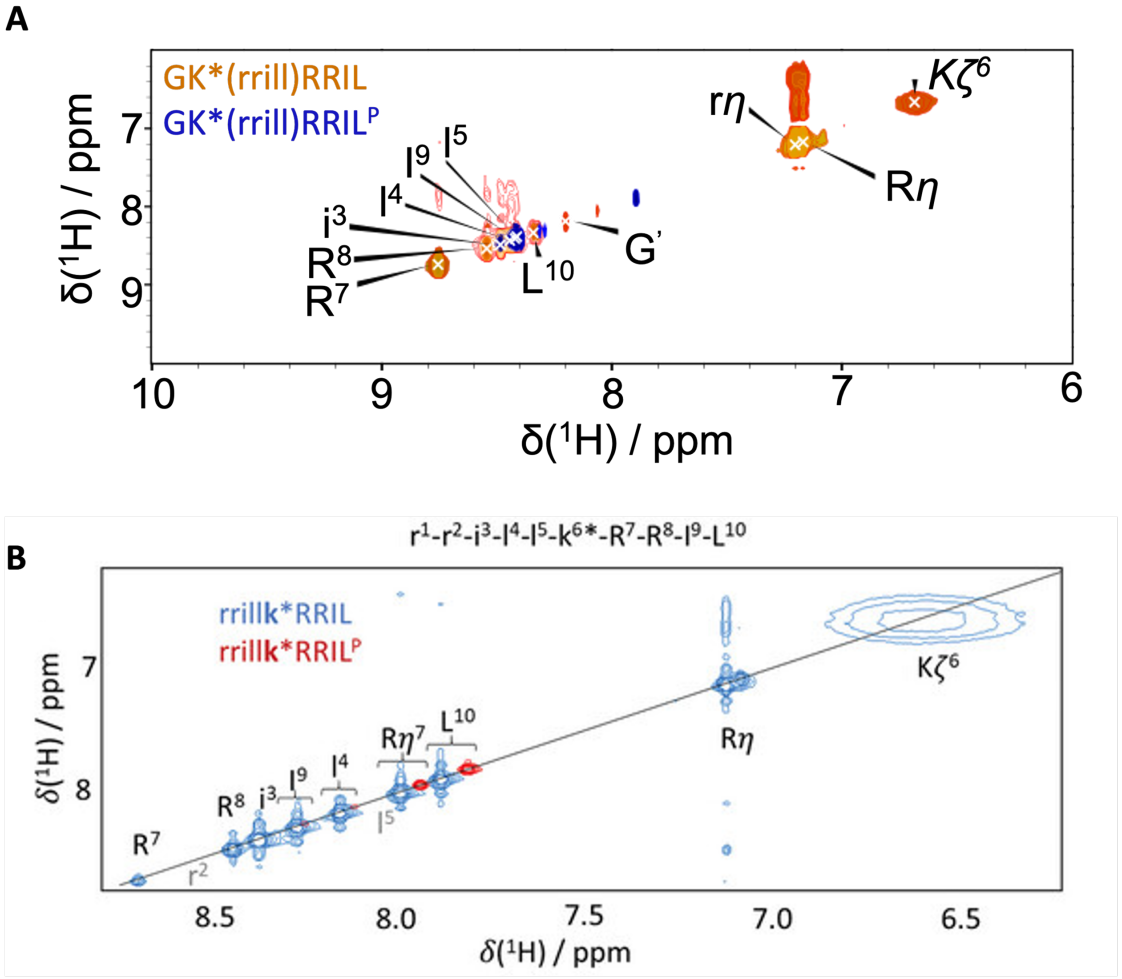

Figure 57 | Comparison of ^1H-^1H TOCSY results of H^N region. The resonance assignment is indicated. (A) Peptide **7** with the sequence G' $K^{6*}(r^1\ r^2\ i^3\ l^4\ l^5)R^7\ R^8\ l^9\ L^{10}$ was dissolved in neat ddH_2O (ochre) and in 50 mM phosphate buffer (blue). Most resonances vanish upon exposure to phosphate buffered, except l^9 and L^{10}. (B) The peptide **2** was dissolved in neat water (blue) and in 50 mM phosphate buffer (red) and showed similar results. The figure (B) was extracted from the open access research article by Strobl *et. al.* with permission of the author.[1]

Additionally, nuclear Overhauser effect spectroscopy (NOESY) experiments were conducted to provide insights into the molecular structure. Peptide **7** was again dissolved in 50 mM phosphate buffer and the results overlayed with the TOCSY spectrum (see **Figure 58A**) Two cross-peaks between water resonances and the amide $^{1}H^{N}$ of i^{3} and l^{9} could be identified. Interestingly the peptide **1** did not display any water cross peaks, indicating a higher aggregation density and possibly the formation of a secondary structure, where amide protons are engaged in hydrogen bonds (see **Figure 58B**). In contrast, peptide **2** with a central D-Lys, exhibited more water cross peaks than peptide **7** (see **Figure 58C**). The variation in aggregation density among the peptides points to distinct behavior in self-assembly, contributing to the different morphologies of the derived particles. The presence of both spherical and rod-shaped particle morphologies produced with peptide **7**, along with the higher number of water cross-peaks than observed for peptide **1** and smaller amount of water peaks than peptide **2** is in line with these observations.

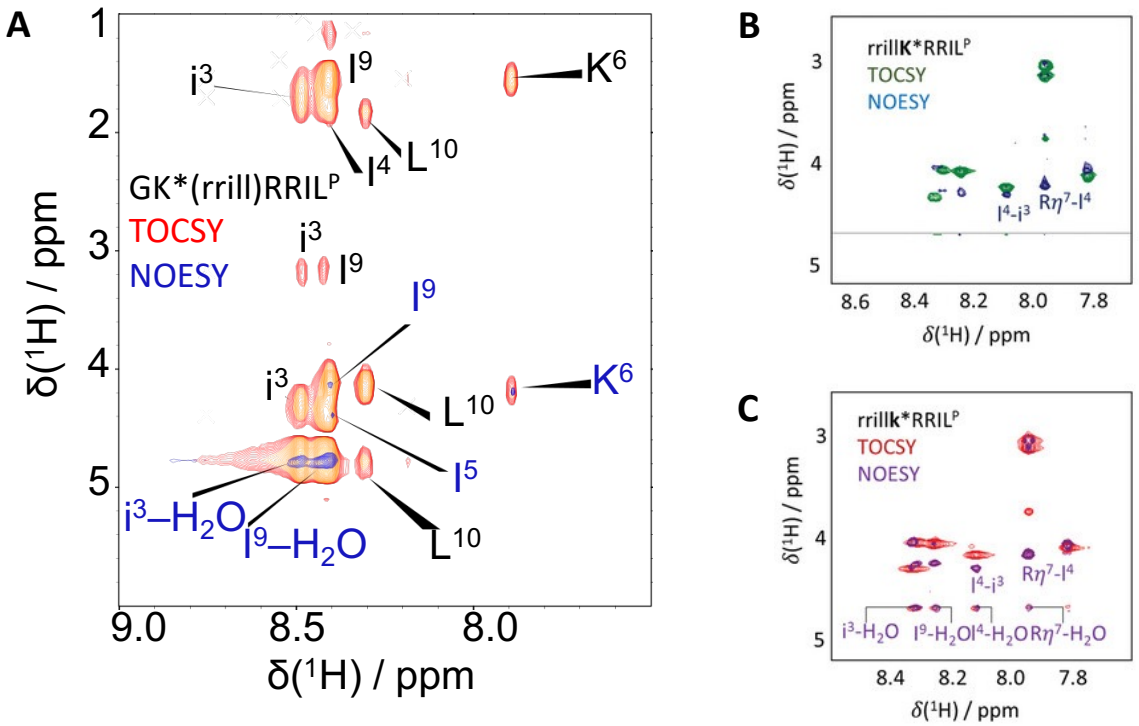

Figure 58 | Comparison of H^{N}/H^{α} region of ^{1}H-^{1}H TOCSY and NOESY results of peptide 7, 1 and 2. All peptides are dissolved in 50 mM phosphate buffer and the overlayed TOCSY and NOESY results are presented. (A) Peptide **7** exhibits NOESY water cross peaks of i^{3} and l^{9}, indicating solvent exposure and therefore smaller aggregation density. (B) In contrast, Peptide **1** shows no water cross peaks at all, suggesting high aggregation density. (C) Peptide **2** in comparison, displays even more water cross peaks than peptide **7** and is presumed to aggregate less. The figures (B) and (C) were extracted from the open access research article by Strobl *et. al.* with permission of the author.[1]

The enhanced propensity for aggregation in peptide **1** was further validated through diffusion-ordered spectroscopy (DOSY), revealing an average hydrodynamic radius (R_h) of 0.30 nm for peptide **1** assemblies and 1.01 nm for peptide **2** assemblies. Notably, peptide **7** falls in between these values with an R_h of 0.80 nm. Intriguingly, in pure water, both peptides **1** and **2** display an R_h of 0.23 nm, corresponding to their individual monomeric states, while peptide **7** exhibits an R_h of 0.80 nm, suggesting aggregation in ddH_2O. That contradicts the observations in the TOCSY experiment and is implausible with the absence of phosphate ions. Hence, it is necessary to repeat the DOSY experiment to determine whether the value of R_h in pure water can be reproduced or if an error occurred in the initial measurements.
The data suggests that the precipitation event relies on distinct templates formed in the solution. Moreover, the particle morphology is likely pre-established by the configurations of the precursors formed in the presence of phosphate ions.[1]

To assess the structure of the precursor, the silica coprecipitation of peptide **7** was investigated using real-time NMR. Therefore ^{1}H spectra were recorded every minute after addition of silicic acid to the peptide solution in 50 mM phosphate buffer. The data processing involved the determination of the intensity of the assigned peaks, which are then normalized and plotted against time.
The intensity curves of the amide H^N of each residue are depicted in **Figure 59A**. Arginine residues readily engage in aggregation, which makes them undetectable due to NMR size limitations. The other residues display a rapid intensity decrease upon addition of silicic acid and formation of silica-precipitates, plateauing at a small value around 50% of the intensity. Additionally, the rate was determined from bi-exponential fits of the data in **Figure 59A**. In **Figure 59B** two rate values for each amino acid are displayed. There is consistently a very small peak representing rapid precipitation and a larger value indicating slower precipitation. This pattern can be attributed to the rapid signal decrease at the beginning followed by a gradual decline. This trend is observable for each amino acid, except for I^4, which exhibits a relatively high error bar and should be approached with caution.

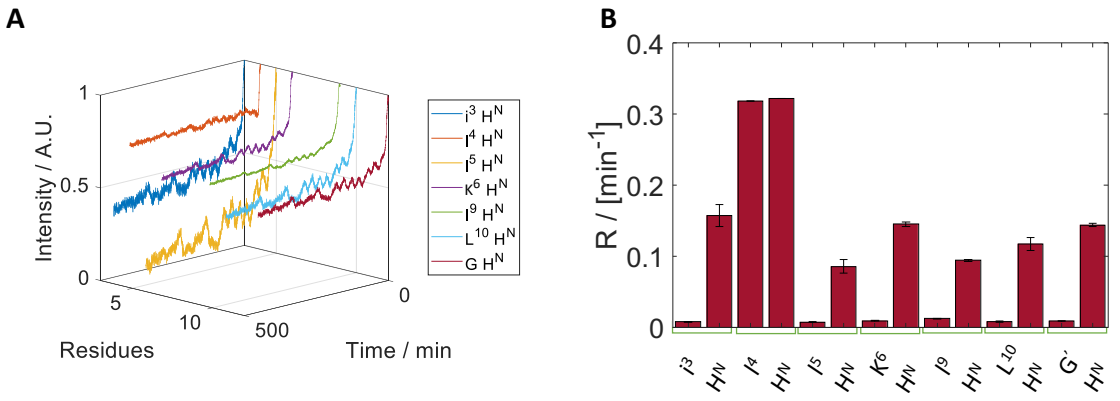

Figure 59 | Investigation of silica coprecipitation of peptide 7 using real time NMR. (A) Normalized intensity time traces of backbone H^N separated in residues. (B) The rate of precipitation of the amide H^N determined by biexponential fit of the intensity curves.

In summary, the results provide a partial explanation why both rod-shaped and spherical morphologies are produced by the peptide **7**. The precursor acts as a template in solution that can form assemblies similar to the ones observed for peptides **1** and **2** with respect to aggregation density and hydrodynamic radius r_H. The additional glycine residue influences the interplay between electrostatic and hydrophobic forces, resulting in alterations in self-assembly and consequently silica particle morphology. The real-time NMR suggests the formation of two distinct templates in solution, each precipitating with different kinetics. If the processes happen in parallel or in series has yet to be determined.

4.3 Peptide incorporation efficiency and release

The silica-precipitating peptides are incorporated into silica particles upon adding silicic acid to a peptide solution. The ratio of peptide associated with silica and remaining free in solution is referred to as the incorporation efficiency. After washing off the peptides in solution and drying, the particles contain a specific quantity of peptides. Previous studies suggested, that additionally to the peptides that are strongly bound to the silica, some only lightly adhere to the surface. This fraction of the peptide is easily released when particles are exposed to a new environment (see **Figure 60**).[38] Furthermore, at lower pH values, the negatively charged silica surface undergoes neutralization, resulting in a weakening of electrostatic interactions and subsequent release of the adherent peptides.[89]

Figure 60 | Illustration of peptide release after 1 h. Some of the peptides adhere to the negatively charged silica surface, while others are embedded in the silica. Due to incubation in buffered solution the peptides are released to a certain extent.

4.3.1 Incorporation efficiency

To assess peptide release from silica particles, the incorporation efficiency had to be determined first. Therefore, two samples were obtained during the silica particle production - one before and one after silica precipitation - and assessed using analytical HPLC, as described in **3.2.13**. The chromatograms were analyzed by integrating the area under the peak after precipitation ($area_{ap}$), which was then adjusted by multiplying it with 1.11 to account for dilution with silicic acid. This adjusted area was then divided by the area before precipitation ($area_{bp}$), resulting in the ratio of peptide in solution. The incorporation efficiency was calculated by **equation (1)**.

$$incorporation\ efficiency\ = 100 - \frac{Area_{ap} \cdot 1.11}{Area_{bp}} \cdot 100 \qquad \textbf{(1)}$$

The incorporation efficiencies of the peptides **3**, **4** and **6** were determined. The selection of these peptides was based on their inclusion of *N*-formyl peptide fMLF, which was later investigated for its role in immune system stimulation. Additionally, the peptides were chosen for their distinct isomeric characteristics. The results of the incorporation efficiency of the selected peptides are presented in **Table 7**. The peptides featuring the scaffold of peptide **1** demonstrate nearly identical results, whereas the peptide derived from the peptide **2** scaffold shows significantly lower incorporation efficiency. The rationale can only be speculated upon, but it is possible that the presence of D-Lys affects the structure in a manner that hinders the efficient siloxane bond formation.

Table 7 | Results of incorporation efficiency (n=3). The peptides **3**, **4** and **6** were analyzed.

Compound #	Sequence	Incorporation efficiency / %
3	fMLF-PEG_3K*(rrill)-RRIL	53.8 ± 5.4
4	K*(fMLF-PEG_3-rrill)-RRIL	54.6 ± 1.2
6	k*(fMLF-PEG_3-rrill)-RRIL	31.6 ± 4.3

4.3.2 Peptide release

Peptide release was performed as described in **3.2.14**. Again, peptides **3**, **4** and **6** containing the *N*-formyl peptide motif fMLF were analyzed. The release of peptides was assessed in RPMI medium to mimic a physiological environment with a pH of 7.4. Additionally, the release of peptides in an acidic environment was examined using 0.1 M citrate buffer at pH 4. The samples were taken after 1 h, 5 h and 24 h and assessed using analytical HPLC.

The obtained chromatograms were evaluated by integrating the areas under the peak ($area_{pr}$) and then they were divided by the incorporation efficiency and the peak area before precipitation ($area_{bp}$), which corresponds to a peptide solution of 2 mg·mL^{-1} (see **equation (2)**).

$$Peptide\ release\ = \frac{Area_{pr}}{Area_{bp} \cdot Incorporation\ efficiency} \cdot 10^4 \qquad \textbf{(2)}$$

The peptide release over time in RPMI medium and citrate buffer for the peptides **3**, **4** and **6** is illustrated in **Figure 61**. Notably, the overall peptide release is significantly higher at pH 4 compared to pH 7.4. Previous studies have indicated that some peptides adhere to the surface of the particles by ionic interactions, which are disrupted at lower pH, leading to higher detection of peptide in solution.[90] The influence of the components of RPMI including amino acids, vitamins and inorganic salt is not clear.

The peptide release in RPMI medium increases over the first 5 hours and then stabilizes at a plateau value of approximately 5% for peptides **3** and **6** and 10% for peptide **4** (see **Figure 61A**). In contrast, the peptide release in citrate buffer (see **Figure 61B**) is rapid, with the most substantial rise within the first hour, before reaching a plateau value. Peptides **4** and **6** level off at 30% peptide release, peptide 5 only releases about 20%.

The comparison of the different peptides reveals an additional trend. The peptide **4** exhibits the highest peptide release in both acidic and physiological pH, whereas peptide **3** showed the lowest release. That is particularly interesting, considering the fact that the two peptides are constitutional isomers. The peptides derived from peptide **1** show the same relative behavior in both conditions, while the peptide **6** with a D-Lys, demonstrates lower peptide release in RPMI medium and relatively high peptide release in citrate buffer.

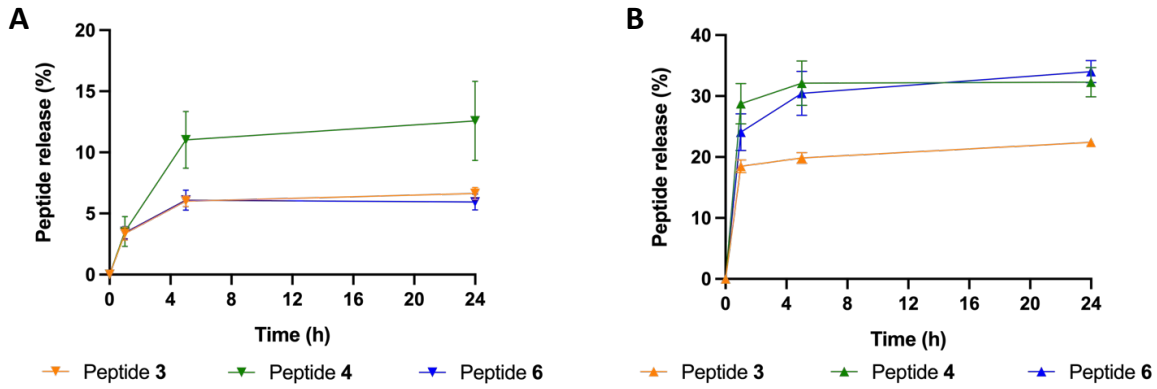

Figure 61 | Peptide release (A) in RPMI medium pH 7.4 and (B) in 0.1 M citrate buffer pH 4. The stereo and constitutional isomers peptide **3**, peptide **4** and peptide **6** were assessed in both conditions.

4.3.3 Discussion of peptide incorporation efficiency and release

The incorporation of the peptides into the particles is relatively low. In comparison, the scaffold peptide elongated with one cysteine at the *N*-terminus of D-Arg K*(crriII)RRIL displayed an incorporation efficiency of approximately 84%. Additionally, a similar peptide scaffold, K*(crriil)RRIL, conjugated with the antigens Bet v 1 and Phl p 5, showed incorporation efficiencies of 89%.[48] It is important to note that the peptides are not identical, but there is an evident variance. One possible factor contributing to this difference could be the incorporation of PEG_3, which enhances solubility and possibly interferes with silica formation. This assumption is supported by the observation that peptides incorporating PEG_3 did not form precipitates in the phosphate buffer, whereas peptides without the spacer formed precipitates in solution. Nevertheless, the peptides are successfully incorporated, and, crucially for applications as vaccine adjuvants, they exhibit consistent incorporation to a similar extent with minor variations.

Another important factor for applications of silica particles as delivery platforms is peptide release. The results revealed that the peptide release is rapid at first and then ceases at a plateau value. At a physiological pH of 7.4, peptides **3** and **6** both released up to 5%, while peptide **4** could release 10%. Under acidic pH conditions, peptides **4** and **6** were released up to 30%, while peptide **3** was released only up to 20%. The results align with previous

studies, which also demonstrate peptide release of 8% at neutral pH and 20% at pH 4.[48] As previously discussed the peptide release is dependent on the surface charge of silica. At neutral pH the silica surface is predominantly negatively charged, allowing some exchange of the positively charged peptides with ions in the buffer, resulting in a 5-10% release. At pH 4, most of the silica surface is uncharged, potentially leading to the release of most of the polycationic peptides.

4.4 Leukocyte activation assay

The introduction of the *N*-formyl peptide fMLF was primarily for its neutrophil stimulating properties, by activating the FPRs.[57] As outlined in the introduction, FPR activation leads to various responses, amongst others superoxide production. The response can be quantified using dihydro rhodamine (DHR) 123, which is oxidized to rhodamine by reactive oxygen species (ROS) (see **Figure 62**). Rhodamine emits fluorescence at a maximum of 525 nm upon excitation at 488 nm.[91]

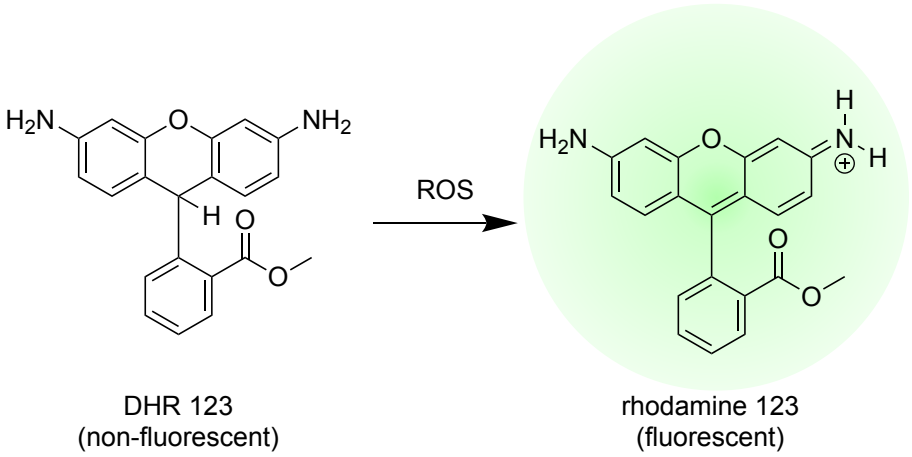

Figure 62 | Structure of DHR 123. The ROS oxidize DHR 123 to rhodamine 123, which is fluorescent and emits light at 528 nm.

The DHR assay was conducted by SyntabTherapeutics (Aachen) using fluorescence activated cell sorting (FACS) to investigate the rate of FPR activation in a human leukocyte cell population.

The peptides **3**, **4** and **6** were dissolved in phosphate buffer saline (PBS), and dilution series of 5 nM, 10 nM, 50 nM, 100 nM, 500 nM, 1 µM, 5 µM and 10 µM of peptides in cell suspensions were prepared. Moreover, also the corresponding particles of peptides **3**, **4** and **6** were suspended in PBS to obtain an estimated dilution series of 500 nM, 1 µM, 5 µM and 10 µM of peptides in cell suspension. The peptide concentration in the particles was estimated by the incorporation efficiency.

As a positive control phorbol myristate acetate (PMA), a known activator of NADPH oxidase, responsible for the production of ROS, was introduced at a concentration of 3 µM, while HHBE without any effector served as a negative control.[92] The cells were treated with the various effector concentrations and controls. The analysis was conducted by FACS, which sorted the cells based on rhodamine-positive cells, indicating FPR activation.

The results of the DHR assay of the peptides and particles are depicted in **Figure 63**. In **Figure 63A** the results for the peptides are illustrated, all exhibiting a consistent pattern. At low concentrations there are minimal rhodamine-positive cells, but from 50 nM onward the rhodamine positive cells increase steadily and converge around 65%. Similar, the corresponding particles display analogous behavior, stabilizing at approximately 60% rhodamine-positive (**Figure 63B**).
In summary, both peptides and particles activate the FPR at an acceptable rate, as indicated by the portion of rhodamine-positive cells. This is evident as the negative control, lacking any effector, exhibited only 0.15% rhodamine-positive cells, which can be considered negligible noise.

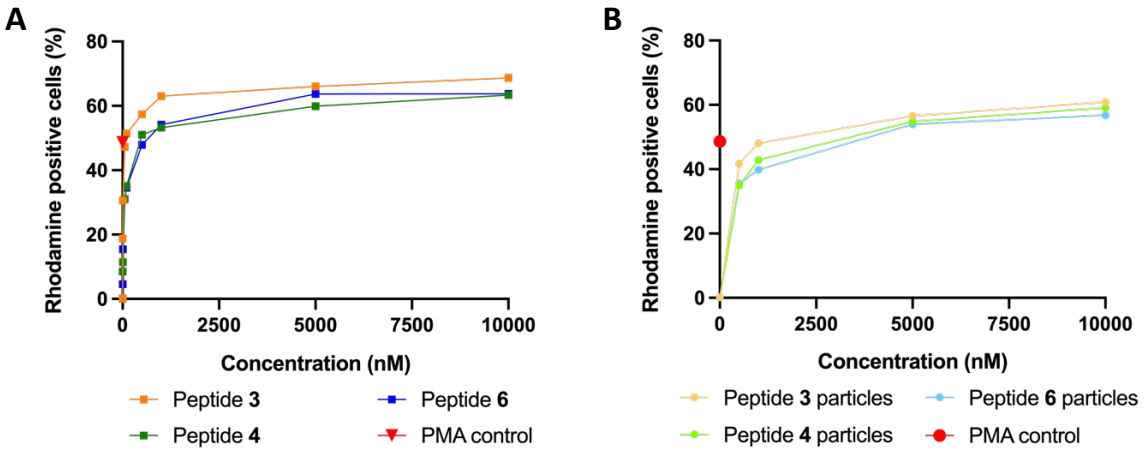

Figure 63 | Results of DHR assay. (A) DHR results for peptides at different concentrations and (B) DHR results for particles derived from the same peptides.

For a more comprehensive comparison the peptides and their corresponding particles are illustrated in one graph shown in **Figure 64**. The peptides exhibit superior FPR activation indicated by a higher number of rhodamine-positive cells. However, the particles derived from the peptides only demonstrate a slightly lower level of FPR activation.
Additionally, as discussed in **4.3.2** only the peptides adhering to the particles, constituting to 5–10%, are released and capable of activating the receptor, since the remaining proportion is tightly embedded in the silica with no possibility of release.

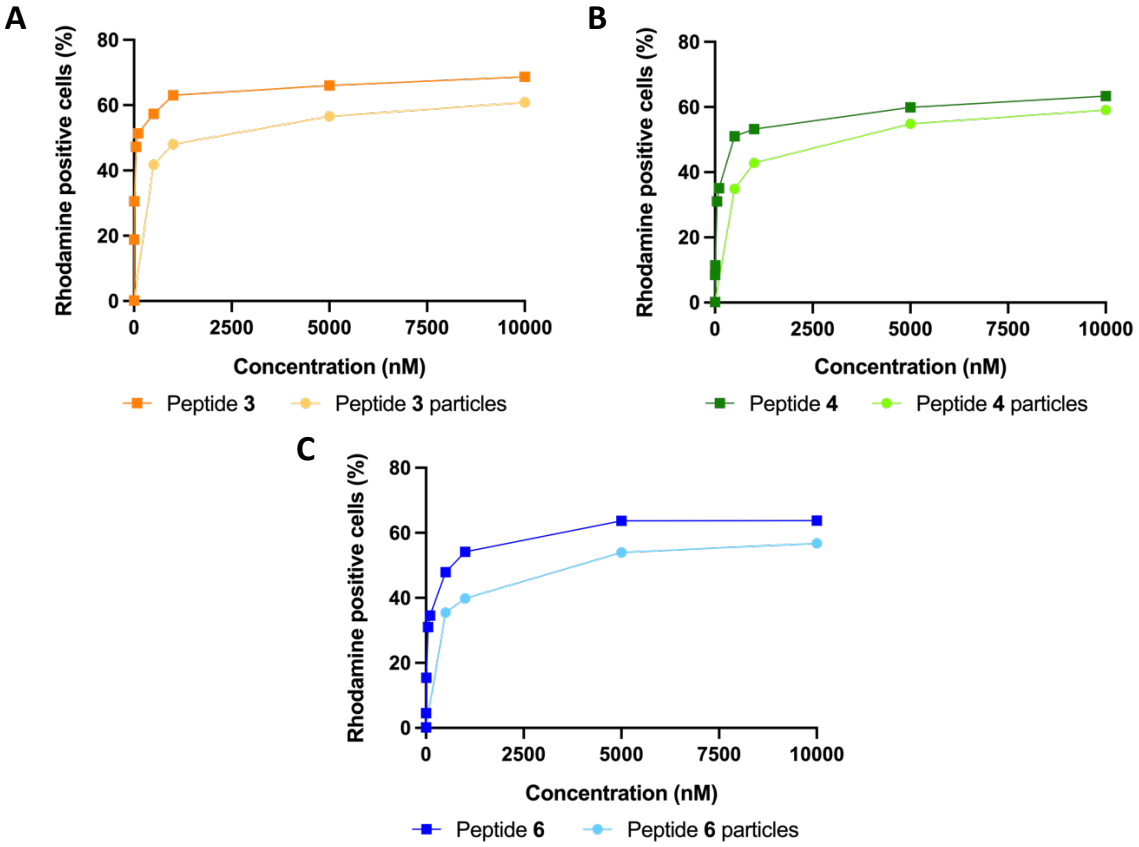

Figure 64 | DHR results comparing the peptide with their corresponding particle. (A) Results for peptide **3** and corresponding particles, (B) results for peptide **4** and corresponding particles and (C) results for peptide **6** and corresponding particles.

An additional DHR assay was performed using the particles prepared with 99% of either peptide **3**, **4** or **6** and 1% peptide **14**. The DHR assay results for particles incorporating the peptides tagged with Cy5 (see **Figure 65A**) are compared to the particles with the corresponding peptides only (see **Figure 65B**). The particles including peptide **14** were tested at higher concentrations (500 nM, 1 µM, 10 µM and 50 µM). Although the graphs may appear slightly different due to the higher concentrations, a closer examination reveals that they reach the same rhodamine-positive cell percentage at equivalent concentration. In summary, the incorporation of D-RRIL-Cy5 does not have an effect on the activation of FPR.

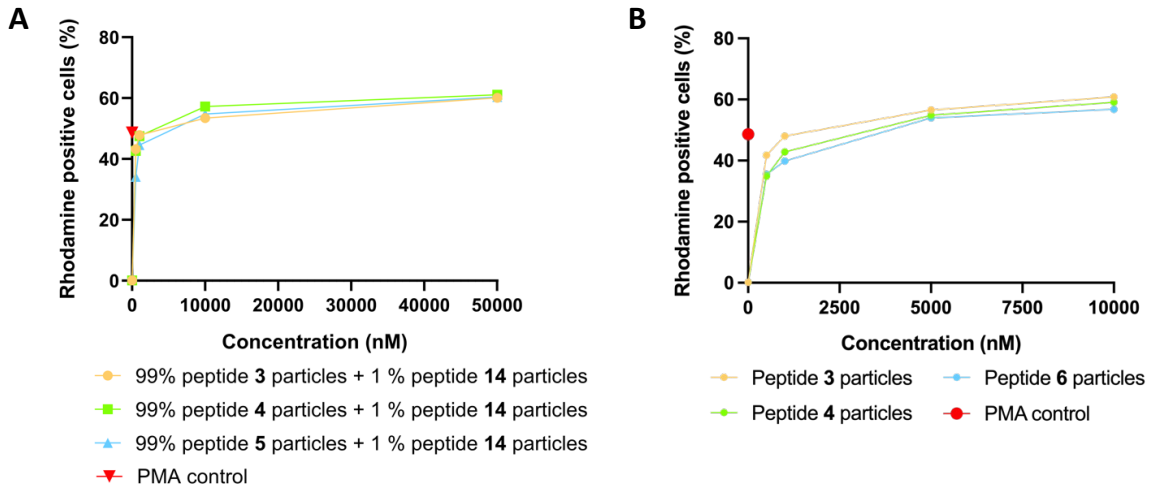

Figure 65 | DHR results. (A) Results for particles generated with 1% peptide **14** and 99% of either peptide **3**, **4** or **6**. (B) Results for particles generated with peptide **3**, **4** and **6**.

4.4.1 Discussion of the leukocyte activation assay

The results from the cellular assay are promising, as both the isolated peptides and those incorporated in the silica particles effectively activated FPR, inducing ROS production. This confirms the suitability of PEG_3 as a spacer, ensuring that fMLF can reach into the binding pocket of the FPR. There is no significant difference in the percentage of rhodamine-positive cells among the peptides, suggesting that the position of fMLF-PEG_3 incorporation and the scaffold peptide do not have an impact on FPR activation. Particularly noteworthy is that the particles induce comparable quantities of rhodamine-positive cells, indicating ROS production. It is important to consider that the peptide concentration in the particles was estimated based on the incorporation efficiency, encompassing both tightly embedded peptides in the silica and adherent peptides. Considering that only 5–10% of the peptides are released at physiological pH, the results should be only a fraction of the isolated peptides. However, silica particles also trigger ROS production independently of fMLF upon internalization, as evidenced in the literature.[48, 93, 94] This explains the increased ROS production. Further studies are required to determine the exact proportion of ROS production induced by silica particles derived from peptides lacking fMLF.

5 Conclusion and outlook

In total, fourteen peptides of different constitution and carrying a set of different modifications were successfully synthesized. All of them demonstrated the ability to precipitate silica particles, consistent with previous studies that showed that many modifications of the scaffold peptide do not obstruct the silica formation.[48] However, it was observed that modifications with three amino acids and more compromise the dense self-assembly required for rod-shaped particles, leading to less compact self-assembly and, consequently, the formation of spherical particles. Additionally, the charged *N*-terminus does seem to be involved in self-assembly, crucial for distinct particle morphology. Notably, one peptide was synthesized that formed both rod-shaped and spherical particles. NMR results revealed two silica precipitation processes progressing at different speed, resulting in the observed distinct morphologies. Even though predicting the morphology remains elusive, this study has enhanced our comprehension of modifications on the scaffold peptides.

Furthermore, the biomedical implications of the modification on the peptide scaffold, specifically its potential application as vaccine adjuvants were also examined. The immune stimulating properties of the fMLF modification was demonstrated on the basis of ROS production induced by both isolated peptides and particles. While both showed promising results, the ROS production in response to particles was relatively high. The increased effect can be attributed to the ROS generation induced by silica particles independent of fMLF, which is described in the literature.[95-97]

Some studies suggest that the phagocytosis of silica particles induces ROS production and, thus, triggers the NOD-, LRR- and pyrin domain-containing protein 3 (NLRP3) inflammasome. This activation leads to the release of pro-inflammatory cytokines, such as interleukin 1β (IL-1β) and tumor necrose factor α (TNF-α), subsequently promoting IL-6 production, indicative of a T_H2 skewed immune response.[93, 97, 98] Our group has previously demonstrated that silica particles derived from the peptide K*(crrill)-RRIL induce the production of pro-inflammatory cytokines, which suggest a T_H2-type immune response.[48] Although a more balanced T_H1/T_H2 immune response would be preferable for broad protection against pathogens and long-term immunity, the biomimetic silica particles show great potential for applications in vaccine adjuvants.[99] The easy production of the particles under mild conditions enables the adsorption or conjugation of sensitive cargo, such as peptide antigens. Moreover, silica particles derived from R5 exhibit excellent biocompatibility and have been observed to be internalized, as evidenced in human colon adenocarcinoma cells HT-29.[90] The results show, that the combination of the innate immune

system stimulating properties of fMLF with the delivery capabilities of silica particles holds great promise for their role as vaccine adjuvants.

6 References

(1) Strobl, J.; Kozak, F.; Kamalov, M.; Reichinger, D.; Kurzbach, D.; Becker, C. F. Understanding Self-Assembly of Silica-Precipitating Peptides to Control Silica Particle Morphology. *Adv Mater* **2023**, *35* (11), e2207586. DOI: 10.1002/adma.202207586 From NLM.

(2) Jaroniec, M. Silicon beyond the valley. *Nature Chemistry* **2009**, *1* (2), 166-166. DOI: 10.1038/nchem.173.

(3) Birchall, J. D. The essentiality of silicon in biology. *Chemical Society Reviews* **1995**, *24* (5), 351-357, 10.1039/CS9952400351. DOI: 10.1039/CS9952400351.

(4) Ehrlich, H.; Demadis, K. D.; Pokrovsky, O. S.; Koutsoukos, P. G. Modern Views on Desilicification: Biosilica and Abiotic Silica Dissolution in Natural and Artificial Environments. *Chemical Reviews* **2010**, *110* (8), 4656-4689. DOI: 10.1021/cr900334y.

(5) Currie, H. A.; Perry, C. C. Silica in plants: biological, biochemical and chemical studies. *Ann Bot* **2007**, *100* (7), 1383-1389. DOI: 10.1093/aob/mcm247 From NLM.

(6) DeMaster, D. J. Marine Silica Cycle. In *Encyclopedia of Ocean Sciences*, Steele, J. H. Ed.; Academic Press, 2001; pp 1659-1667.

(7) Epstein, E. SILICON. *Annu Rev Plant Physiol Plant Mol Biol* **1999**, *50*, 641-664. DOI: 10.1146/annurev.arplant.50.1.641 From NLM.

(8) Carlisle, E. M. Silicon: an essential element for the chick. *Science* **1972**, *178* (4061), 619-621. DOI: 10.1126/science.178.4061.619 From NLM.

(9) Farooq, M. A.; Dietz, K. J. Silicon as Versatile Player in Plant and Human Biology: Overlooked and Poorly Understood. *Front Plant Sci* **2015**, *6*, 994. DOI: 10.3389/fpls.2015.00994 From NLM.

(10) Norton, T. A.; Melkonian, M.; Andersen, R. A. Algal biodiversity. *Phycologia* **1996**, *35* (4), 308-326. DOI: 10.2216/i0031-8884-35-4-308.1.

(11) Hopkinson, B. M.; Dupont, C. L.; Allen, A. E.; Morel, F. M. Efficiency of the CO2-concentrating mechanism of diatoms. *Proc Natl Acad Sci U S A* **2011**, *108* (10), 3830-3837. DOI: 10.1073/pnas.1018062108 From NLM.

(12) Field, C. B.; Behrenfeld, M. J.; Randerson, J. T.; Falkowski, P. Primary production of the biosphere: integrating terrestrial and oceanic components. *Science* **1998**, *281* (5374), 237-240. DOI: 10.1126/science.281.5374.237 From NLM.

(13) Armbrust, E. V. The life of diatoms in the world's oceans. *Nature* **2009**, *459* (7244), 185-192. DOI: 10.1038/nature08057 From NLM.

(14) Nelson, D. M.; Tréguer, P.; Brzezinski, M. A.; Leynaert, A.; Quéguiner, B. Production and dissolution of biogenic silica in the ocean: Revised global estimates, comparison with

regional data and relationship to biogenic sedimentation. *Global Biogeochemical Cycles* **1995**, *9* (3), 359-372. DOI: https://doi.org/10.1029/95GB01070 (acccessed 2023/10/30).

(15) Round, F. E.; M., C. R.; G., M. D. The diatoms: biology and morphology of the genera. *Journal of the Marine Biological Association of the United Kingdom* **1990**, *70* (4), 924-924. DOI: 10.1017/S0025315400059245 From Cambridge University Press Cambridge Core.

(16) Mann, D. G.; Droop, S. J. M. 3. Biodiversity, biogeography and conservation of diatoms. *Hydrobiologia* **1996**, *336* (1), 19-32. DOI: 10.1007/BF00010816.

(17) Thamatrakoln, K.; Alverson, A. J.; Hildebrand, M. Comparative sequence analysis of diatom silicon transporters: Toward a mechanistic model of silicon transport. *Journal of Phycology* **2006**, *42* (4), 822-834. DOI: https://doi.org/10.1111/j.1529-8817.2006.00233.x (acccessed 2023/11/02).

(18) Martin-Jézéquel, V.; Hildebrand, M.; Brzezinski, M. A. SILICON METABOLISM IN DIATOMS: IMPLICATIONS FOR GROWTH *Journal of Phycology* **2000**, *36* (5), 821-840. DOI: https://doi.org/10.1046/j.1529-8817.2000.00019.x (acccessed 2023/10/24).

(19) Drum, R. W.; Pankratz, H. S. POST MITOTIC FINE STRUCTURE OF GOMPHONEMA PARVULUM. *J Ultrastruct Res* **1964**, *10*, 217-223. DOI: 10.1016/s0022-5320(64)80006-x From NLM.

(20) Kröger, N.; Poulsen, N. Diatoms-from cell wall biogenesis to nanotechnology. *Annu Rev Genet* **2008**, *42*, 83-107. DOI: 10.1146/annurev.genet.41.110306.130109 From NLM.

(21) Foo, C. W.; Huang, J.; Kaplan, D. L. Lessons from seashells: silica mineralization via protein templating. *Trends Biotechnol* **2004**, *22* (11), 577-585. DOI: 10.1016/j.tibtech.2004.09.011 From NLM.

(22) Hoagland, K. D.; Rosowski, J. R.; Gretz, M. R.; Roemer, S. C. DIATOM EXTRACELLULAR POLYMERIC SUBSTANCES: FUNCTION, FINE STRUCTURE, CHEMISTRY, AND PHYSIOLOGY. *Journal of Phycology* **1993**, *29* (5), 537-566. DOI: https://doi.org/10.1111/j.0022-3646.1993.00537.x (acccessed 2023/11/03).

(23) Tesson, B.; Hildebrand, M. Characterization and localization of insoluble organic matrices associated with diatom cell walls: insight into their roles during cell wall formation. *PLoS One* **2013**, *8* (4), e61675. DOI: 10.1371/journal.pone.0061675 From NLM.

(24) Brunner, E.; Richthammer, P.; Ehrlich, H.; Paasch, S.; Simon, P.; Ueberlein, S.; van Pée, K. H. Chitin-based organic networks: an integral part of cell wall biosilica in the diatom Thalassiosira pseudonana. *Angew Chem Int Ed Engl* **2009**, *48* (51), 9724-9727. DOI: 10.1002/anie.200905028 From NLM.

(25) Bidle, K. D.; Azam, F. Accelerated dissolution of diatom silica by marine bacterial assemblages. *Nature* **1999**, *397* (6719), 508-512. DOI: 10.1038/17351.

(26) Kröger, N.; Lehmann, G.; Rachel, R.; Sumper, M. Characterization of a 200-kDa diatom protein that is specifically associated with a silica-based substructure of the cell wall. *Eur J Biochem* **1997**, *250* (1), 99-105. DOI: 10.1111/j.1432-1033.1997.00099.x From NLM.

(27) Kröger, N.; Wetherbee, R. Pleuralins are Involved in Theca Differentiation in the Diatom Cylindrotheca fusiformis. *Protist* **2000**, *151* (3), 263-273. DOI: https://doi.org/10.1078/1434-4610-00024.

(28) Davis, A. K.; Hildebrand, M.; Palenik, B. A STRESS-INDUCED PROTEIN ASSOCIATED WITH THE GIRDLE BAND REGION OF THE DIATOM THALASSIOSIRA PSEUDONANA (BACILLARIOPHYTA)1. *Journal of Phycology* **2005**, *41* (3), 577-589. DOI: https://doi.org/10.1111/j.1529-8817.2005.00076.x (acccessed 2023/11/03).

(29) Wenzl, S.; Hett, R.; Richthammer, P.; Sumper, M. Silacidins: highly acidic phosphopeptides from diatom shells assist in silica precipitation in vitro. *Angew Chem Int Ed Engl* **2008**, *47* (9), 1729-1732. DOI: 10.1002/anie.200704994 From NLM.

(30) Lechner, C. C.; Becker, C. F. Silaffins in Silica Biomineralization and Biomimetic Silica Precipitation. *Mar Drugs* **2015**, *13* (8), 5297-5333. DOI: 10.3390/md13085297 From NLM.

(31) Kröger, N.; Lorenz, S.; Brunner, E.; Sumper, M. Self-assembly of highly phosphorylated silaffins and their function in biosilica morphogenesis. *Science* **2002**, *298* (5593), 584-586. DOI: 10.1126/science.1076221 From NLM.

(32) Kröger, N.; Deutzmann, R.; Sumper, M. Polycationic peptides from diatom biosilica that direct silica nanosphere formation. *Science* **1999**, *286* (5442), 1129-1132. DOI: 10.1126/science.286.5442.1129 From NLM.

(33) Pamirsky, I. E.; Golokhvast, K. S. Origin and status of homologous proteins of biomineralization (biosilicification) in the taxonomy of phylogenetic domains. *Biomed Res Int* **2013**, *2013*, 397278. DOI: 10.1155/2013/397278 From NLM.

(34) Poulsen, N.; Kröger, N. Silica morphogenesis by alternative processing of silaffins in the diatom Thalassiosira pseudonana. *J Biol Chem* **2004**, *279* (41), 42993-42999. DOI: 10.1074/jbc.M407734200 From NLM.

(35) Kröger, N.; Deutzmann, R.; Sumper, M. Silica-precipitating Peptides from Diatoms: The chemical structure of silaffin-1A from Cylindrotheca fusiformis *Journal of Biological Chemistry* **2001**, *276* (28), 26066-26070. DOI: 10.1074/jbc.M102093200 (acccessed 2023/11/04).

(36) Lutz, K.; Gröger, C.; Sumper, M.; Brunner, E. Biomimetic silica formation: Analysis of the phosphate-induced self-assembly of polyamines. *Physical Chemistry Chemical Physics* **2005**, *7* (14), 2812-2815, 10.1039/B505945C. DOI: 10.1039/B505945C.

(37) Patwardhan, S. V.; Shiba, K.; Schröder, H. C.; Müller, W. E. G.; Clarson, S. J.; Perry, C. C. The Interaction of 'Silicon' with Proteins: Part 2. The Rold of Bioinspired Peptide and Recombinant Proteins in Silica Polymerization. In *Science and Technology of Silicones and Silicone-Modified Materials*, ACS Symposium Series, Vol. 964; American Chemical Society, 2007; pp 328-347.

(38) Lechner, C. C.; Becker, C. F. Modified silaffin R5 peptides enable encapsulation and release of cargo molecules from biomimetic silica particles. *Bioorg Med Chem* **2013**, *21* (12), 3533-3541. DOI: 10.1016/j.bmc.2013.04.006 From NLM.

(39) Knecht, M. R.; Wright, D. W. Functional analysis of the biomimetic silica precipitating activity of the R5 peptide from Cylindrotheca fusiformis. *Chemical Communications* **2003**, (24), 3038-3039, 10.1039/B309074D. DOI: 10.1039/B309074D.

(40) Lechner, C. C.; Becker, C. F. A sequence-function analysis of the silica precipitating silaffin R5 peptide. *J Pept Sci* **2014**, *20* (2), 152-158. DOI: 10.1002/psc.2577 From NLM.

(41) Lutz, H.; Jaeger, V.; Schmüser, L.; Bonn, M.; Pfaendtner, J.; Weidner, T. The Structure of the Diatom Silaffin Peptide R5 within Freestanding Two-Dimensional Biosilica Sheets.

Angew Chem Int Ed Engl **2017**, *56* (28), 8277-8280. DOI: 10.1002/anie.201702707 From NLM.

(42) Kamalov, M.; Capel, P. D.; Rentenberger, C.; Müllner, A. R. M.; Peterlik, H.; Becker, C. F. W. Silaffin-Inspired Peptide Assemblies Template Silica Particles with Variable Morphologies. *ChemNanoMat* **2018**, *4* (12), 1209-1213. DOI: https://doi.org/10.1002/cnma.201800340 (acccessed 2023/11/07).

(43) Berthod, A. Silica: backbone material of liquid chromatographic column packings. *Journal of Chromatography A* **1991**, *549*, 1-28. DOI: https://doi.org/10.1016/S0021-9673(00)91415-8.

(44) Kumar, S.; Malik, M. M.; Purohit, R. Synthesis Methods of Mesoporous Silica Materials. *Materials Today: Proceedings* **2017**, *4* (2, Part A), 350-357. DOI: https://doi.org/10.1016/j.matpr.2017.01.032.

(45) Zhao, S.; Zhang, S.; Ma, J.; Fan, L.; Yin, C.; Lin, G.; Li, Q. Double loaded self-decomposable SiO2 nanoparticles for sustained drug release. *Nanoscale* **2015**, *7* (39), 16389-16398, 10.1039/C5NR03029C. DOI: 10.1039/C5NR03029C.

(46) Zhang, C.; Xie, H.; Zhang, Z.; Wen, B.; Cao, H.; Bai, Y.; Che, Q.; Guo, J.; Su, Z. Applications and Biocompatibility of Mesoporous Silica Nanocarriers in the Field of Medicine. *Front Pharmacol* **2022**, *13*, 829796. DOI: 10.3389/fphar.2022.829796 From NLM.

(47) Croissant, J. G.; Fatieiev, Y.; Khashab, N. M. Degradability and Clearance of Silicon, Organosilica, Silsesquioxane, Silica Mixed Oxide, and Mesoporous Silica Nanoparticles. *Advanced Materials* **2017**, *29* (9), 1604634. DOI: https://doi.org/10.1002/adma.201604634 (acccessed 2023/11/14).

(48) Reichinger, D.; Reithofer, M.; Hohagen, M.; Drinic, M.; Tobias, J.; Wiedermann, U.; Kleitz, F.; Jahn-Schmid, B.; Becker, C. F. W. A Biomimetic, Silaffin R5-Based Antigen Delivery Platform. In *Pharmaceutics*, 2023; Vol. 15.

(49) Trewyn, B. G.; Nieweg, J. A.; Zhao, Y.; Lin, V. S. Y. Biocompatible mesoporous silica nanoparticles with different morphologies for animal cell membrane penetration. *Chemical Engineering Journal* **2008**, *137* (1), 23-29. DOI: https://doi.org/10.1016/j.cej.2007.09.045.

(50) Greenwood, B. The contribution of vaccination to global health: past, present and future. *Philos Trans R Soc Lond B Biol Sci* **2014**, *369* (1645), 20130433. DOI: 10.1098/rstb.2013.0433 From NLM.

(51) Pollard, A. J.; Bijker, E. M. A guide to vaccinology: from basic principles to new developments. *Nat Rev Immunol* **2021**, *21* (2), 83-100. DOI: 10.1038/s41577-020-00479-7 From NLM.

(52) Vogel, F. R. Adjuvants in perspective. *Dev Biol Stand* **1998**, *92*, 241-248. From NLM.

(53) Kenney, R. T.; Edelman, R. Survey of human-use adjuvants. *Expert Rev Vaccines* **2003**, *2* (2), 167-188. DOI: 10.1586/14760584.2.2.167 From NLM.

(54) Reed, S. G.; Orr, M. T.; Fox, C. B. Key roles of adjuvants in modern vaccines. *Nature Medicine* **2013**, *19* (12), 1597-1608. DOI: 10.1038/nm.3409.

(55) Reed, S. G.; Bertholet, S.; Coler, R. N.; Friede, M. New horizons in adjuvants for vaccine development. *Trends Immunol* **2009**, *30* (1), 23-32. DOI: 10.1016/j.it.2008.09.006 From NLM.

(56) Platt, A.; Wetzler, L. Innate immunity and vaccines. *Curr Top Med Chem* **2013**, *13* (20), 2597-2608. DOI: 10.2174/15680266113136660185 From NLM.

(57) Kowalczyk, A.; Doener, F.; Zanzinger, K.; Noth, J.; Baumhof, P.; Fotin-Mleczek, M.; Heidenreich, R. Self-adjuvanted mRNA vaccines induce local innate immune responses that lead to a potent and boostable adaptive immunity. *Vaccine* **2016**, *34* (33), 3882-3893. DOI: 10.1016/j.vaccine.2016.05.046 From NLM.

(58) Brito, L. A.; Malyala, P.; O'Hagan, D. T. Vaccine adjuvant formulations: a pharmaceutical perspective. *Semin Immunol* **2013**, *25* (2), 130-145. DOI: 10.1016/j.smim.2013.05.007 From NLM.

(59) Schijns, V. E. Immunological concepts of vaccine adjuvant activity. *Curr Opin Immunol* **2000**, *12* (4), 456-463. DOI: 10.1016/s0952-7915(00)00120-5 From NLM.

(60) Aguilar, J. C.; Rodríguez, E. G. Vaccine adjuvants revisited. *Vaccine* **2007**, *25* (19), 3752-3762. DOI: 10.1016/j.vaccine.2007.01.111 From NLM.

(61) Tomai, M. A.; Johnson, A. G. T cell and interferon-gamma involvement in the adjuvant action of a detoxified endotoxin. *J Biol Response Mod* **1989**, *8* (6), 625-643. From NLM.

(62) HogenEsch, H.; O'Hagan, D. T.; Fox, C. B. Optimizing the utilization of aluminum adjuvants in vaccines: you might just get what you want. *npj Vaccines* **2018**, *3* (1), 51. DOI: 10.1038/s41541-018-0089-x.

(63) Sokolovska, A.; Hem, S. L.; HogenEsch, H. Activation of dendritic cells and induction of CD4(+) T cell differentiation by aluminum-containing adjuvants. *Vaccine* **2007**, *25* (23), 4575-4585. DOI: 10.1016/j.vaccine.2007.03.045 From NLM.

(64) Pulendran, B.; S. Arunachalam, P.; O'Hagan, D. T. Emerging concepts in the science of vaccine adjuvants. *Nature Reviews Drug Discovery* **2021**, *20* (6), 454-475. DOI: 10.1038/s41573-021-00163-y.

(65) Zhao, T.; Cai, Y.; Jiang, Y.; He, X.; Wei, Y.; Yu, Y.; Tian, X. Vaccine adjuvants: mechanisms and platforms. *Signal Transduction and Targeted Therapy* **2023**, *8* (1), 283. DOI: 10.1038/s41392-023-01557-7.

(66) Migeotte, I.; Communi, D.; Parmentier, M. Formyl peptide receptors: a promiscuous subfamily of G protein-coupled receptors controlling immune responses. *Cytokine Growth Factor Rev* **2006**, *17* (6), 501-519. DOI: 10.1016/j.cytogfr.2006.09.009 From NLM.

(67) McDonald, B.; Pittman, K.; Menezes, G. B.; Hirota, S. A.; Slaba, I.; Waterhouse, C. C.; Beck, P. L.; Muruve, D. A.; Kubes, P. Intravascular danger signals guide neutrophils to sites of sterile inflammation. *Science* **2010**, *330* (6002), 362-366. DOI: 10.1126/science.1195491 From NLM.

(68) Honda, M.; Takeichi, T.; Hashimoto, S.; Yoshii, D.; Isono, K.; Hayashida, S.; Ohya, Y.; Yamamoto, H.; Sugawara, Y.; Inomata, Y. Intravital Imaging of Neutrophil Recruitment Reveals the Efficacy of FPR1 Blockade in Hepatic Ischemia-Reperfusion Injury. *J Immunol* **2017**, *198* (4), 1718-1728. DOI: 10.4049/jimmunol.1601773 From NLM.

(69) Richard, D. Y.; François, B.; Ji Ming, W.; Claes, D.; Craig, G.; Marc, P.; Charles, N. S.; Philip, M. M. International Union of Basic and Clinical Pharmacology. LXXIII. Nomenclature for the Formyl Peptide Receptor (FPR) Family. *Pharmacological Reviews* **2009**, *61* (2), 119. DOI: 10.1124/pr.109.001578.

(70) Weiß, E.; Kretschmer, D. Formyl-Peptide Receptors in Infection, Inflammation, and Cancer. *Trends Immunol* **2018**, *39* (10), 815-829. DOI: 10.1016/j.it.2018.08.005 From NLM.

(71) Boulay, F.; Tardif, M.; Brouchon, L.; Vignais, P. Synthesis and use of a novel N-formyl peptide derivative to isolate a human N-formyl peptide receptor cDNA. *Biochem Biophys Res Commun* **1990**, *168* (3), 1103-1109. DOI: 10.1016/0006-291x(90)91143-g From NLM.

(72) Dahlgren, C.; Gabl, M.; Holdfeldt, A.; Winther, M.; Forsman, H. Basic characteristics of the neutrophil receptors that recognize formylated peptides, a danger-associated molecular pattern generated by bacteria and mitochondria. *Biochem Pharmacol* **2016**, *114*, 22-39. DOI: 10.1016/j.bcp.2016.04.014 From NLM.

(73) Wang, W.; Liu, X.; Zheng, X.; Jin, H. J.; Li, X. Biomineralization: An Opportunity and Challenge of Nanoparticle Drug Delivery Systems for Cancer Therapy. *Advanced Healthcare Materials* **2020**, *9* (22), 2001117. DOI: https://doi.org/10.1002/adhm.202001117 (acccessed 2023/10/28).

(74) Walther, A.; Riehemann, K.; Gerke, V. A Novel Ligand of the Formyl Peptide Receptor: Annexin I Regulates Neutrophil Extravasation by Interacting with the FPR. *Molecular Cell* **2000**, *5* (5), 831-840. DOI: https://doi.org/10.1016/S1097-2765(00)80323-8.

(75) Liu, Y.; Chen, K.; Wang, J. M. Chapter 91 - FPR Ligands. In *Handbook of Biologically Active Peptides (Second Edition)*, Kastin, A. J. Ed.; Academic Press, 2013; pp 671-680.

(76) Bokoch, G. M. Chemoattractant signaling and leukocyte activation. *Blood* **1995**, *86* (5), 1649-1660. From NLM.

(77) Dorward, D. A.; Lucas, C. D.; Chapman, G. B.; Haslett, C.; Dhaliwal, K.; Rossi, A. G. The Role of Formylated Peptides and Formyl Peptide Receptor 1 in Governing Neutrophil Function during Acute Inflammation. *The American Journal of Pathology* **2015**, *185* (5), 1172-1184. DOI: https://doi.org/10.1016/j.ajpath.2015.01.020.

(78) Zhao, H. F.; Wang, J.; Tony To, S. S. The phosphatidylinositol 3-kinase/Akt and c-Jun N-terminal kinase signaling in cancer: Alliance or contradiction? (Review). *Int J Oncol* **2015**, *47* (2), 429-436. DOI: 10.3892/ijo.2015.3052 From NLM.

(79) O'Flaherty, J. T.; Jacobson, D. P.; Redman, J. F.; Rossi, A. G. Translocation of protein kinase C in human polymorphonuclear neutrophils. Regulation by cytosolic Ca2(+)-independent and Ca2(+)-dependent mechanisms. *J Biol Chem* **1990**, *265* (16), 9146-9152. From NLM.

(80) Kim, C.; Marchal, C. C.; Penninger, J.; Dinauer, M. C. The hemopoietic Rho/Rac guanine nucleotide exchange factor Vav1 regulates N-formyl-methionyl-leucyl-phenylalanine-activated neutrophil functions. *J Immunol* **2003**, *171* (8), 4425-4430. DOI: 10.4049/jimmunol.171.8.4425 From NLM.

(81) Lopez-Ilasaca, M.; Crespo, P.; Pellici, P. G.; Gutkind, J. S.; Wetzker, R. Linkage of G Protein-Coupled Receptors to the MAPK Signaling Pathway Through PI 3-Kinase γ. *Science* **1997**, *275* (5298), 394-397. DOI: 10.1126/science.275.5298.394 (acccessed 2023/11/09).

(82) Quehenberger, O.; Prossnitz, E. R.; Cavanagh, S. L.; Cochrane, C. G.; Ye, R. D. Multiple domains of the N-formyl peptide receptor are required for high-affinity ligand binding. Construction and analysis of chimeric N-formyl peptide receptors. *J Biol Chem* **1993**, *268* (24), 18167-18175. From NLM.

(83) Gao, J. L.; Murphy, P. M. Species and subtype variants of the N-formyl peptide chemotactic receptor reveal multiple important functional domains. *J Biol Chem* **1993**, *268* (34), 25395-25401. From NLM.

(84) Mills, J. S.; Miettinen, H. M.; Cummings, D.; Jesaitis, A. J. Characterization of the binding site on the formyl peptide receptor using three receptor mutants and analogs of Met-Leu-Phe and Met-Met-Trp-Leu-Leu. *J Biol Chem* **2000**, *275* (50), 39012-39017. DOI: 10.1074/jbc.M003081200 From NLM.

(85) Chen, G.; Wang, X.; Liao, Q.; Ge, Y.; Jiao, H.; Chen, Q.; Liu, Y.; Lyu, W.; Zhu, L.; van Zundert, G. C. P.; et al. Structural basis for recognition of N-formyl peptides as pathogen-associated molecular patterns. *Nature Communications* **2022**, *13* (1), 5232. DOI: 10.1038/s41467-022-32822-y.

(86) Kaiser, E.; Colescott, R. L.; Bossinger, C. D.; Cook, P. I. Color test for detection of free terminal amino groups in the solid-phase synthesis of peptides. *Anal Biochem* **1970**, *34* (2), 595-598. DOI: 10.1016/0003-2697(70)90146-6 From NLM.

(87) Schindelin, J.; Arganda-Carreras, I.; Frise, E.; Kaynig, V.; Longair, M.; Pietzsch, T.; Preibisch, S.; Rueden, C.; Saalfeld, S.; Schmid, B.; et al. Fiji: an open-source platform for biological-image analysis. *Nature Methods* **2012**, *9* (7), 676-682. DOI: 10.1038/nmeth.2019.

(88) Yamane, T.; Hanaoka, K.; Muramatsu, Y.; Tamura, K.; Adachi, Y.; Miyashita, Y.; Hirata, Y.; Nagano, T. Method for Enhancing Cell Penetration of Gd3+-based MRI Contrast Agents by Conjugation with Hydrophobic Fluorescent Dyes. *Bioconjugate Chemistry* **2011**, *22* (11), 2227-2236. DOI: 10.1021/bc200127t.

(89) Sulpizi, M.; Gaigeot, M.-P.; Sprik, M. The Silica–Water Interface: How the Silanols Determine the Surface Acidity and Modulate the Water Properties. *Journal of Chemical Theory and Computation* **2012**, *8* (3), 1037-1047. DOI: 10.1021/ct2007154.

(90) Del Favero, G.; Bialas, F.; Grabher, S.; Wittig, A.; Bräuer, B.; Gerthsen, D.; Echalier, C.; Kamalov, M.; Marko, D.; Becker, C. F. W. Silica particles with a quercetin-R5 peptide conjugate are taken up into HT-29 cells and translocate into the nucleus. *Chem Commun (Camb)* **2019**, *55* (65), 9649-9652. DOI: 10.1039/c9cc02215e From NLM.

(91) Djiadeu, P.; Azzouz, D.; Khan, M. A.; Kotra, L. P.; Sweezey, N.; Palaniyar, N. Ultraviolet irradiation increases green fluorescence of dihydrorhodamine (DHR) 123: false-positive results for reactive oxygen species generation. *Pharmacol Res Perspect* **2017**, *5* (2), e00303. DOI: 10.1002/prp2.303 From NLM.

(92) Karlsson, A.; Nixon, J. B.; McPhail, L. C. Phorbol myristate acetate induces neutrophil NADPH-oxidase activity by two separate signal transduction pathways: dependent or independent of phosphatidylinositol 3-kinase. *J Leukoc Biol* **2000**, *67* (3), 396-404. DOI: 10.1002/jlb.67.3.396 From NLM.

(93) Yazdi, A. S.; Guarda, G.; Riteau, N.; Drexler, S. K.; Tardivel, A.; Couillin, I.; Tschopp, J. Nanoparticles activate the NLR pyrin domain containing 3 (Nlrp3) inflammasome and cause pulmonary inflammation through release of IL-1α and IL-1β. *Proceedings of the National*

Academy of Sciences **2010**, *107* (45), 19449-19454. DOI: 10.1073/pnas.1008155107 (acccessed 2023/11/21).

(94) Fubini, B.; Hubbard, A. Reactive oxygen species (ROS) and reactive nitrogen species (RNS) generation by silica in inflammation and fibrosis. *Free Radic Biol Med* **2003**, *34* (12), 1507-1516. DOI: 10.1016/s0891-5849(03)00149-7 From NLM.

(95) Park, Y.-H.; Bae, H. C.; Jang, Y.; Jeong, S. H.; Lee, H. N.; Ryu, W.-I.; Yoo, M. G.; Kim, Y.-R.; Kim, M.-K.; Lee, J. K.; et al. Effect of the size and surface charge of silica nanoparticles on cutaneous toxicity. *Molecular & Cellular Toxicology* **2013**, *9* (1), 67-74. DOI: 10.1007/s13273-013-0010-7.

(96) Maurer-Jones, M. A.; Lin, Y.-S.; Haynes, C. L. Functional Assessment of Metal Oxide Nanoparticle Toxicity in Immune Cells. *ACS Nano* **2010**, *4* (6), 3363-3373. DOI: 10.1021/nn9018834.

(97) Zhang, H.; Dunphy, D. R.; Jiang, X.; Meng, H.; Sun, B.; Tarn, D.; Xue, M.; Wang, X.; Lin, S.; Ji, Z.; et al. Processing pathway dependence of amorphous silica nanoparticle toxicity: colloidal vs pyrolytic. *J Am Chem Soc* **2012**, *134* (38), 15790-15804. DOI: 10.1021/ja304907c From NLM.

(98) Sharp, F. A.; Ruane, D.; Claass, B.; Creagh, E.; Harris, J.; Malyala, P.; Singh, M.; O'Hagan, D. T.; Pétrilli, V.; Tschopp, J.; et al. Uptake of particulate vaccine adjuvants by dendritic cells activates the NALP3 inflammasome. *Proc Natl Acad Sci U S A* **2009**, *106* (3), 870-875. DOI: 10.1073/pnas.0804897106 From NLM.

(99) Gregory, A. E.; Titball, R.; Williamson, D. Vaccine delivery using nanoparticles. *Front Cell Infect Microbiol* **2013**, *3*, 13. DOI: 10.3389/fcimb.2013.00013 From NLM.

List of abbreviations

ACN	……	Acetonitrile
AU	……	Absorption unit
Boc	……	t-Butyloxycarbonyl
Cy5	……	Cyanine 5
Dab	……	2,4-diaminobutyric acid
DAG	……	Diacylglycerol
DCM	……	Dichloromethane
DHR	……	Dihydro rhodamine
DIC	……	Diispropyl carbodiimide
DMF	……	N,N-Dimethylformamide
DMS	……	Dimethyl sulfide
ESI	……	Electron-spray ionization
FACS	……	Fluorescence activated cell sorting
Fmoc	……	9-fluorenylmethoxycarbonyl

FPR	.....	Formyl peptide receptor
GuaHCl	.....	Guanidinium hydrochloride
HATU	.....	2-(1H-7-Azabenzotriazol-1-yl)-1,1,3,3-tetramethyluronoium hexafluorphosphate
HF	.....	Hydrogen Fluoride
HHBS	.....	Hank's buffer with HEPES
HPLC	.....	High performance liquid chromatography
IL-1β	.....	Interleukin 1β
IP_3	.....	Inositol trisphosphate
LCP	.....	Long chain polyamines
MS	.....	Mass spectrometry
Mtt	.....	4-Methyltrityl
NLRP3	.....	NOD-, LRR- and pyrin domain-containing protein 3
NMR	.....	Nuclear magnetic resonance
NPF	.....	4-Nitrophenyl formate
Oxyma	.....	Ethyl 2-cyano-2-(hydroxyimino) acetate
PAMPs	.....	Pathogen associated molecular patterns
PBS	.....	Phosphate buffer saline
PEG	.....	Polyethylene glycol
PI3K	.....	Phosphoinositide 3-kinase
PIP	.....	Phosphoinositol 4,5 bisphosphate
PKC	.....	Protein kinase C
PL	.....	Phospholipase
PMA	.....	Phorbol myristate acetate
PRR	.....	Pattern recognition receptor
ROS	.....	Reactive oxygen species
RP	.....	Reversed-phase
RPMI	.....	Roswell Park Memorial Institute
RT	.....	Room temperature
SAS	.....	Solvent accessible surface
SDV	.....	Silica deposition vesicle
SEM	.....	Scanning electron microscopy
SPPS	.....	Solid-phase peptide synthesis
Sv	.....	Substitution value
TFA	.....	Trifluoroacetic acid
TIS	.....	Triisopropyl silane

TLR	……	Toll-like receptor
TMOS	……	Tetramethyl orthosilicate
TNF-α	……	Tumor necrose factor α
TOCSY	……	Total correlation spectroscopy

List of figures

List of tables